MECHANICAL PROPERTIES OF CELLULOSE NANOCRYSTAL THIN FILMS

USING A STRUCTURING APPROACH TO ASSESS THE MECHANICAL PROPERTIES OF CELLULOSE NANOCRYSTAL-BASED THIN FILMS

By UROOJ GILL, B.Sc.

A Thesis

Submitted to the School of Graduate Studies

in Partial Fulfillment of the Requirements for the

Degree Master of Science

Master of Science (2017)

McMaster University (Chemical Biology), Hamilton, Ontario

Title: Using a Structuring Approach to Assess the Mechanical Properties of Cellulose Nanocrystal-Based Thin Films

Author: Urooj Gill, B.Sc. (McMaster University)

Supervisors: Professor Jose M. Moran-Mirabal, Professor Emily D. Cranston

Number of Pages: xvi, 125

.

Lay Abstract

The mechanical properties of coatings made of cellulose-derived nanoparticles changes with relative humidity, due to the water-absorbing nature of the nanoparticles. Thus, the focus of this work was to study the stiffness of these coatings in a humidity-independent manner, and to link changes in mechanical properties to changes in the coating fabrication method. Coatings with two compositions were studied, consisting of cellulose nanoparticles combined with different polymers, or cellulose nanoparticles only. These coatings were prepared on pre-stressed substrates that shrunk when heated. The coatings wrinkled with the shrinking substrate, where the wrinkles were analyzed to calculate the stiffness of the coatings. The mechanical properties of coatings with nanoparticles and polymers were found to be humidity-independent and changed with coating composition. For the all-cellulose nanoparticle coatings, changes in the wrinkle's appearance (which implies changes in stiffness) could be linked to changes in the nanoparticle orientation. Knowledge of these coatings' mechanical properties is crucial to finding applications that are most suitable for these nanoparticles extracted from nature.

Abstract

The goal of this work was to quantify the mechanical properties of cellulose nanocrystal (CNC)-based thin films using a polystyrene (PS) structuring approach. This structuring approach was used to biaxially wrinkle CNC-polymer and all-CNC films, in order to assess how changes in the film fabrication process affected the elastic modulus of these films. All films were prepared on pre-stressed PS substrates and structured by heating them above the glass transition temperature of PS, which caused the substrates to shrink and the films to wrinkle biaxially. CNC-polymer films were prepared using the layer-by-layer approach, where three parameters were modified to obtain films of varying compositions: 1) type of polymer (xyloglucan, XG, or polyethyleneimine, PEI), 2) polymer concentration (0.1 wt% or 1 wt%), and 3) film thickness (*i.e.*, number of deposited bilayers). After these films were structured, their elastic moduli were calculated to be 70 ± 2 GPa for CNC-$XG_{0.1}$, 72 ± 2 GPa for CNC-$PEI_{0.1}$, and 32.2 ± 0.8 GPa for CNC-$PEI_{1.0}$ films, indicating that the mechanical properties of CNC-polymer films changed with film composition. This structuring method was also found to provide a humidity-independent measurement of the modulus due to the irreversible nature of the wrinkling. Next, to prepare all-CNC films, CNC suspensions were evaporated under conditions designed to control the film thickness (using 0.005 wt% – 8 wt% CNC suspensions) and CNC nanoparticle orientation (chiral nematic, isotropic, or uniaxial). Suspensions were dried slowly under vacuum, quickly by heating, or by spin-coating to form films with chiral nematic, isotropic, or uniaxial (radial) CNC orientations, respectively. Following structuring, these wrinkled films showed unique morphologies that changed with

nanoparticle orientation, suggesting that their mechanical properties are dependent on the CNC orientation within the films. The work presented in this thesis implies that the mechanical properties of films fabricated from hygroscopic bio-based nanomaterials can be assessed in a humidity-independent way by using the structuring method presented. Quantifying the mechanical properties of these films is critical to assess the potential applications of CNCs, where CNC-based materials may be used in developing paper-based electronics, extracellular matrix mimics, and plant cell wall mimics.

Acknowledgements

I would like to start by thanking my supervisors Dr. Jose M. Moran-Mirabal and Dr. Emily D. Cranston for taking me on as a Master's student – this work would not have been possible without your constant patience, guidance, and support. Jose, thank you for giving me the opportunity to work in your lab before I began my Master's, as both a summer volunteer and a fourth year thesis student. This was my first experience working in a research lab, and it was where I learned that I truly enjoyed doing research. It was this experience that helped me decide that I wanted to continue doing research in the form of my Master's!

I am very grateful to the past and current members of the Moran-Mirabal and Cranston groups for providing very supportive and friendly work environments for me to work in, over the past two years. In particular, I would like to thank Dr. Yujie Zhu for always being willing to help me in the lab, and my undergraduate student Travis Sutherland for all of his hard work and dedication to our project. To the graduate students in the Moran-Mirabal group – Ayodele Fatona, Markus Rose, Kevin Saem, Mouhanad Babi, Xiuping Ding, Christal Zhou, Helen Luu, Petr Nalivaika, and Sara Makaremi – thank you for always being so supportive, encouraging, and willing to help, and for providing a wonderful and fun environment to work in. To the graduate students in the Cranston group – Heera Marway, Dan Osorio, Justin Hu, Oriana Vanderfleet, Dan LeClair, Steph Kedzior, Elli Niinivaara, Mike Reid, Kevin De France, Steven Toniolo, Blair Morgan, and Lily Liu – thank you for making the group meetings very enjoyable and insightful; it was a great

opportunity for me to learn about cellulose and vaccines, and anything else in between that came up during the meetings.

A special thanks to Dr. Maikel C. Rheinstädter, Dr. Dawn M.E. Bowdish, Dr. Todd Hoare, Dr. Robert Pelton, Dr. Stephen Veldhuis, and Dr. Peter Mascher for access to equipment and chemical/biological reagents.

And lastly, I would like to say thank you to my friends and family for their constant and unwavering support over the past two years. You have all been amazing, and I could not have asked for a better support group. To my family – my mum, dad, brother, and sister-in-law – thank you for learning a little bit about my research (mainly because I never stop talking about it) and for reading my paper, even though the material may have been difficult to understand. Perhaps most importantly of all, I am grateful for all the delicious food you provided me with which, at times, was my main source of motivation!

Table of Contents

Lay Abstract iii

Abstract iv

Acknowledgements vi

Table of Contents viii

List of Figures xi

List of Abbreviations and Symbols xv

Declaration of Academic Achievement xvi

Chapter 1 – Introduction 1

1.1. Understanding the Mechanical Properties of Cellulose Nanocrystal Thin Films 1

1.2. Research Objectives 3

1.3. Thesis Outline 4

1.4. References 4

Chapter 2 – Literature Review 6

2.1. Cellulose and Nanocellulose 6

2.1.1. Cellulose Nanofibrils (CNFs) 9

2.1.2. Cellulose Nanocrystals (CNCs) 10

2.2. Preparation of CNC-Based Thin Films 14

2.2.1. CNC Biocomposite Films 15

2.2.2. All-CNC Films 16

2.3. CNC Mechanical Properties and their Limitations 20

2.3.1. Mechanical Properties of CNCs 20

2.3.2. Mechanical Properties of CNC-Based Thin Films 21

2.4. Structuring Methods to Assess Thin Film Mechanical Properties 22

2.4.1. External Compression of a Polymeric Substrate 22

2.4.2. Structuring Through Shape-Memory Polymer Thermal Shrinkage 25

2.5. References 27

Chapter 3 – Beyond Buckling: Humidity-Independent Measurement of the Mechanical Properties of Green Nanobiocomposite Films 32

3.1. Abstract 33
3.2. Introduction 34
3.3. Experimental 38
3.3.1. Chemicals 38
3.3.2. Biologicals 38
3.3.3. Preparation of Cellulose Nanocrystals (CNCs) 39
3.3.4. Polystyrene (PS) Substrate Preparation 40
3.3.5. Nanobiocomposite Film Preparation 40
3.3.6. Structuring of Nanobiocomposite Films 41
3.3.7. Atomic Force Microscopy (AFM) 41
3.3.8. Variable Angle Spectroscopic Ellipsometry (VASE) 41
3.3.9. X-Ray Diffraction (XRD) 42
3.3.10. White Light Interference Microscopy (WLIM) 43
3.3.11. Scanning Electron Microscopy (SEM) 44
3.3.12. Structure Analysis of Structured Nanobiocomposite Films 44
3.3.13. Elastic Modulus Calculations 45
3.3.14. RAW264.7 Cell Culturing 46
3.3.15. Cell Viability 46
3.3.16. Cell Fixation, Staining, and Imaging Using Fluorescence Microscopy 47
3.3.17. Fractal Analysis 48
3.4. Results and Discussion 48
3.4.1. Structuring of CNC-Polymer Nanobiocomposite Films 48
3.4.2. Characterization of CNC-Polymer Nanobiocomposite Films 51
3.4.3. Mechanical Properties and Composition of CNC-Polymer Nanobiocomposite Films 55
3.4.4. Cell Viability and Morphology on CNC-Polymer Nanobiocomposite Films 60
3.5. Conclusions 63
3.6. Acknowledgements 65
3.7. References 65

Chapter 4 – Mechanical Properties of All-Cellulose Nanocrystal Thin Films as a Function of Nanoparticle Orientation 71
4.1. Abstract 72
4.2. Introduction 73
4.3. Experimental 77
4.3.1. Production of Cellulose Nanocrystals (CNCs) 77
4.3.2. Preparation of Polystyrene (PS) Substrates 78
4.3.3. Fabrication of All-CNC Thin Films 79
4.3.4. Structuring of All-CNC Films 80
4.3.5. Polarized Optical Microscopy (POM) 80
4.3.6. Variable Angle Spectroscopic Ellipsometry (VASE) 80
4.3.7. Scanning Electron Microscopy (SEM) 81
4.4. Results and Discussion 81
4.4.1. Fabrication of All-CNC Films 81
4.4.2. Structuring of All-CNC Films 93
4.5. Conclusions 100
4.6. Acknowledgements 101
4.7. References 102
Chapter 5 – Conclusions and Future Outlooks 105
5.1. Conclusions 105
5.2. Future Outlooks 107
Appendix A – Supplementary Information for Chapter 3 110
Appendix B – Supplementary Information for Chapter 4 122

List of Figures

Chapter 2

Figure 2-1 Chemical structure of a glucan chain, where each cellobiose consists of a dimer of anhydroglucose molecules that are rotated 180° relative to one another 8

Figure 2-2 Transmission electron microscopy (TEM) images of (A) TEMPO-oxidized CNFs and (B) wood-derived CNCs 10

Figure 2-3 Schematic outlining the acid hydrolysis of cellulose to produce CNCs 12

Figure 2-4 During acid hydrolysis, the more accessible disordered regions of cellulose are cleaved first, leaving behind CNCs – the crystalline cellulose particles 13

Figure 2-5 Schematic outlining the various surface functionalities that can be introduced onto CNCs, based on the hydrolysis conditions used to extract these nanoparticles from cellulose 14

Figure 2-6 Chiral nematic ordering of CNCs in suspension. (A) Above a critical concentration, CNC suspensions will separate into an upper isotropic phase (left) and a lower anisotropic, or cholesteric, phase (right). (B) When the anisotropic phase of a CNC suspension is imaged by polarized optical microscopy (POM), a characteristic fingerprint texture is seen 18

Figure 2-7 Atomic force microscopy (AFM) height images of CNC-based films prepared by dip-coating of a substrate. (A) Films prepared from the isotropic phase of CNC suspensions have isotropically oriented CNCs, while (B) films prepared from the anisotropic phase of suspensions have linearly oriented CNCs. A 2D fast Fourier transform of these films confirms that the CNCs are oriented isotropically and linearly, respectively 19

Figure 2-8 (A) Optical microscopy and (B) AFM images of a uniaxially wrinkled film (top) and an isotropically wrinkled film (bottom) on a soft underlying substrate 24

Figure 2-9 (A) Schematic showing a thin gold film deposited on a pre-stressed polystyrene (PS) substrate, which structures when the substrate is shrunken above its glass transition temperature. Scanning electron microscopy (SEM) images are shown of (A) uniaxial (thickness = 10 nm)

and (B) biaxial (thickness = 200 nm) wrinkled gold films, following the PS shrinking step 26

Chapter 3

Figure 3-1 Fabrication of LbL nanobiocomposite structured films. A) LbL films were fabricated on pre-stressed PS substrates. PAH was first deposited onto the substrates, followed by the deposition of CNC-polymer bilayers. In the LbL fabrication process, alternating layers of CNCs and polymer (XG or PEI) were successively adsorbed from solution onto the substrates, forming one bilayer (N = 1). This bilayer deposition process was repeated to form films of varied thicknesses. The CNC-polymer films were then structured by heating the PS substrates, which caused them to shrink biaxially and wrinkle the CNC-polymer films. B) Atomic force microscopy (AFM) height image of a structured CNC-polymer film composed of 20 bilayers (image zoomed into a flat area that allowed AFM tracing). C) Chemical structures of xyloglucan and polyethyleneimine 49

Figure 3-2 SEM images of biaxially wrinkled CNC-polymer films with varying number of deposited bilayers 50

Figure 3-3 Thickness measurements were obtained for all CNC-polymer films using variable angle spectroscopic ellipsometry, where the slopes indicate average thicknesses per bilayer in nanometers, n = 3, all $R^2 \geq 0.96$. White light interferometry was used to characterize the roughness of the nanobiocomposite films prior to structuring (lines and number indicate average roughness) and following structuring, n ≥ 15. For all plots zero (●), full (♦) and half bilayers (▲) are indicated 53

Figure 3-4 Calculation of the elastic modulus from the morphological analysis of the structured nanobiocomposite films. A) Intensity versus characteristic length plots were generated via 2D FFT analysis for the corresponding wrinkled structures. These plots were averaged, where the wrinkle length values at the highest intensities were determined (peaks in boxed area), and averaged to calculate the characteristic length. Plots of characteristic wrinkle length (ζ) vs. film thickness were generated for (B) CNC-$XG_{0.1}$, (C) CNC-$PEI_{0.1}$, and (D) CNC-$PEI_{1.0}$ films, where the slopes were used with Equation 1 to calculate the elastic moduli. Full (♦) and half (▲) bilayers are indicated, n ≥ 3, all $R^2 > 0.94$-0.97. Open circles indicate films that were hydrated by immersion in water for 30 minutes prior to structuring 56

Figure 3-5 X-ray diffraction measurements were used to determine the relative film compositions. A) Schematic for the XRD set-up. B) 2D X-ray plots in the xy plane ($q_{||}$) and xz plane (q_z) for pure polymer samples $PEI_{1.0}$ and CNCs, and a composite CNC-$PEI_{1.0}$ film (N = 20 bilayers). C) Intensity data extracted from the 2D X-ray plot for the CNC-$PEI_{1.0}$ film was analyzed in two sections (black and pink outlines), and fitted using the X-ray profile obtained from the pure polymer samples 58

Figure 3-6 Fluorescence images of RAW264.7 cells seeded onto unstructured and structured CNC-$PEI_{1.0}$ surfaces that were prepared at various bilayers (BLs). A) The LIVE/DEAD cytotoxicity assay indicates living cells stained by calcein (green) and dead cells stained by ethidium homodimer-1 (red); scale bar = 50 µm. B) Epifluorescence images of individual cells were obtained by staining the cells with 4',6-diamino-2-phenylindole (DAPI) (blue) and AlexaFluor 488-phalloidin (green) for their nuclei and actin filaments, respectively; scale bars = 10 µm 63

Chapter 4

Figure 4-1 Fabrication method used to prepare all-cellulose nanocrystal (CNC) thin films. Polystyrene (PS) substrates were masked with a vinyl sheet, exposing only a circular region in the center of the substrates (r = 0.846 cm). The substrates were then oxidized with plasma, after which the vinyl sheets were removed from the PS. CNC suspensions of varying concentrations were drop-cast onto the PS substrates and allowed to evaporate. The method of evaporation used – drying under vacuum, heating, or spin-coating – dictated CNC orientation within the films – chiral nematic, isotropic, or uniaxial (radial). Once these films were prepared, they were then structured using a shrinking approach. PS substrates were heated above their glass transition temperature, which caused the substrates to shrink and the all-CNC films to subsequently structure 82

Figure 4-2 Macroscopic view of all-CNC films prepared from concentrated CNC suspensions, that were either dried slowly under vacuum (left) or quickly by heating (right) 84

Figure 4-3 Polarized optical microscopy (POM) images of all-CNC films prepared by drying CNC suspensions under vacuum. Films showed distinct textures when prepared at thicknesses beyond 0.8 µm (CNC wt% $\geq$ 0.1), but showed little-to-no texturing at thicknesses lower than 0.5 µm (CNC wt% $\leq$ 0.04). The estimated film thickness (h) at each wt% suspension is shown as an inset in the POM images. Images were taken in the centre of

the film between crossed polarizers, using a 530 nm retardation waveplate 86

Figure 4-4 POM images taken at 100x of all-CNC films prepared under vacuum. Fingerprint texture is present in these films, and is a result of chiral nematic CNC orientations. Images were taken in the centre of the film between crossed polarizers, using a 530 nm retardation waveplate 87

Figure 4-5 POM images of all-CNC films prepared by drying CNC suspensions through heating. Films showed distinct textures when prepared at thicknesses beyond 2 μm (CNC wt% ≥ 0.25), but exhibited little-to-no texturing at thicknesses below 1 μm (CNC wt% ≤ 0.1). The estimated film thickness (h) at each wt% suspension is shown as an inset in the POM images. Images were taken in the centre of the film between crossed polarizers, using a 530 nm retardation waveplate 91

Figure 4-6 POM images of all-CNC films prepared by spin-coating of CNC suspensions. A 1 wt% CNC suspension was spin-coated multiple times (N) on PS substrates to produce films of thicknesses ranging from 0.2 – 0.49 μm. Film thickness (h) was determined by variable angle spectroscopic ellipsometry (VASE), and is shown as an inset within the POM images. Images were taken in the centre of the film between crossed polarizers, using a 530 nm retardation waveplate 92

Figure 4-7 SEM images of structured all-CNC films that were prepared under vacuum. Films of thicknesses beyond 26 μm (CNC wt% ≥ 3) delaminated from the underlying substrate during structuring, leaving behind a thin CNC film that structured with the shrinking substrate. Structured films of thicknesses ranging from 0.9 – 8.9 μm (CNC wt% between 0.1 and 1) did not delaminate from the substrate, but were cracked across the entire film surface. When films were structured with thicknesses below 0.5 μm (CNC wt% ≤ 0.05), they biaxially wrinkled with the shrinking substrate and did not delaminate or crack 95

Figure 4-8 POM and SEM images for structured thin all-CNC films dried A) under vacuum, B) by heating, or C) through spin-coating (with N number of subsequent depositions, or varying film thicknesses) 99

Figure 4-9 SEM comparison of structured all-CNC films prepared at near identical thicknesses. Thickness (h) values are shown as an inset of the SEM images, and were measured by VASE. An SEM image of a CNC-polymer film is also shown 100

List of Abbreviations and Symbols

AFM	Atomic force microscopy
CNC	Cellulose nanocrystal
CNF	Cellulose nanofibril
E_f	Elastic modulus of film
E_s	Elastic modulus of substrate
FFT	Fast Fourier transform
h	Film thickness
λ	Wrinkle wavelength
LbL	Layer-by-layer
PAH	Polyallylamine hydrochloride
PDMS	Poly(dimethylsiloxane)
PEI	Polyethyleneimine
POM	Polarized optical microscopy
PS	Polystyrene
SEM	Scanning electron microscopy
SIEBIMM	Strain-induced elastic buckling instability for mechanical measurements
TEMPO	2,2,6,6-Tetramethylpiperidine-1-oxyl
VASE	Variable angle spectroscopic ellipsometry
ν_f	Poisson's ratio of film
ν_s	Poisson's ratio of substrate
WLIM	White light interference microscopy
ξ	Persistence length
XG	Xyloglucan
XRD	X-ray diffraction
ζ	Characteristic wrinkle length

Declaration of Academic Achievement

I declare that the research contribution which follows is original work, completed and written by me, with editorial assistance from my supervisors Dr. Jose M. Moran-Mirabal and Dr. Emily D. Cranston.

The following individuals contributed to experimentation and data analysis:

- In Chapter 3, Travis Sutherland aided in sample and image preparation, Elina Niinivaara obtained atomic force microscopy (AFM) images, Dr. Yujie Zhu & Sokunthearath (Kevin) Saem helped obtain scanning electron microscopy (SEM) images, Sebastian Himbert performed X-ray diffraction measurements and aided in subsequent data analysis, and Justin P. Boyle performed cell work.
- In Chapter 4, Sokunthearath (Kevin) Saem & Dr. Yujie Zhu obtained SEM images.

Chapter 1 – Introduction

1.1. Understanding the Mechanical Properties of Cellulose Nanocrystal Thin Films

Bio-based nanomaterials (*e.g.*, cellulose- and starch-derived nanoparticles) are of interest as potential candidates for replacing current fossil fuel-derived materials (*e.g.*, oil, coal, natural gas). The need to substitute these materials arises from the increasing anthropogenic carbon footprint left from consumer products that make use of these fossil fuel materials. Greenhouse gases, mainly carbon dioxide, are generated through the production and consumption of fossil fuel energy. The amount of carbon dioxide generated from fossil fuels has doubled between 1970 to 2008 (where 30 billion tons of carbon dioxide were produced in 2008), and this is rapidly affecting global warming and climate change.[1] Not only are fossil fuel-derived materials impacting the world, they are also being depleted rapidly; their rate of production takes millions of years, and is not able to keep up with their rate of depletion. For these reasons, it is crucial to find materials to substitute fossil fuel-derived materials which are both environmentally-friendly and renewable.

Bio-based nanomaterials are a promising alternative since they can be produced from renewable resources, are biodegradable, and are generally non-toxic. Examples of such materials are cellulose-derived nanoparticles known as cellulose nanocrystals (CNCs), which are rod-shaped crystalline polymer particles with high mechanical and tensile strengths.[2] Due to the "green" and sustainable nature of CNCs, research on these nanomaterials continues to expand into numerous areas, such as those that require renewable and eco-friendly components. CNCs can add strength, function and value to

many hybrid materials such as emulsions, hydrogels, foams, paints, adhesives and thin films.[2,3] In regards to thin films and coatings, CNCs can be used to prepare nanocomposites or all-nanoparticle films, which consist of a network of nanoparticles that strongly interact with other materials (*e.g.*, polymers, other types of nanoparticles) or nanoparticles that interact with one another through intermolecular and surface forces. In this way, films with varying compositions and properties (*e.g.*, mechanical, physical, chemical, electrical properties) can be prepared. However, to find the most suitable applications for CNC nanocomposites and thin films, their mechanical properties need to be determined. Knowing the mechanical properties of these bio-based nanomaterials could open new avenues of research and product development for CNCs.

Various techniques have been used to quantify the mechanical properties of thin films, such as three-point bending flexural tests, nanoindentation, thin film buckling, and dynamic mechanical analysis (DMA).[4,5] These methods are advantageous to use because sample preparation requirements are very simple and sample testing is relatively straightforward. However, there are also disadvantages to using these methods. While sample requirements are simple, these methods can only quantify free-standing films, films that are not soft or "sticky", and films of larger thicknesses (micron-range and higher). These methods also have low precision, low sensitivity, and modeling assumptions that skew the quantification of the mechanical properties. When working with thin films consisting of bio-based nanomaterials such as CNCs, an additional problem is the hygroscopic nature of the nanomaterials, where the mechanical properties of these films change with relative humidity.[6] The mechanical properties of CNC nanocomposites and

thin films have been studied using DMA, tensile testing, modeling methods, and buckling.[6–8] The biggest drawback to using these methods, other than those listed above, is that the mechanical properties change with relative humidity, since these films bind strongly to water.[6] Therefore, the work presented in this thesis focuses on investigating the mechanical properties of CNC-based thin films in a way that is independent of humidity, while also looking at how the mechanical properties of these films changes with adjustments to the film fabrication process.

1.2. Research Objectives

The goal of this thesis is to investigate the mechanical properties of CNC-based thin films using a polystyrene (PS) structuring approach, in order to calculate the elastic modulus of these films in a humidity-independent manner. Furthermore, the work aims to link changes in the film's elastic modulus to the film fabrication procedure. In particular, two types of CNC-based films are studied: CNC-polymer nanocomposite films and all-CNC films.

CNC-Polymer Nanocomposite Films:

This work focuses on the fabrication and structuring of CNC-polymer films, to produce structured films with different CNC-to-polymer ratios and mechanical strengths. This structuring approach shows that the mechanical properties of these films can be determined in a humidity-independent fashion, and also indicates that the mechanical properties of these films can be linked to changes in the film composition.

All-CNC Films:

This work focuses on the preparation of all-CNC films with different types of CNC orientation, followed by the subsequent structuring of these films to produce wrinkled materials. This structuring approach relates changes in nanoparticle orientation to changes in both the wrinkle morphology and the mechanical properties of the films.

1.3. Thesis Outline

This thesis consists of five chapters, which includes this Introduction (Chapter 1). Chapter 2 presents a detailed literature review of cellulose and nanocellulose, their incorporation into films, the mechanical strength of these materials, and structuring methods used to study the mechanical properties of these films. Chapter 3 describes work where CNC-polymer films of varying compositions are fabricated and structured, in order to determine their mechanical properties. This work has been published in *Nanoscale*.[9] Chapter 4 presents work where all-CNC films are prepared with varying CNC orientation, and are structured to produce morphologies that change as a function of CNC orientation. The goal of this chapter is to begin relating the film's mechanical properties to changes in nanoparticle orientation. This work will be submitted for publication and is currently a manuscript in preparation. Lastly, Chapter 5 summarizes the main conclusions of this thesis, and provides recommendations to expand on this work.

1.4. References

(1) Höök, M.; Tang, X. Depletion of Fossil Fuels and Anthropogenic Climate change—A Review. *Energy Policy* **2013**, *52*, 797–809.

(2) Habibi, Y.; Lucia, L. A.; Rojas, O. J. Cellulose Nanocrystals: Chemistry, Self-Assembly, and Applications. *Chem. Rev.* **2010**, *110* (6), 3479–3500.

(3) Martin, C.; Jean, B. Nanocellulose/polymer Multilayered Thin Films: Tunable Architectures towards Tailored Physical Properties. *Nord. Pulp Pap. Res. J.* **2014**, *29* (1), 19–30.

(4) *Front Matter, in Polymer Composites: Volume 2*; Thomas, S., Joseph, K., Malhotra, S. K., Goda, K., Sreekala, M. S., Eds.; Wiley-VCH Verlag GmbH & Co. KGaA: Weinheim, Germany, 2013.

(5) Stafford, C. M.; Harrison, C.; Beers, K. L.; Karim, A.; Amis, E. J.; VanLandingham, M. R.; Kim, H.-C.; Volksen, W.; Miller, R. D.; Simonyi, E. E. A Buckling-Based Metrology for Measuring the Elastic Moduli of Polymeric Thin Films. *Nat. Mater.* **2004**, *3* (8), 545–550.

(6) Kan, K. H. M.; Cranston, E. D. Mechanical Testing of Thin Film Nanocellulose Composites Using Buckling Mechanics. *TAPPI J.* **2013**, *12* (4), 9–17.

(7) Moon, R. J.; Martini, A.; Nairn, J.; Simonsen, J.; Youngblood, J. Cellulose Nanomaterials Review: Structure, Properties and Nanocomposites. *Chem. Soc. Rev.* **2011**, *40*, 3941–3994.

(8) Gindl, W.; Keckes, J. Drawing of Self-Reinforced Cellulose Films. *J. Appl. Polym. Sci.* **2007**, *103*, 2703–2708.

(9) Gill, U.; Sutherland, T.; Himbert, S.; Zhu, Y.; Rheinstädter, M. C.; Cranston, E. D.; Moran-Mirabal, J. M. Beyond Buckling: Humidity-Independent Measurement of the Mechanical Properties of Green Nanobiocomposite Films. *Nanoscale* **2017**, *9* (23), 7781–7790.

Chapter 2 – Literature Review

2.1. Cellulose and Nanocellulose

Cellulose is the most abundant biopolymer in nature, easily found and extracted from various sources including plants, bacteria, tunicates, algae, and fungi.[1–5] This bio-based material has been of interest for millennia, where cellulose in both its raw and derivatized forms continues to find practical and potential applications in the development of paper, filler agents (pharmaceuticals), textiles, food thickeners, biofuels, building insulation additives, coatings, optical films, and cosmetics.[5] With the increasing demand for materials that are renewable and non-cytotoxic, cellulose is emerging as a promising material that can replace non-sustainable materials such as those derived from fossil fuels.

Cellulosic materials possess a hierarchical structure with a fundamental cellulose unit known as the glucan chain (Figure 2-1), which is a linear polymer of anhydroglucose molecules linked by β-1,4-D-glycosidic bonds.[1,4,5] As a result of the glycosidic bond, each consecutive anhydroglucose molecule is rotated by 180° relative to the previous one in the glucan chain. This makes the crystallographic unit cell contain a cellobiose (dimer of anhydroglucose units), with a length along the glucan chain axis of ~1 nm. Cellulose I is the native cellulose product, which contains glucan chains that are pack in parallel configurations to one another (cellulose-derived materials used in this thesis are in the Cellulose I form). Each glucan chain also has an inherent asymmetry, and consists of a chemically nonreducing end (pendent hydroxyl group) and a reducing end (hemiacetal unit) (Figure 2-1). The degree of polymerization (DP) of cellulose, defined as the number of

anhydroglucose subunits within the cellulose chain, ranges from 150 – 20,000 and depends on the cellulose source used.

During the biosynthetic process, glucan chains are produced from glucose molecules but are not released as individual chains – instead, following synthesis, the chains aggregate and bundle into what is known as an elementary cellulose fibril, which has dimensions between 5-20 nm in diameter and many microns in length.[1,2,4,5] Generally, each elementary cellulose fibril consists of 36 glucan chains, but this number varies based on the biosynthetic route used by the organism. The glucan chain aggregation that occurs is favourable via inter- and intramolecular hydrogen bonding between and within chains, as well as through van der Waals interactions. The elementary cellulose fibrils then further assemble to form microfibrils, which are made up of regions of crystalline cellulose that are connected by dislocations, or defect regions, in the crystalline packing of cellulose.[1,2] Finally, microfibrils assemble to form macrofibrils, or the cellulose fibers themselves, which consist of crystalline and disordered regions of cellulose (tightly packed cellulose chains and more loosely packed cellulose chains, respectively). This hierarchical structure is ultimately what gives cellulose its unique mechanical, electrical, and optical properties.

Cellulose (and cellulose derivatives) have found a wide range of applications for two reasons: 1) the cellulose surface can be functionalized and 2) structurally stable cellulosic material from the macroscale (cellulose fibers) down to the nanoscale (nanocellulose) can be derived.[2,5] It can be difficult to introduce functionalities on the cellulose backbone because this typically requires activation of the hydroxyl groups to increase their reactivity, and also requires choosing a solvent that will not swell or dissolve

the crystalline cellulose.[5] Although this is the case, cellulose functionalization is pursued because once these limitations are overcome, functionalization of cellulose can be achieved with reproducible substitution patterns and degrees of reaction. Different functionalities can be introduced via the hydroxyl groups on the cellulose chains, such as carboxylic acids, urethanes linkages, esters, ethers, silyls, and sulfonates.[2,5] The polarity of cellulose can also be altered, and regioselective reactions can be carried out to select for the secondary hydroxyl groups as opposed to the primary hydroxyl groups, for example.[5] In this way, the functionalization of cellulose can result in cellulose-based materials with different types of surface chemistries and regioselective functionalities.

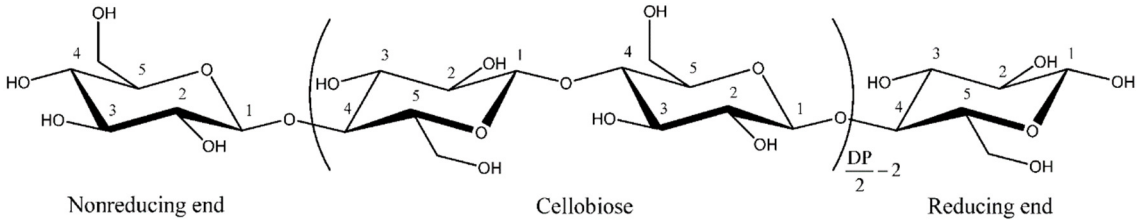

Figure 2-1. Chemical structure of a glucan chain, where each cellobiose consists of a dimer of anhydroglucose molecules that are rotated 180° relative to one another. Reproduced from reference 1.

The cellulose macrostructure can also be broken down to the nanoscale, to derive nanomaterials broadly known as nanocellulose.[2,5] Several methods are used to mechanically shear or chemically hydrolyze bulk cellulosic material and cellulose microfibrils to obtain nanocellulose, where the method used depends on the type of nanocellulose that is being derived. Interest in nanocellulose stems from its high

crystallinity and aspect ratios, as well as its mechanical, barrier, thermal, and optical properties, which can be exploited not only as standalone materials, but also within composites and mixtures. To this end, two types of nanocelluloses are commonly derived and studied – cellulose nanofibrils (CNFs) and cellulose nanocrystals (CNCs).

2.1.1. Cellulose Nanofibrils (CNFs)

Cellulose nanofibrils (CNFs) refer to nanoscale elementary cellulose fibrils which, in plant-derived fibrils, consist of approximately 36 glucan chains.[2] CNFs are composed of crystalline cellulose that is sporadically broken up by dislocations or disordered regions, and are derived from wood or plant fibers (macro- and microfibrils) through mechanical refinement.[2,3,6,7] It is challenging to produce CNFs directly from bulk cellulose since the fibrils remain aggregated or bound together via strong hydrogen bonding. Over the past few years, it has become more common to modify the cellulose prior to its mechanical disintegration (or refinement) using different chemical modifications or enzymatic treatments.[2,6,7] Chemicals used to modify bulk cellulose material include alkaline-acid combinations (*e.g.*, NaOH and HCl treatments) and ionic liquids (*e.g.*, 1-butyl-3-methylimidazolium chloride), while enzymes used include cellulases such as cellobiohydrolases and endoglucanases.[7] The goal of these treatments is to increase the surface area of the cellulose fibers for mechanical disintegration, and also to remove lignin and hemicelluloses present in the bulk cellulose material.

Once modified, the cellulose can then be mechanically refined to produce CNFs using microfluidizers, supergrinding, beating/homogenization, high-shear techniques,

cryogenic crushing, or ultrasonication.[2,3,6,7] The nanofibrils produced have lengths ranging from 500 nm to several microns, and widths in the 4-60 nm range (Figure 2-2a).[6,7] CNFs have high flexibility, strong rheological properties, and high porosity,[4,5,7] and are an attractive nanocellulosic material to work with for their potential applications in areas involving the development of nanopaper, food packaging, and coating technologies.[7]

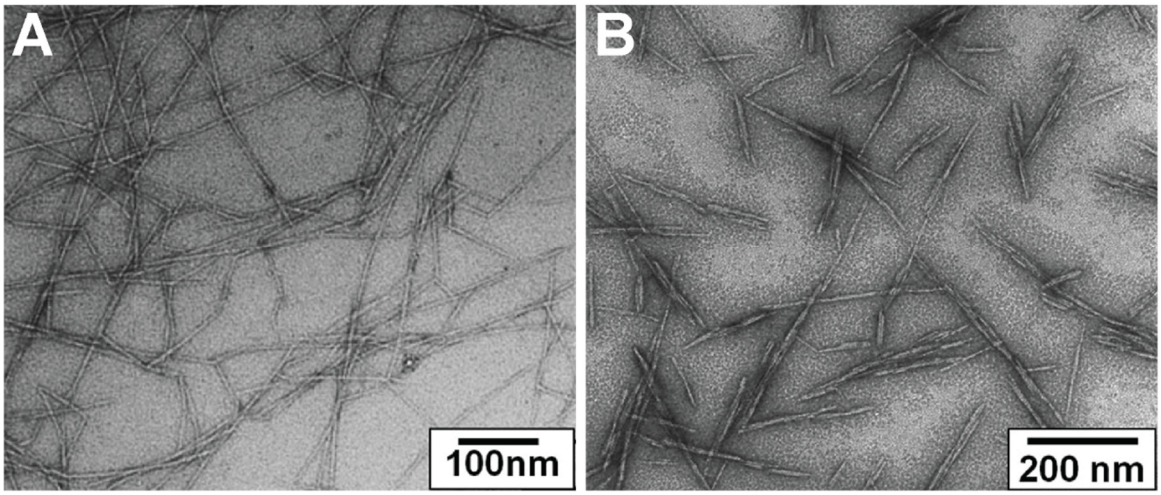

Figure 2-2. Transmission electron microscopy (TEM) images of (A) TEMPO-oxidized CNFs and (B) wood-derived CNCs. Reproduced from reference 2.

2.1.2. Cellulose Nanocrystals (CNCs)

Cellulose nanocrystals (CNCs) are crystalline rod-shaped nanoparticles extracted from natural cellulose sources.[1,2] They are produced by a controlled acid hydrolysis process (Figure 2-3), where the acid cleaves cellulose chains at the more readily accessible disordered regions of cellulose. Specifically, cleavage happens at the R_y-O-R_z glycosidic linkage, and is a multi-step process. The first step is protonation of the glycosidic oxygen

by the acid.[8] Following this, the hydroxyl of a water molecule enters and cleaves the polymer chain at the protonated oxygen, to yield two cellulose chains that have been cleaved at the glycosidic oxygen. When the disordered cellulose is hydrolyzed, it is converted to water-soluble oligosaccharides and glucose molecules, leaving behind the intact crystalline cellulose particles, or CNCs (Figure 2-4).[1,2,8]

Based on the acid used, the hydrolysis process may or may not introduce new chemical groups onto the CNC backbone.[1] Various acids have been reported for CNC production, including hydrochloric, sulfuric, phosphoric, hydrobromic, and nitric acids. The most commonly used acids in this process are sulfuric and hydrochloric acid. When the hydrolysis is performed with sulfuric acid, sulfate half-ester groups are introduced onto the CNCs at the surface primary and secondary hydroxyl sites, which renders the CNCs anionic (Figure 2-5). On the other hand, when hydrochloric acid is used, CNCs are produced from cellulose without any modifications to the cellulose backbone, and thus remain neutral.

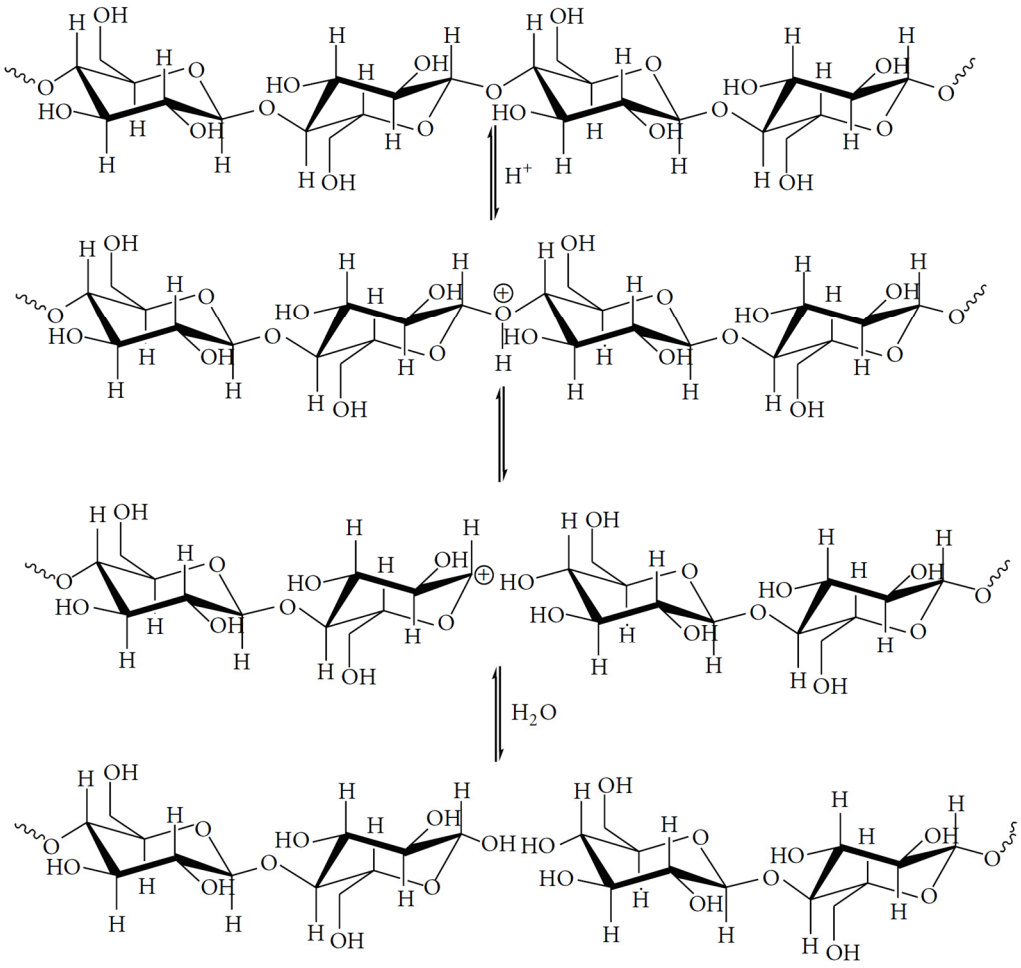

Figure 2-3. Schematic outlining the acid hydrolysis of cellulose to produce CNCs. Reproduced from reference 8.

Anionic CNCs form colloidally stable suspensions in aqueous media due to the electrostatic repulsion between neighbouring CNCs.[1,9] On the other hand, neutral CNCs tend to aggregate and do not form stable suspensions, since there is no electrostatic repulsion present between individual nanoparticles.[10] In order to improve the dispersibility of neutral CNCs, they can be further treated using TEMPO (2,2,6,6-tetramethylpiperidine-1-oxyl)-mediated oxidation, which oxidizes the surface C6 hydroxyl groups of glucose into

carboxyl groups, rendering the CNCs anionic.[11] Based on the starting cellulose source and the hydrolysis conditions used, the derived CNCs form stable aqueous suspensions that consist of rod-like particles with lengths of 70-1000 nm and widths of 3-50 nm (Figure 2-2b).[1,11] Typically, acid hydrolysis of wood and cotton sources produces CNCs with smaller dimensions (length 100-300 nm, width 3-10 nm), while CNCs extracted from tunicates and bacteria have much larger dimensions (tunicate: length 500-2000 nm, width 10-20 nm; bacteria: length 100-1000 nm, width 5-50 nm). By modifying the cellulose starting material used and the acid type, CNCs with various surface functionalities and physical characteristics can be produced.

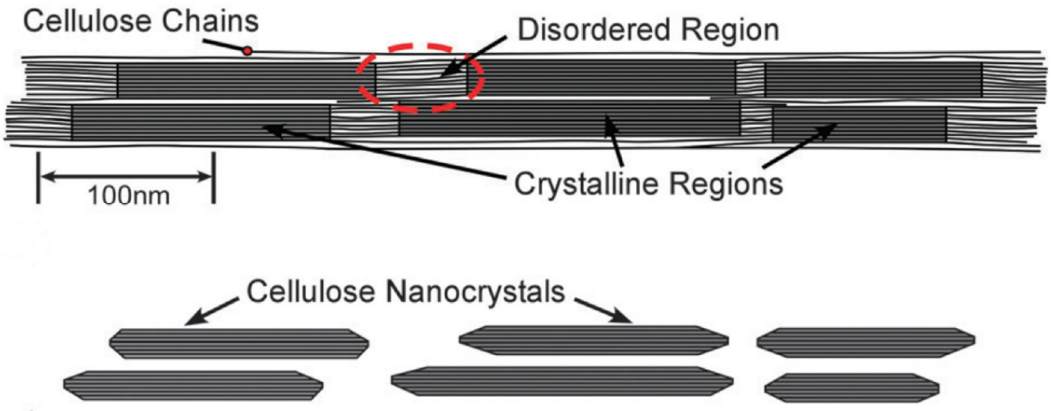

Figure 2-4. During acid hydrolysis, the more accessible disordered regions of cellulose are cleaved first, leaving behind CNCs – the crystalline cellulose particles. Reproduced from reference 2.

A comparison of the two types of nanocelluloses (CNCs and CNFs) indicates, firstly, that CNC dimensions are generally smaller than those of CNFs. Although both types of nanocelluloses have different aspect ratios, they have similar elastic moduli of 57-220

GPa[7] and 143-150 GPa[2] for CNCs and CNFs, respectively. If these nanocelluloses are incorporated into thin films, their elastic moduli are also very similar within composites (CNCs: 0.0005-33.5 GPa; CNFs: 0.003-17.2 GPa)[2,12,13] and within nanocellulose-only films (CNCs: 5-10 GPa; CNFs: 6-15 GPa).[2] From this, we see that there are similarities in the properties of CNFs and CNCs; however, both types of nanocelluloses also have distinct differences in several of their properties. For instance, CNCs are more rigid (less flexible) and have lower porosity than CNFs.[4,5,7] These properties of CNCs add strength, function, and value to many hybrid materials that incorporate these crystalline nanoparticles, such as emulsions, hydrogels, foams, paints, adhesives and thin films.[1,14]

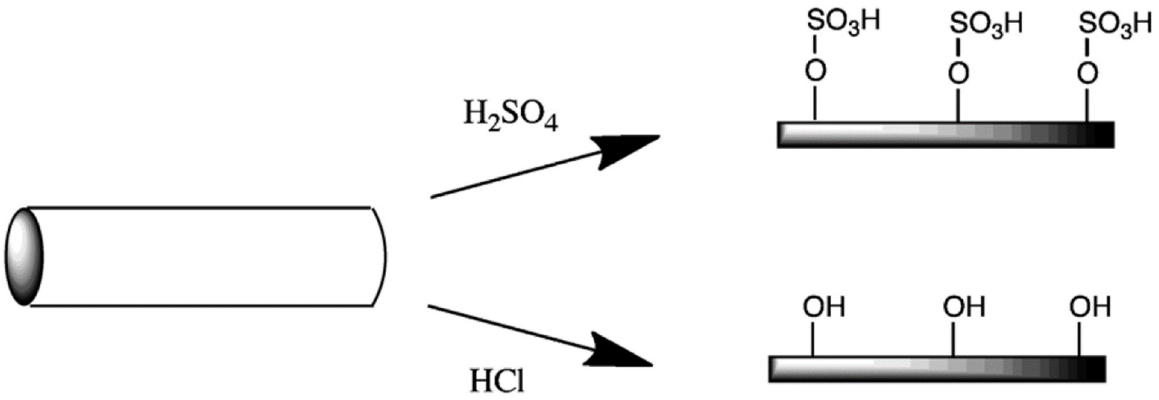

Figure 2-5. Schematic outlining the various surface functionalities that can be introduced onto CNCs, based on the hydrolysis conditions used to extract these nanoparticles from cellulose. Reproduced from reference 2.

2.2. Preparation of CNC-Based Thin Films

CNC-based thin films (with thicknesses in the nanometer to micron range) are prepared to study their 3-dimensonal structure, solvent adsorption and swelling, and

interfacial behaviour in the presence of polymers, surfactants, and inorganic compounds.[15–17] CNCs can be used to prepare biocomposite films or all-nanoparticle films, which consist of a network of nanoparticles that strongly interact with other materials (*e.g.*, polymers, other types of nanoparticles) or nanoparticles that interact with one another through intermolecular and surface forces. In this way, films with varying compositions and properties (*e.g.*, mechanical, physical, chemical, electrical, rheological, barrier, thermal, optical) can be prepared.[2,15–18] Sections 2.2.1. and 2.2.2. outline methods used to fabricate cellulose-based surfaces, in the form of CNC biocomposite films and all-CNC films.

2.2.1. CNC Biocomposite Films

CNC biocomposite films are defined as thin films composed of CNCs and one or more materials, such as polymers, surfactants, quantum dots, or metallic nanoparticles.[17,19–26] Working with different materials results in films with tailorable properties that have a variety of applications in the areas of disposable packaging, optical coatings, biosensors, membrane filtration devices, fiber membranes, electrodes, tissue engineering scaffolds, antimicrobial films, food packaging materials, and paper-based electronics.[2,14,18]

Methods used to fabricate CNC biocomposites include layer-by-layer (LbL) deposition, solution-casting, melt-compounding, and electrospinning.[2,14,16] In the LbL process, layers of complementary molecules are consecutively adsorbed onto a substrate, where this adsorption occurs through either electrostatic interactions, hydrogen bonding, van der Waals forces, or a combination of these interactions.[14,27,28] LbL depositions can be performed using two methods – dip-coating and spin-coating.[14] In solution-casting, a CNC

suspension is mixed with the material(s) of interest, where the mixture is cast onto a substrate and allowed to dry via evaporation, freeze-drying, extrusion, or compression molding.[1,2] When using melt-compounding, polymer melts are incorporated with CNCs during thermo-mechanical mixing, after which extrusion of this mixture produces a CNC-polymer matrix composite. Lastly, in electrospinning, CNC-polymer mixtures are formed in varying ratios and extruded via a high voltage applied between the syringe holding the mixture and a grounded target. This causes a CNC-polymer jet to form and accelerate towards the target. The solvent evaporation and whipping motion of the jet forms fibers of varying widths, thicknesses, and morphologies, depending on the materials used in the mixture. Chapter 3 of this thesis presents a study on CNC-based biocomposite films which are fabricated using the LbL deposition technique.

2.2.2. All-CNC Films

The properties of all-CNC thin films vary, where they are only affected by the chemical and structural aspects of the rod-like CNCs. The resulting properties of all-CNC films are also dependent on the film fabrication method used, where films can be formed by dip-coating a substrate in a CNC suspension, or by solvent-casting and drying a CNC suspension onto a substrate.[2,16,29] Solvent-cast suspensions are dried through evaporation, vacuum filtration, pressing, freeze-drying, solvent exchange, or a combination of these methods,[2] where some of these methods are identical to those mentioned in section 2.2.1. CNCs can adopt different orientations in thin films, which include chiral nematic, isotropic, and uniaxial (linear or radial) orientations.[1,2]

Above a critical concentration, CNCs have a self-assembling tendency in suspension, where they form a chiral nematic liquid crystalline orientation as a result of their rod-like structure.[1,9,30] Suspensions beyond this critical concentration spontaneously form two phases – an upper phase (isotropic) where the CNCs are isotropically oriented, and a lower phase (anisotropic) where the CNCs exhibit chiral nematic order (Figure 2-6a).[30] The chiral nematic ordered phase is formed by stacked planes of CNCs aligned in one direction (defined as the director), where the director of each consecutive plane is slightly rotated anticlockwise. The axial distance required for the plane director to undergo a full rotation corresponds to the chiral nematic pitch of the CNCs, which can be characterized by the fingerprint texture seen in polarized optical microscopy (POM) images of the anisotropic phase (Figure 2-6b). Chiral nematic CNC suspensions that are solvent-cast onto a substrate and slowly evaporated under controlled conditions will form films that retain this chiral nematic order. Chapter 4 of this thesis discusses the fabrication of all-CNC films with chiral nematic CNC order, where CNC suspensions are dried slowly under vacuum.

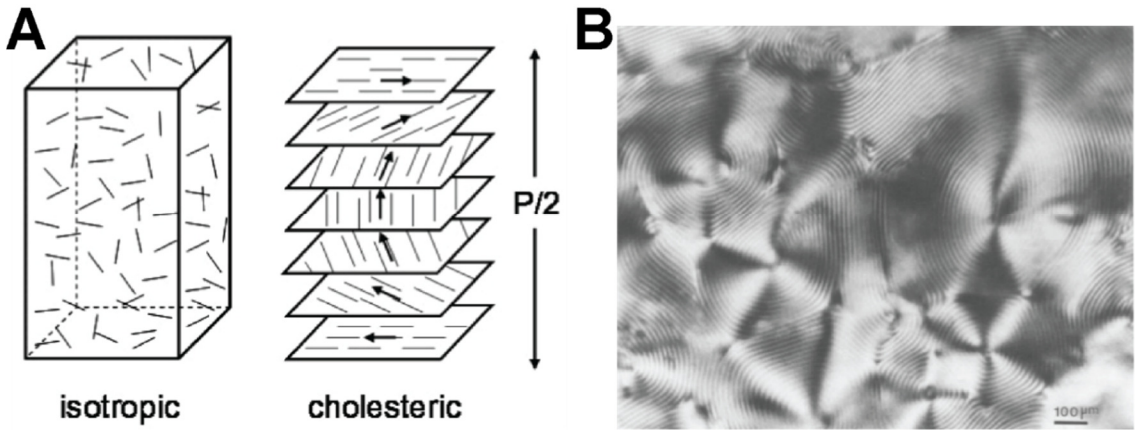

Figure 2-6. Chiral nematic ordering of CNCs in suspension. (A) Above a critical concentration, CNC suspensions will separate into an upper isotropic phase (left) and a lower anisotropic, or cholesteric, phase (right). (B) When the anisotropic phase of a CNC suspension is imaged by polarized optical microscopy (POM), a characteristic fingerprint texture is seen. Reproduced from reference 30.

All-CNC films can also consist of nanoparticle orientations that are isotropic (random). One way to achieve this is through the adsorption of layers of CNCs onto a substrate, where the substrate is dip-coated into an isotropic CNC suspension (Figure 2-7a).[29] Isotropic CNC orientations can also be achieved in films by drying a solvent-cast CNC suspension very quickly, where the CNCs do not have sufficient time to self-assemble into a preferred orientation. In Chapter 4, all-CNC films with isotropic nanoparticle orientations are produced by quickly drying solvent-cast CNC suspensions using heat.

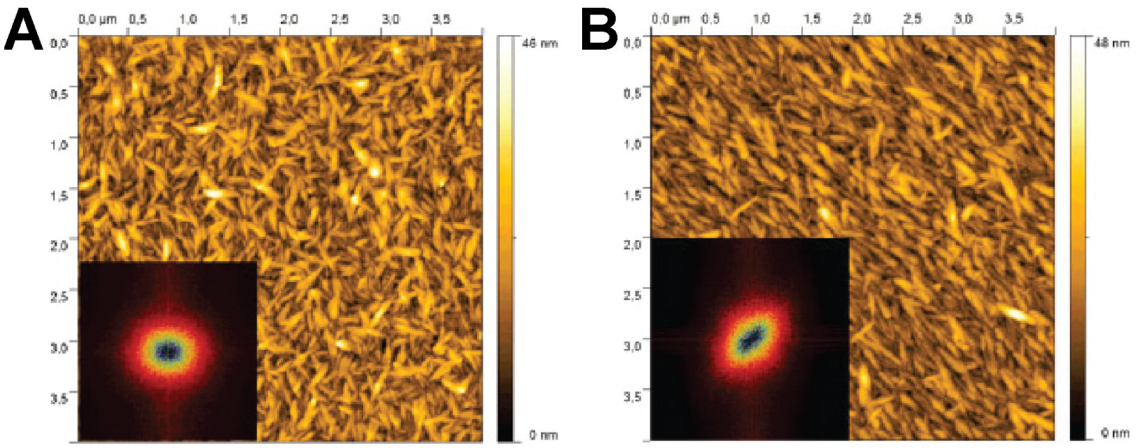

Figure 2-7. Atomic force microscopy (AFM) height images of CNC-based films prepared by dip-coating of a substrate. (A) Films prepared from the isotropic phase of CNC suspensions have isotropically oriented CNCs, while (B) films prepared from the anisotropic phase of suspensions have linearly oriented CNCs. A 2D fast Fourier transform of these films confirms that the CNCs are oriented isotropically and linearly, respectively. Reproduced from reference 31.

Lastly, films with uniaxial (linear/radial) CNC alignments can be fabricated using applied shear forces, dip-coating, Langmuir-Blodgett (LB) deposition, Langmuir-Schaeffer (LS) deposition, applied external magnetic fields, applied electric fields, and spin-coating.[29,31–35] Applied shear forces such as shear flow, rotation of a cylindrical vial, and convective shear forces cause CNCs in suspension to linearly orient parallel or perpendicular to the applied shear force.[29] The direction of nanoparticle orientation depends on the type of applied force, the concentration of CNC suspension, and the substrate used, which results in ordered suspensions can be dried down to all-CNC films that retain their linear orientation. When using dip-coating, a substrate is submerged into a CNC suspension with anisotropic order, where the films produced have CNCs that are linearly aligned parallel to the substrate surface (Figure 2-7b).[31] In LB[32] and LS[33] depositions, a monolayer of CNCs is deposited from suspension onto a substrate through vertical[32] or horizontal[33]

depositions, respectively, to produce films with linearly aligned CNCs.[32,33] When working with dilute (isotropic) CNC suspensions in the presence of an applied magnetic field, the long axis of the CNCs aligns perpendicular to applied field to form radially oriented suspensions.[34] These suspensions can then be dried down to all-CNC films that retain this radial nanoparticle alignment. This can also be achieved using an applied electric field, where the CNCs will align parallel to the applied field as a result of their electrical anisotropy.[35] Another way to produce films with radially aligned CNCs is through spin-coating of a CNC suspension onto a substrate,[36,37] which is the method used in Chapter 4 to produce all-CNC films with uniaxially aligned nanoparticles.

2.3. CNC Mechanical Properties and their Limitations

2.3.1. Mechanical Properties of CNCs

The mechanical properties of crystalline cellulose have been studied using methods such as X-ray diffraction, inelastic X-ray scattering, atomic force microscopy (AFM), Raman spectroscopy, and other modeling techniques.[2,3] However, the values determined are debated due to the limitations and assumptions of these techniques. Attempts to quantify the elastic modulus of crystalline cellulose have resulted in values in the 57-220 GPa and 9-50 GPa range for the axial and transverse directions, respectively.[2] The mechanical performance of individual CNC particles has also been quantified by AFM[38] and Raman spectroscopy,[39] with axial elastic moduli values ranging from 57-143 GPa.[2] Based on these results, the specific modulus of nanocellulose is comparable to that of Kevlar or steel.[1]

2.3.2. Mechanical Properties of CNC-Based Thin Films

The mechanical properties of CNC-based thin films have been assessed using techniques such as dynamic mechanical analysis, tensile testing, buckling mechanics, and modeling methods.[2,13] CNC biocomposite films have been reported with elastic moduli of 0.0005-33.5 GPa,[2,13,40] where some of these values change with relative humidity.[13] The upper bound elastic moduli of biocomposite films consisting of isotropically and radially oriented cellulose nanoparticles have been estimated through modelling, and have values of 8.8 and 17.2 GPa, respectively (assuming 10 wt% of cellulose nanoparticles).[2] These results suggest that the film's mechanical properties will increase as more nanoparticle order is introduced into the film. Experimentally, this has been seen in CNC-cellulose II composite films (with 25 wt% of CNCs), where films with isotropically oriented CNCs have an elastic modulus of 9.9 GPa and films with radially aligned CNCs have a modulus of 33.5 GPa.[40] When considering all-CNC films, little work has evaluated their mechanical properties, and studies that have looked at these properties report elastic moduli to be 5-10 GPa.[2] These values are much lower than the estimated upper bound values calculated by Moon *et al*., from which they determine that cellulose nanoparticle films with isotropic or uniaxial nanoparticle orientations have upper bound moduli in the range of 50-60 GPa or 100-150 GPa, respectively.[2] There are two potential reasons that the measured elastic moduli values are lower than the upper bound values: 1) there are less interfacial nanoparticle-nanoparticle interactions in the films than the model predicts, and 2) in films with aligned nanoparticles, there is less uniaxial nanoparticle alignment present than assumed by the model.

2.4. Structuring Methods to Assess Thin Film Mechanical Properties

Methods such as nanoindentation, dynamic mechanical thermal analysis, and three-point bending flexural tests are routinely used to study the mechanical performance of thin films.[41] Advantages to using these methods include simple sample preparation requirements and relatively straightforward sample testing. However, drawbacks to using these techniques include: low precision, lack of sensitivity when it comes to measuring films of sub-micron thicknesses, and stringent sample requirements that are not suitable to many thin films and the way they are prepared (*e.g.*, can only assess free-standing films, cannot quantify films that are soft and "sticky"). Many of these methods are well-suited to assessing free-standing thin films, but cannot accurately quantify films adhered to an underlying substrate or films approaching sub-micron thicknesses. As an alternative, structuring methods are being used to assess the mechanical performance of sub-micron thin films, and make use of soft polymeric substrates or shape-memory substrates in order to overcome the limitations of conventional methods.[12,42,43] These methods also have limitations, however, where they cannot measure stand-alone films, and can be challenging to use when trying to quantify the mechanical properties of films composed of hygroscopic materials, since water is likely retained in these films.

2.4.1. External Compression of a Polymeric Substrate

Soft polymers, such as poly(dimethylsiloxane) (PDMS), can be used as substrates for the deposition and structuring of thin films and coatings.[42,44,45] Thin films with high mechanical moduli relative to the soft substrate can be structured when an external

compressive stress is applied on the substrate. Examples of compressive stress include the thermally induced contraction of a heated substrate or an applied compressive strain. The underlying substrate compresses, which causes the film to buckle and form wrinkled features. Different types of structuring occur depending on the type of compression the substrate undergoes (*e.g.,* films can form uniaxial or isotropic wrinkles, Figure 2-8).[46] A wide range of films have been structured using this method, including films consisting of polymers, organosilicates, metals, and organic nanomaterials.[12,42,44,45,47] Examples of organic nanomaterial-based films are nanocellulose-containing composites such as CNF- and CNC-based composite films, which have been uniaxially structured through uniaxially-applied compressive stresses.[12,13]

In addition to forming wrinkled thin films, this structuring approach can be used to calculate the elastic modulus of uniaxially wrinkled films, using the strain-induced elastic buckling instability for mechanical measurements (SIEBIMM) technique.[42,48] Knowledge of the substrate's elastic modulus (E_s), Poisson's ratio for both the substrate (ν_s) and the film (ν_s), film thickness (h), and wavelength of the uniaxial wrinkles (λ) allows for the determination of the film's elastic modulus (E_f) using Equation 2.1. The elastic moduli for polymeric, organosilicate, and nanocellulose films have been studied using this method,[12,13,42] where examples of nanocellulose films include CNF and CNC biocomposite films.[12,13] The elastic moduli of CNF-polyethyleneimine (PEI) films are reported to be 17.2 ± 1.2 GPa and 1.5 ± 0.2 GPa at 0% and 50% relative humidity, respectively,[12] while CNC-PEI films have elastic modulus values of 3.5 ± 0.3 GPa, 12 ± 1 GPa, and 16 ± 5 GPa at 64%, 42%, and 30% relative humidity, respectively.[13] Therefore, the disadvantage of

working with nanocellulose-based composite films is that their mechanical properties change with relative humidity – something which is not a limitation of the SIEBIMM approach itself. This structuring approach is a suitable alternative to conventional methods for determining the elastic moduli of a wide range of thin films, but is not the most suitable method to use when working with hygroscopic thin films.[12,13,42]

$$E_f = 3E_s \frac{(1-\nu_f{}^2)}{(1-\nu_s{}^2)} \left(\frac{\lambda}{2\pi h}\right)^3 \tag{2.1}$$

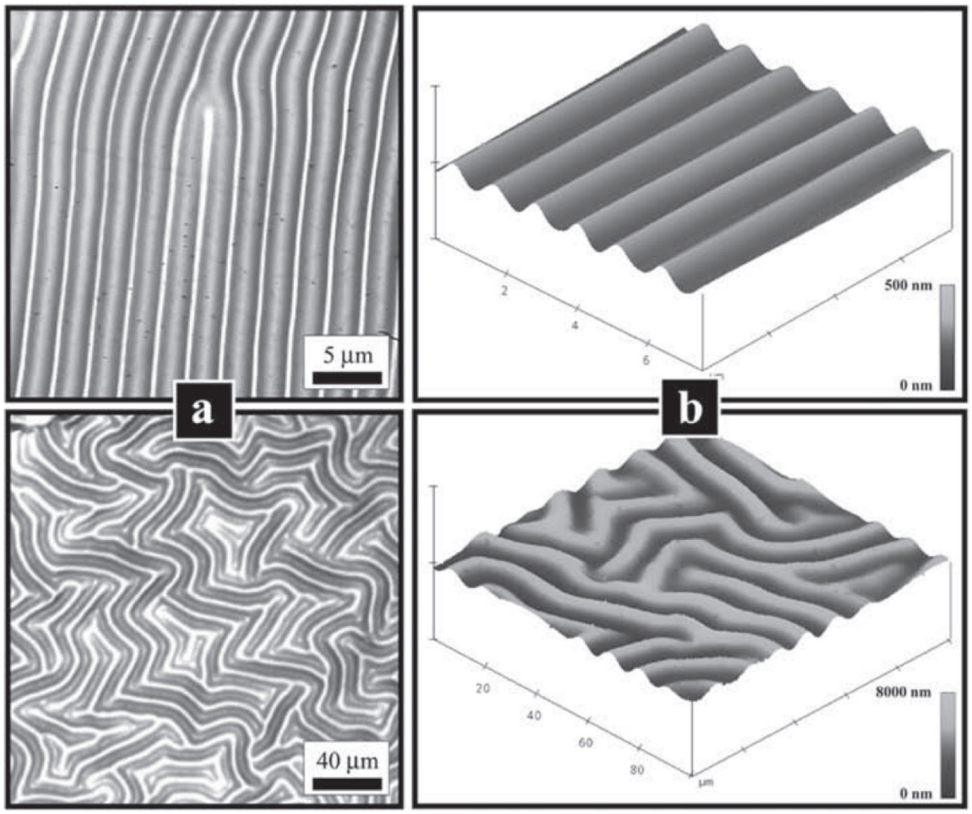

Figure 2-8. (A) Optical microscopy and (B) AFM images of a uniaxially wrinkled film (top) and an isotropically wrinkled film (bottom) on a soft underlying substrate. Reproduced from reference 46.

2.4.2. Structuring through Shape-Memory Polymer Thermal Shrinkage

Another structuring method used to form wrinkled thin films involves preparing films on pre-stressed, shape-memory polymer substrates.[43,49,50] Shape-memory substrates that are used include pre-stressed polystyrene (PS) and polyolefin (PO) sheets which, when heated above their glass transition temperature, retract (or shrink) to their "original" shape.[49,50] PS and PO sheets shrink isotropically to 40% and 95% of their original size, respectively. During the shrinking process, compressive stress is generated by the contracting substrate. When these soft substrates are prepared with a stiff film on their surface, this compressive stress is released through uniaxial or isotropic wrinkling of the film (Figure 2-9).[43,49] Similar to the structuring approach discussed in Section 2.4.1., this shape-memory polymer structuring approach is amenable to a wide range of films where, for instance, wrinkled metallic, glassy, and carbon nanotube films can be fabricated.[43,49,51,52] This structuring approach is unique from the method discussed in Section 2.4.1., where structured films produced using this technique are stable and irreversibly plastically deformed. Removal of the external compressive stress or separation from the underlying substrate does not compromise the integrity of the wrinkled features.[53]

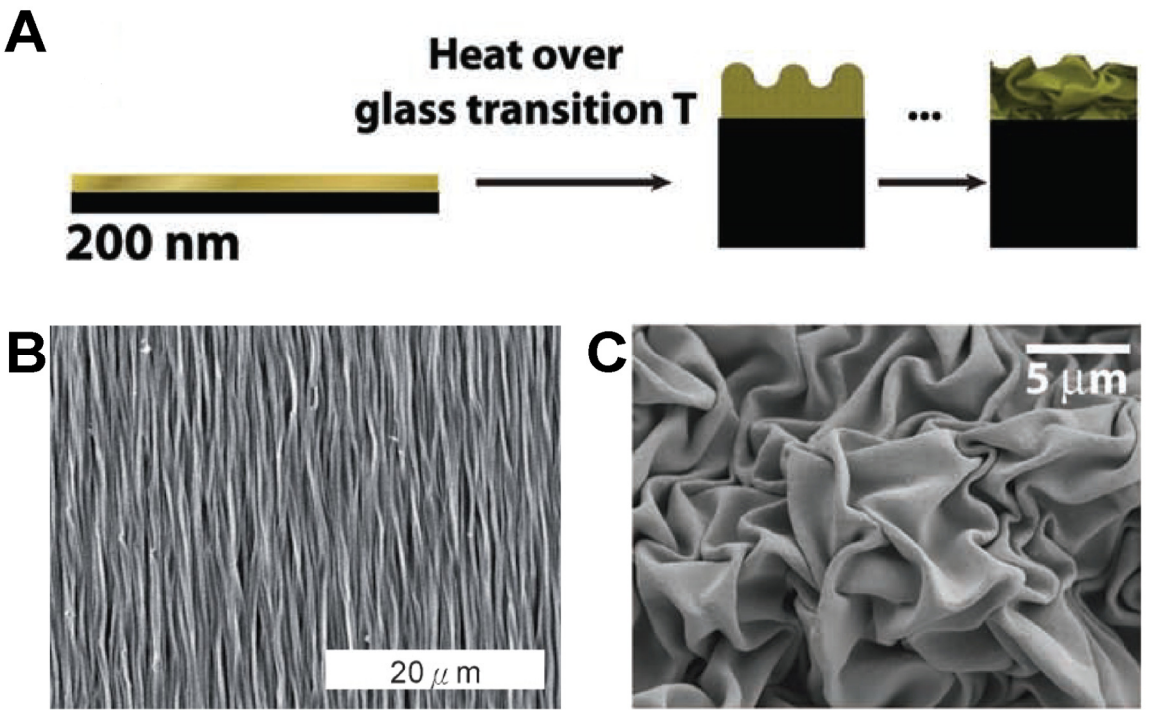

Figure 2-9. (A) Schematic showing a thin gold film deposited on a pre-stressed polystyrene (PS) substrate, which structures when the substrate is shrunken above its glass transition temperature. Scanning electron microscopy (SEM) images are shown of (A) uniaxial (thickness = 10 nm) and (B) biaxial (thickness = 200 nm) wrinkled gold films, following the PS shrinking step. A and C are reproduced from reference 49, B is reproduced from reference 43.

In addition to forming stable wrinkled films, this structuring method can also be used to calculate the elastic modulus of thin films.[43] Referring back to Equation 1 (section 2.4.1.), a parameter η can defined (Equation 2.2)[43,48] from which $\eta^{1/3}h \propto \lambda$. This indicates that for a film of a certain stiffness, as its thickness is increased, the resulting wrinkled features following structuring have larger wavelength values. When biaxial strains are applied in a system, another parameter needs to be taken into account – the persistence length ξ, which is the distance over which the isotropic wrinkles lose memory of their original propagation direction.[48] The persistence length is difficult to measure directly, and

so it can be scaled to η, where $\xi \propto \eta^{2/3}h$.[43,48] This indicates that the persistence length increases proportionally with wrinkle wavelength. In order to determine η, plots of film thickness and wrinkle length need to be generated, where the slopes of these curves are equal to $\eta^{2/3}$, keeping in mind that this parameter is scaled from the persistence length when biaxial strains are applied.[43] Once η is calculated and the elastic modulus of the substrate is known, the film's elastic modulus can be calculated using $\eta \approx \frac{E_f}{E_s}$. This structuring approach has been used to study the mechanical properties of wrinkled metallic films,[43] but has not been used to wrinkle nanocellulose-based thin films and study their mechanical properties. Therefore, in this thesis, the PS structuring approach is used to study the mechanical properties of CNC biocomposites and all-CNC films, as discussed in Chapters 3 and 4.

$$\eta = \frac{E_f\left(1-\nu_s^2\right)}{3E_s\left(1-\nu_f^2\right)} \tag{2.2}$$

2.5. References

(1) Habibi, Y.; Lucia, L. A.; Rojas, O. J. Cellulose Nanocrystals: Chemistry, Self-Assembly, and Applications. *Chem. Rev.* **2010**, *110* (6), 3479–3500.

(2) Moon, R. J.; Martini, A.; Nairn, J.; Simonsen, J.; Youngblood, J. Cellulose Nanomaterials Review: Structure, Properties and Nanocomposites. *Chem. Soc. Rev.* **2011**, *40*, 3941–3994.

(3) Eichhorn, S. J.; Dufresne, A.; Aranguren, M.; Marcovich, N. E.; Capadona, J. R.; Rowan, S. J.; Weder, C.; Thielemans, W.; Roman, M.; Renneckar, S.; Gindl, W.; Veigel, S.; Keckes, J.; Yano, H.; Abe, K.; Nogi, M.; Nakagaito, A. N.; Mangalam, A.; Simonsen, J.; Benight, A. S.; Bismarck, A.; Berglund, L. A.; Peijs, T. Review: Current International Research into Cellulose Nanofibres and Nanocomposites. *J. Mater. Sci.* **2010**, *45* (1), 1–33.

(4) Mariano, M.; El Kissi, N.; Dufresne, A. Cellulose Nanocrystals and Related Nanocomposites: Review of Some Properties and Challenges. *J. Polym. Sci., Part B Polym. Phys.* **2014**, *52*, 791–806.

(5) Klemm, D.; Heublein, B.; Fink, H.-P.; Bohn, A. Cellulose: Fascinating Biopolymer and Sustainable Raw Material. *Angew. Chemie Int. Ed.* **2005**, *44*, 3358–3393.

(6) Klemm, D.; Kramer, F.; Moritz, S.; Lindström, T.; Ankerfors, M.; Gray, D.; Dorris, A. Nanocelluloses: A New Family of Nature-Based Materials. *Angew. Chemie Int. Ed.* **2011**, *50*, 5438–5466.

(7) Abdul Khalil, H. P. S.; Davoudpour, Y.; Islam, M. N.; Mustapha, A.; Sudesh, K.; Dungani, R.; Jawaid, M. Production and Modification of Nanofibrillated Cellulose Using Various Mechanical Processes: A Review. *Carbohydr. Polym.* **2014**, *99*, 649–665.

(8) Lee, H. V.; Hamid, S. B. A.; Zain, S. K. Conversion of Lignocellulosic Biomass to Nanocellulose: Structure and Chemical Process. *Sci. World J.* **2014**, *2014*, 1–20.

(9) Revol, J.-F.; Bradford, H.; Giasson, J.; Marchessault, R. H.; Gray, D. G. Helicoidal Self-Ordering of Cellulose Microfibrils in Aqueous Suspension. *Int. J. Biol. Macromol.* **1992**, *14*, 170–172.

(10) Araki, J.; Wada, M.; Kuga, S.; Okano, T. Flow Properties of Microcrystalline Cellulose Suspension Prepared by Acid Treatment of Native Cellulose. *Colloids Surfaces A Physicochem. Eng. Asp.* **1998**, *142*, 75–82.

(11) Lagerwall, J. P. F.; Schütz, C.; Salajkova, M.; Noh, J.; Hyun Park, J.; Scalia, G.; Bergström, L. Cellulose Nanocrystal-Based Materials: From Liquid Crystal Self-Assembly and Glass Formation to Multifunctional Thin Films. *NPG Asia Mater.* **2014**, *6*, e80.

(12) Cranston, E. D.; Eita, M.; Johansson, E.; Netrval, J.; Salajková, M.; Arwin, H.; Wågberg, L. Determination of Young's Modulus for Nanofibrillated Cellulose Multilayer Thin Films Using Buckling Mechanics. *Biomacromolecules* **2011**, *12*, 961–969.

(13) Kan, K. H. M.; Cranston, E. D. Mechanical Testing of Thin Film Nanocellulose Composites Using Buckling Mechanics. *TAPPI J.* **2013**, *12* (4), 9–17.

(14) Martin, C.; Jean, B. Nanocellulose/polymer Multilayered Thin Films: Tunable Architectures towards Tailored Physical Properties. *Nord. Pulp Pap. Res. J.* **2014**, *29* (1), 19–30.

(15) Kontturi, E.; Tammelin, T.; Österberg, M. Cellulose—model Films and the Fundamental Approach. *Chem. Soc. Rev.* **2006**, *35*, 1287–1304.

(16) Cranston, E. D.; Gray, D. G. Model Cellulose I Surfaces: A Review. In *Model Cellulosic Surfaces*; Roman, M., Ed.; ACS Symposium Series; ACS Publishing: Washington, DC, 2009; pp 75–93.

(17) Aulin, C.; Ahola, S.; Josefsson, P.; Nishino, T.; Hirose, Y.; Österberg, M.; Wågberg, L. Nanoscale Cellulose Films with Different Crystallinities and Mesostructures—Their Surface Properties and Interaction with Water. *Langmuir* **2009**, *25* (13), 7675–7685.

(18) Julkapli, N. M.; Bagheri, S. Progress on Nanocrystalline Cellulose Biocomposites. *React. Funct. Polym.* **2017**, *112*, 9–21.

(19) Podsiadlo, P.; Sui, L.; Elkasabi, Y.; Burgardt, P.; Lee, J.; Miryala, A.; Kusumaatmaja, W.; Carman, M. R.; Shtein, M.; Kieffer, J.; Lahann, J.; Kotov, N. A. Layer-by-Layer Assembled Films of Cellulose Nanowires with Antireflective Properties. *Langmuir* **2007**, *23* (15), 7901–7906.

(20) Liu, H.; Song, J.; Shang, S.; Song, Z.; Wang, D. Cellulose Nanocrystal/Silver Nanoparticle Composites as Bifunctional Nano Fillers within Waterborne Polyurethane. *Appl. Mater. Interfaces* **2012**, *4*, 2413–2419.

(21) Cerclier, C.; Guyomard-Lack, A.; Moreau, C.; Cousin, F.; Beury, N.; Bonnin, E.; Jean, B.; Cathala, B. Coloured Semi-Reflective Thin Films for Biomass-Hydrolyzing Enzyme Detection. *Adv. Mater.* **2011**, *23*, 3791–3795.

(22) Edwards, J. V.; Prevost, N.; French, A.; Concha, M.; Delucca, A.; Wu, Q. Nanocellulose-Based Biosensors: Design, Preparation, and Activity of Peptide-Linked Cotton Cellulose Nanocrystals Having Fluorimetric and Colorimetric Elastase Detection Sensitivity. *Engineering* **2013**, *5*, 20–28.

(23) Granberg, H.; Coppel, L. G.; Eita, M.; De Mayolo, E. A.; Arwin, H.; Wågberg, L. Dynamics of Moisture Interaction with Polyelectrolyte Multilayers Containing Nanofibrillated Cellulose. *Nord. Pulp Pap. Res. J.* **2012**, *27* (2), 496–499.

(24) Dammak, A.; Moreau, C.; Beury, N.; Schwikal, K.; Winter, H. T.; Bonnin, E.; Saake, B.; Cathala, B. Elaboration of Multilayered Thin Films Based on Cellulose Nanocrystals and Cationic Xylans: Application to Xylanase Activity Detection. *Holzforschung* **2013**, *67* (5), 579–586.

(25) Guyomard-Lack, A.; Cerclier, C.; Beury, N.; Jean, B.; Cousin, F.; Moreau, C.; Cathala, B. Nano-Structured Cellulose Nanocrystals-Xyloglucan Multilayered Films for the Detection of Cellulase Activity. *Eur. Phys. J. Spec. Top.* **2012**, *213*, 291–294.

(26) Chen, L.; Lai, C.; Marchewka, R.; Berry, R. M.; Tam, K. C. Use of CdS Quantum Dot-Functionalized Cellulose Nanocrystal Films for Anti-Counterfeiting Applications. *Nanoscale* **2016**, *8*, 13288–13296.

(27) Decher, G. Fuzzy Nanoassemblies: Toward Layered Polymeric Multicomposites. *Sci.* **1997**, *277* (5330), 1232–1237.

(28) *Multilayer Thin Films: Sequential Assembly of Nanocomposite Materials*; Decher, G., Schlenoff, J. B., Eds.; John Wiley & Sons: Hoboken, NJ, 2006.

(29) Abitbol, T.; Cranston, E. D. Directed Assembly of Oriented Cellulose Nanocrystal Films. In *Handbook of Green Materials*; World Scientific: Hackensack, NJ, 2014; Vol. 3, pp 79–103.

(30) Abitbol, T.; Cranston, E. D. Chiral Nematic Self-Assembly of Cellulose Nanocrystals in Suspensions and Solid Films. In *Handbook of Green Materials*; World Scientific: Hackensack, NJ, 2014; Vol. 3, pp 37–56.

(31) Jean, B.; Dubreuil, F.; Heux, L.; Cousin, F. Structural Details of Cellulose Nanocrystals/Polyelectrolytes Multilayers Probed by Neutron Reflectivity and AFM. *Langmuir* **2008**, *24* (7), 3452–3458.

(32) Habibi, Y.; Foulon, L.; Aguié-Béghin, V.; Molinari, M.; Douillard, R. Langmuir-Blodgett Films of Cellulose Nanocrystals: Preparation and Characterization. *J. Colloid Interface Sci.* **2007**, *316*, 388–397.

(33) Habibi, Y.; Hoeger, I.; Kelley, S. S.; Rojas, O. J. Development of Langmuir-Schaeffer Cellulose Nanocrystal Monolayers and Their Interfacial Behaviors. *Langmuir* **2010**, *26* (2), 990–1001.

(34) Revol, J.-F.; Godbout, L.; Dong, X.-M.; Gray, D. G.; Chanzy, H.; Maret, G. Chiral Nematic Suspensions of Cellulose Crystallites; Phase Separation and Magnetic Field Orientation. *Liq. Cryst.* **1994**, *16* (1), 127–134.

(35) Bordel, D.; Putaux, J.-L.; Heux, L. Orientation of Native Cellulose in an Electric Field. *Langmuir* **2006**, *22*, 4899–4901.

(36) Edgar, C. D.; Gray, D. G. Smooth Model Cellulose I Surfaces from Nanocrystal Suspensions. *Cellulose* **2003**, *10*, 299–306.

(37) Lefebvre, J.; Gray, D. G. AFM of Adsorbed Polyelectrolytes on Cellulose I Surfaces Spin-Coated on Silicon Wafers. *Cellulose* **2005**, *12*, 127–134.

(38) Lahiji, R. R.; Xu, X.; Reifenberger, R.; Raman, A.; Rudie, A.; Moon, R. J. Atomic Force Microscopy Characterization of Cellulose Nanocrystals. *Langmuir* **2010**, *26* (6), 4480–4488.

(39) Šturcová, A.; Davies, G. R.; Eichhorn, S. J. Elastic Modulus and Stress-Transfer Properties of Tunicate Cellulose Whiskers. *Biomacromolecules* **2005**, *6* (2), 1055–1061.

(40) Gindl, W.; Keckes, J. Drawing of Self-Reinforced Cellulose Films. *J. Appl. Polym. Sci.* **2007**, *103*, 2703–2708.

(41) *Front Matter, in Polymer Composites: Volume 2*; Thomas, S., Joseph, K., Malhotra,

S. K., Goda, K., Sreekala, M. S., Eds.; Wiley-VCH Verlag GmbH & Co. KGaA: Weinheim, Germany, 2013.

(42) Stafford, C. M.; Harrison, C.; Beers, K. L.; Karim, A.; Amis, E. J.; VanLandingham, M. R.; Kim, H.-C.; Volksen, W.; Miller, R. D.; Simonyi, E. E. A Buckling-Based Metrology for Measuring the Elastic Moduli of Polymeric Thin Films. *Nat. Mater.* **2004**, *3* (8), 545–550.

(43) Fu, C.-C.; Grimes, A.; Long, M.; Ferri, C. G. L.; Rich, B. D.; Ghosh, S.; Ghosh, S.; Lee, L. P.; Gopinathan, A.; Khine, M. Tunable Nanowrinkles on Shape Memory Polymer Sheets. *Adv. Mater.* **2009**, *21* (44), 4472–4476.

(44) Volynskii, A. L.; Bazhenov, S.; Lebedeva, O. V.; Bakeev, N. F. Mechanical Buckling Instability of Thin Coatings Deposited on Soft Polymer Substrates. *J. Mater. Sci.* **2000**, *35*, 547–554.

(45) Bowden, N.; Brittain, S.; Evans, A. G.; Hutchinson, J. W.; Whitesides, G. M. Spontaneous Formation of Ordered Structures in Thin. *Nature* **1998**, *393*, 146–149.

(46) Chung, J. Y.; Nolte, A. J.; Stafford, C. M. Surface Wrinkling: A Versatile Platform for Measuring Thin-Film Properties. *Adv. Mater.* **2011**, *23* (3), 349–368.

(47) Shao, Y.; Brook, M. A. Structured Metal Film on Silicone Elastomers. *J. Mater. Chem.* **2010**, *4* (8), 1166–1169.

(48) Groenewold, J. Wrinkling of Plates Coupled with Soft Elastic Media. *Physica A* **2001**, *298*, 32–45.

(49) Gabardo, C. M.; Zhu, Y.; Soleymani, L.; Moran-Mirabal, J. M. Bench-Top Fabrication of Hierarchically Structured High-Surface-Area Electrodes. *Adv. Funct. Mater.* **2013**, *23* (24), 3030–3039.

(50) Nguyen, D.; Taylor, D.; Qian, K.; Norouzi, N.; Rasmussen, J.; Botzet, S.; Lehmann, M.; Halverson, K.; Khine, M. Better Shrinkage than Shrinky-Dinks. *Lab Chip* **2010**, *10*, 1623–1626.

(51) Zhu, Y.; Boyle, J. P.; Bonin, K.; Chowdhury, T.; Moran-Mirabal, J. M. Micro/nanostructured SiO2 and TiO2 Films Fabricated through Polymer Shrinking as Tunable Topography Substrates for Cell Studies. *Integr. Biol.* Submitted.

(52) Park, S.-J.; Kim, J.; Chu, M.; Khine, M. Highly Flexible Wrinkled Carbon Nanotube Thin Film Strain Sensor to Monitor Human Movement. *Adv. Mater. Technol.* **2016**, *1* (5), 1600053.

(53) Zhu, Y.; Moran-Mirabal, J. Highly Bendable and Stretchable Electrodes Based on Micro/Nanostructured Gold Films for Flexible Sensors and Electronics. *Adv. Electron. Mater.* **2016**, *2*, 1500345.

Chapter 3 – Beyond Buckling: Humidity-Independent Measurement of the Mechanical Properties of Green Nanobiocomposite Films

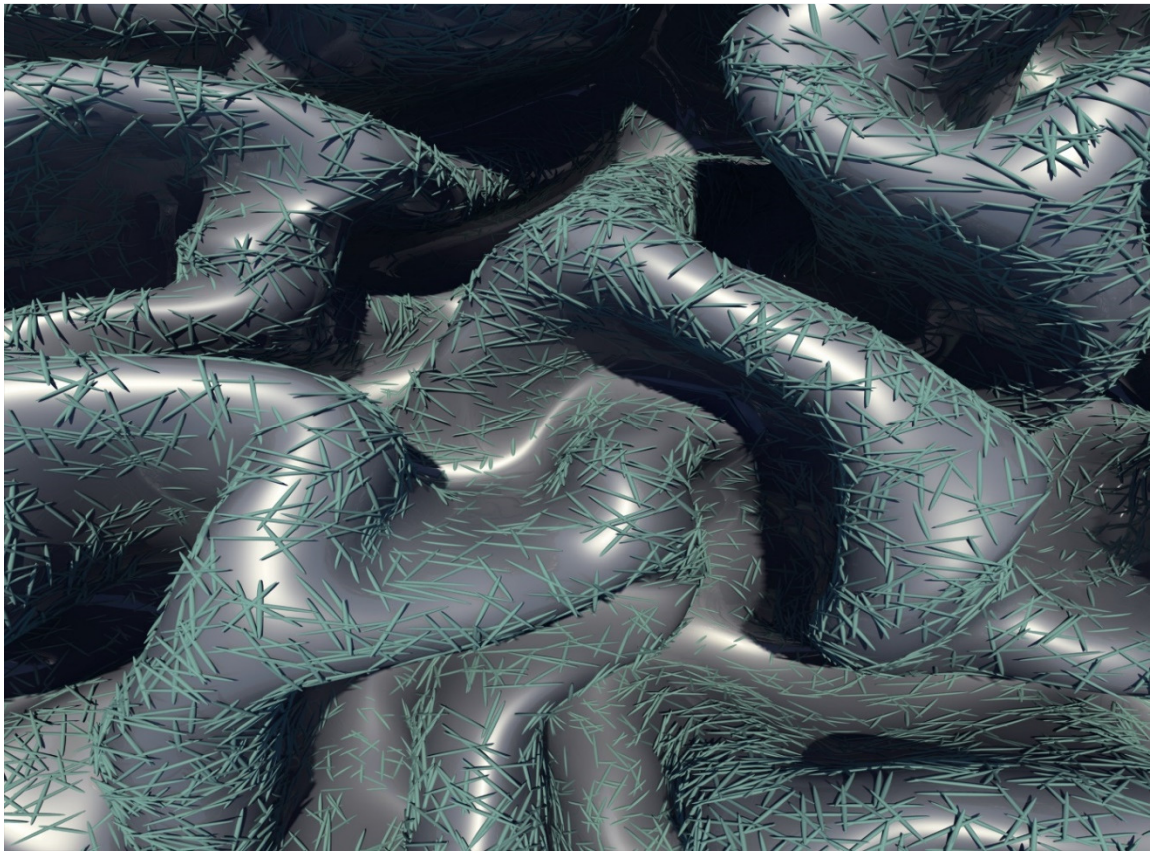

Part of the contents presented in this chapter are published in the journal Nanoscale as:

Gill, U.; Sutherland, T.; Himbert, S.; Zhu, Y.; Rheinstädter, M. C.; Cranston, E. D.; Moran-Mirabal, J. M. Beyond Buckling: Humidity-Independent Measurement of the Mechanical Properties of Green Nanobiocomposite Films. *Nanoscale* **2017**, *9* (23), 7781–7790.

Urooj Gill did experimental design, data analysis, and manuscript writing with editorial assistance and supervision from Dr. Jose M. Moran-Mirabal and Dr. Emily D. Cranston.

3.1. Abstract

Precise knowledge of the mechanical properties of emerging nanomaterials and nanocomposites is crucial to match their performance with suitable applications. While methods to characterize mechanical properties exist, they are limited by instrument sensitivity and sample requirements. For bio-based nanomaterials this challenge is exacerbated by the extreme dependence of mechanical properties on humidity. This work presents an alternative approach, based on polymer shrinking-induced wrinkling mechanics, to determine the elastic modulus of nanobiocomposite films in a humidity-independent manner. Layer-by-layer (LbL) films containing cellulose nanocrystals (CNCs) and water-soluble polymers were deposited onto pre-stressed polystyrene substrates followed by thermal shrinking, which wrinkled the films to give them characteristic topographies. Three deposition parameters were varied during LbL assembly: (1) polymer type (xyloglucan – XG, or polyethyleneimine – PEI); (2) polymer concentration (0.1 or 1 wt%); and (3) number of deposition cycles, resulting in 10–600 nm thick nanobiocomposite films with tuneable compositions. 2D fast Fourier transform analysis on electron microscopy images of the wrinkled films was used to calculate humidity-independent moduli of 70 ± 2 GPa for CNC-$XG_{0.1}$, 72 ± 2 GPa for CNC-$PEI_{0.1}$, and 32.2 ± 0.8 GPa for CNC-$PEI_{1.0}$ films. Changing the LbL deposition parameters led to structured nano-biocomposites with tunable mechanical properties and topographies, and given the "green" and non-toxic nature of the films, they were found to be suitable cell culture platforms. This structuring method is straightforward and amenable to a wide range of supported thin films,

where applications of these CNC nanobiocomposite films may include smart packaging, cell-based biosensors, extracellular matrix mimics, and tissue engineering substrates.

3.2. Introduction

The unique chemical, electrical and mechanical properties of nanomaterials make them attractive for a diverse range of applications spanning nanomedicine, nanoelectronics and nanomachines. Current and future products incorporating nanomaterials include sensors, energy storage/conversion devices, wearable electronics, drug delivery systems, inks, and water purification systems, among many others.[1–4] The past 30 years have seen immense progress in the production of nanomaterials and devices, and the development of nanocharacterization techniques. However, despite the importance of mechanical performance in many applications, methods to measure nanomechanical properties have failed to keep pace. This work thus presents a structuring method that allows for the humidity-independent determination of the elastic modulus of supported thin film nanocomposites, prepared from plant-derived nanoparticles and polymers that are assembled using a water-based layer-by-layer (LbL) deposition approach.

Current methods to determine the elastic modulus of nanocomposite thin films include nanoindentation, dynamic mechanical thermal analysis, three-point bending flexural tests, and buckling measurements.[5,6] However, these techniques are often limited by their precision, lacking the sensitivity required to detect the mechanical response of individual nanoparticles or ultrathin films. Furthermore, conventional mechanical testing methods, and even some nanomechanical techniques, are only amenable to free-standing

films, but are incapable of handling films with sub-micron thicknesses. In all cases, sample preparation, technique operation and data processing can be highly nanomaterial specific. These problems are exacerbated when it comes to working with thin films that are sensitive to humidity, such as films fabricated from bio-based nanomaterials like crystallites and nanofibers.

Nanocellulose is a family of bio-based materials (*e.g.* cellulose nanocrystals – CNCs, and cellulose nanofibrils – CNFs) that strongly interact with water,[7] which has made it challenging to accurately quantify the mechanical properties of nanocellulose-containing composites.[8–10] Nanocellulose is a "green" and non-toxic[11] nanomaterial extracted from plants, algae, bacteria, and tunicate with a broad range of applications. Favourable properties of nanocellulose include its high chemical, colloidal, and thermal stability (compared to other bio-based materials), large aspect ratio, and impressive mechanical strength resulting from cellulose's ability to form tightly packed crystalline structures.[12]

The elastic modulus of crystalline cellulose has been debated for decades based on X-ray diffraction, inelastic X-ray scattering, atomic force microscopy (AFM), Raman spectroscopy, and modeling techniques – all of which have their own assumptions and limitations. Despite conflicting results, the elastic modulus for crystalline cellulose is taken to be in the 57-220 GPa and 9-50 GPa range in the axial and transverse directions, respectively.[8,13] The mechanical properties of individual CNCs have also been assessed by AFM[14] and Raman spectroscopy,[15] where the axial modulus values ranged from 57-143 GPa.[8] The specific modulus of nanocellulose is thus comparable to materials such as Kevlar or steel[12] and is predicted to greatly reinforce matrix materials according to geometric

percolation models.[16] However, to date these properties have not been fully exploited in nanobiocomposites, partially due to their humidity dependence.

In the present study, we have used an "extreme case" of the SIEBIMM (strain-induced elastic buckling instability for mechanical measurements) method[6,17] to irreversibly structure LbL CNC nanocomposite films, through the extensive compressive stress induced by the shrinkage of an underlying shape-memory polymer. We demonstrate that this structuring approach allows us to quantify the mechanical properties of the films in a humidity-independent manner. Films of CNCs and water-soluble polymers were deposited onto pre-stressed polystyrene (PS) substrates, after which the substrates were heated above their glass transition temperature and shrunken, causing wrinkling of the nanocomposite films. The PS shrinking method has been previously used to create micro- and nanostructured surfaces from metallic, oxide, and carbon nanotube thin films,[18–22] but has not been applied to structure or measure the modulus of nanobiocomposite films. In particular, the humidity independent nature of the modulus measurement strategy and irreversibility of the structures has not been previously shown.

The LbL nanocomposite films used in this study were prepared by dipping the PS substrate in alternating aqueous baths of CNCs and either the hemicellulose xyloglucan (XG) or the cationic polyelectrolyte polyethyleneimine (PEI), where the interactions responsible for layer build-up were van der Waals[23] and electrostatic interactions,[9,24] respectively. CNC-XG films are interesting as mimics for the plant cell wall, where XG is believed to crosslink individual cellulose microfibrils and increase the strength and load-bearing properties of the cell wall,[25] and have also been used as sensors for the detection of

enzymes.[23,26–30] On the other hand, little work has focused on CNC-PEI mixtures and films, which represent model nanobiocomposite systems where the CNCs are strongly incorporated into the polymeric matrix through electrostatic interactions. Previous SIEBIMM measurements on CNC-PEI films have reported elastic moduli of 16, 12, and 3.5 GPa at 30, 42, and 64% relative humidity,[9,10] demonstrating that the films' mechanical properties are highly humidity dependent. The complexity of equilibrating films under controlled humidity for long times and performing the measurements under identical conditions make it prohibitive to extensively test multiple nanobiocomposite formulations, which has led to the approach presented here.

In this work, three parameters were varied during LbL film assembly: polymer type, polymer concentration, and the number of deposition cycles, where the mechanical properties of these films were rapidly and accurately quantified, something that would have been difficult to achieve using the SIEBIMM approach. We have observed marked differences in the mechanical properties of the nanobiocomposite films based on the identity of the polymer used and its relative content within the film. We hypothesize that the differences observed stem from the different driving forces involved in the film assembly and the intrinsic polymer properties. Our results show that the rational use of polymer components can lead to films with tuneable stiffness and can extend the range of mechanical properties and surface topographies attainable with nanocellulose materials. We anticipate that these new nanobiocomposites will find applications in smart packaging, cell-based biosensors, extracellular matrix mimics, and tissue engineering substrates.

3.3. Experimental

3.3.1. Chemicals

Deionized water with a resistivity of 18.2 MΩ cm was used for all experiments (Milli-Q A10 Purification System, Millipore, Etobicoke, Canada). Polyallylamine hydrochloride (PAH, M_w = 120000 – 200000 g/mol) was purchased from Polysciences (Warrington, PA) and prepared in water to a concentration of 0.1 wt%. A 3 wt% cellulose nanocrystal (CNC) suspension was obtained through acid hydrolysis of cotton filter aid (Whatman ashless filter aid, GE Healthcare Canada, Mississauga, Canada). A xyloglucan (XG) solution (0.1 wt%) was a gift from Dr. Laurent Heux (CNRS, Grenoble, France). Polyethyleneimine (PEI, M_w = 750,000 g/mol, 50% (w/v) in water) was purchased from Sigma-Aldrich (Oakville, Canada), and prepared in water to concentrations of 0.1 wt% and 1 wt%.

3.3.2. Biologicals

Murine RAW264.7 cells (ATCC® TIB-71™) were purchased from the American Type Culture Collection (ATCC, Manassas, VA). Dulbecco's Modified Eagle Medium (DMEM, consisting of L-glutamine and high glucose, 10%fetal calf serum Penicillin/Streptomycin), TrypLETM-EDTA, trypan blue, fluorescent dyes 4',6-diamino-2-phenylindole (DAPI) and Phalloidin-AlexaFluor 488, and the LIVE/DEAD® Viability/Cytotoxicity assay kit were purchased from Invitrogen, Life Technologies (Burlington, ON, Canada). Glycine, para-formaldehyde, glutaraldehyde, bovine serum albumin (BSA), fish gelatin, and Triton X-100 were all purchased from Sigma-Aldrich

(Oakville, ON, Canada). Phosphate buffered saline (PBS, 10X) was obtained from BioShop Inc. (Burlington, ON, Canada), and used at 1x concentration for all experiments.

3.3.3. Preparation of Cellulose Nanocrystals (CNCs)

CNCs were produced through the sulfuric acid hydrolysis of cotton, as reported previously.[31] A total of 700 mL sulfuric acid (64 wt%, Sigma Aldrich, Oakville, ON, Canada) was used to hydrolyze 40 g cotton filter aid in a 45 °C water bath for 45 minutes, with constant mechanical stirring. The reaction was quenched by diluting 10-fold in Milli-Q water and decanted. The mixture was repeatedly centrifuged in 10-minute intervals at 5500*g* to remove excess acid. A stable CNC suspension was obtained, where no pellet formed following centrifugation. The suspension was then dialyzed against Milli-Q water for two weeks, until the pH of the external dialysis reservoir stabilized. Following this, a point probe sonicator (Sonifier 450, Branson Ultrasonics, Danbury, CT) was used to sonicate the CNC suspension in an ice water bath for 45 minutes, in three 15-minute intervals. The suspension was filtered through a glass microfiber filter (Whatman grade GF/B, VWR, Chicago, IL), yielding a solution of approximately 1 wt% CNCs. The CNC suspension was concentrated to 3 wt% through evaporation at ambient conditions, and its pH was adjusted from 3.36 to 6.07 using 10 M NaOH (EMD Millipore, Darmstadt, Germany), such that CNCs were used in the sodium-form. Sulfate half-ester content grafted to the CNCs was measured using conductometric titrations,[32] which showed that the sulfur content on the CNCs was 0.43 wt%, corresponding to 0.25 charge groups/nm^2. Dynamic light scattering (DLS) indicated that the average "apparent" size of the CNCs was 92 nm. By AFM, the average CNC dimensions were 197 nm in length and 8 nm in height.

3.3.4. Polystyrene (PS) Substrate Preparation

Pre-stressed PS shrink films (Graphix Shrink Film, Graphix, Maple Heights, OH) were used as substrates, and were first cut into 2 × 2 cm squares with a Robo Pro CE5000-40-CRP cutter (Graphtec America Inc., Irvine, CA). The CB15UB ceramic blade (Graphtec America Inc., Irvine, CA) was used with a force, quality and speed set of 30, 1, and 1, respectively. The square substrates were cleaned under orbital agitation (50 rpm) for 5 minutes each in isopropanol, ethanol, and water baths, consecutively, and dried using a nitrogen stream. Cleaned PS substrates were stored until ready to use.

3.3.5. Nanobiocomposite Film Preparation

Films were prepared on PS substrates using the LbL technique. PS substrates were first cleaned using air plasma at 600 mTorr for 3 minutes (PDC001 Expanded Plasma Cleaner, Harrick Plasma, Ithaca, NY). The clean substrates were then dipped into the following solutions/suspensions for 15 minutes each: a) PAH, b) CNCs (3 wt%), and c) XG or PEI (0.1 wt% or 1 wt%). Following each dipping step, the PS substrates were rinsed in water for 5 minutes then dried using a nitrogen stream. After the initial PAH layer, the substrates were alternated between CNC suspensions and XG or PEI solutions. One bilayer (N = 1) was defined as a single deposition step of CNCs followed by an adsorption step with XG or PEI, and films were denoted CNC-XG or CNC-PEI; thus, integer bilayers had XG or PEI as the outermost layer and half-integer bilayers had CNCs as the top layer. Nanobiocomposite films were prepared from N = 1 to 20 bilayers for CNC-$XG_{0.1}$ films,

and from N = 1 to 20.5 bilayers for CNC-$PEI_{0.1}$ ([PEI] = 0.1 wt%) and CNC-$PEI_{1.0}$ ([PEI] = 1 wt%) films.

3.3.6. Structuring of Nanobiocomposite Films

PS substrates with CNC-polymer films of varying thicknesses were shrunken in an isotemp vacuum oven (Fisher Scientific, Ottawa, ON, Canada) at 135 °C for 15 minutes, on aluminum boats lined with parchment paper.[18] These boats allowed for uniform heat transfer throughout the PS substrates, avoiding any distortion forming in the shrunken substrates.

3.3.7. Atomic Force Microscopy (AFM)

AFM images of structured CNC-$PEI_{1.0}$ films (N = 20 bilayers) were obtained in Alternating Current (AC) mode with a speed of 0.5 Hz, using an Asylum MFP-3D atomic force microscope (Asylum Research an Oxford Instrument Company, Santa Barbara, CA). Rectangular FMR cantilevers (NanoWorld) were used with normal spring constants of 1.2–5.5 N m^{-1} and resonant frequencies of 60–90 kHz.

3.3.8. Variable Angle Spectroscopic Ellipsometry (VASE)

Thickness measurements were obtained for nanobiocomposite films prepared on Si substrates. A M-2000UI™ variable angle spectroscopic ellipsometer (J.A. Woollam Co., Inc., Lincoln, NE) was used, which spanned wavelengths of 250 – 1680 nm and angles from 55 – 75 degrees, in 5 degree increments, to obtain ellipsometric data for the films. The CompleteEASE® Software was used to extract the thickness values of the

nanobiocomposite films. Here, the Cauchy model was used to fit the ellipsometric data with the assumption that transparent films were present on the Si substrates.

3.3.9. X-Ray Diffraction (XRD)

X-ray diffraction data was obtained using the Biological Large Angle Diffraction Experiment (BLADE) in the Laboratory for Membrane and Protein Dynamics at McMaster University. X-ray measurements were conducted at room temperature and ambient relative humidity using a Rigaku SmartLab X-ray diffractometer (Rigaku Corporation), which was equipped with a 9 kW (45 kV, 200 mA) CuKα rotating anode at a wavelength of 1.5418 Å. X-ray measurements were obtained for samples deposited on Si substrates, which consisted of pure CNCs, XG, PEI and samples that consisted of CNC-$XG_{0.1}$ and CNC-$PEI_{1.0}$ films (N = 20 bilayers) and CNC-$PEI_{0.1}$ films (N = 40 bilayers). Both the source and the detector were mounted on movable arms, and the wafers remained horizontal for the duration of the measurements. The wafers were oriented in the X-ray diffractometer such that the $q_{||}$-axis probed the lateral structure parallel to the wafer surface, and the out-of-plane structure, q_z, perpendicular to the substrate. Multi-layer optics were focused to give a high intensity beam parallel to the monochromatic X-ray intensities (up to 10^{10} counts/mm^{2}s), from which a sketch of the resulting scattering geometry was generated. Note that there was no risk of sample damage using this in-house technique, as a result of the large beam size and the relatively low intensity of the X-ray beam itself. A 2D intensity map was obtained from these XRD experiments using MATLAB, which showed the area of the reciprocal space. The corresponding real-space length scales were 2.5 – 60 Å and were determined using the

equation $d = \frac{2\pi}{|Q|}$, where d is the distance between two scatterers and Q is the scattering vector. The intensity maps were integrated over the azimuth and the meridian, and the resulting curves were fitted using a Lorentzian distribution. The diffraction patterns of the pure samples (CNC, XG and PEI) were fitted with multiple-peak profiles. These base profiles were then used to deconvolve the XRD data of the nanobiocomposite films into its individual components based on the relative weight of the profiles. Here, the signal intensity of the components was assumed to be directly correlated to their mass abundance in the nanobiocomposite films. We validated the method used to extract these film compositions by repeating the analysis on a drop-cast film of 50:50 CNC:$PEI_{1.0}$. The X-ray analysis for this film was performed as described above, where measurements were taken at 10% relative humidity due to the hygroscopic nature of the film components.

3.3.10. White Light Interference Microscopy (WLIM)

WLIM measurements were taken using a Zygo NewView 5000 white light interferometer (Zygo Corporation, Middlefield, CT). Data was obtained for nanobiocomposite films formed on PS substrates, before and after shrinking. Five different areas on each substrate were imaged onto a charge coupled device (CCD) camera using a 50× objective with 2× additional optical zoom, resulting in fields of view of 70 × 50 μm, and a camera pixel size of 112 nm. The topographical maps obtained through WLIM were used to calculate the root mean square (RMS) roughness of each of the surveyed areas, from which an average RMS roughness value was calculated. For all images, a fast Fourier transform (FFT) band pass filter was applied to remove noise with cut-off frequencies of

183.35 mm^{-1} and 558.79 mm^{-1}. The MetroPro software (Zygo Corporation, Middlefield, CT) was used for image analysis.

3.3.11. Scanning Electron Microscopy (SEM)

SEM images were obtained for PS substrates with structured nanobiocomposite films using a JEOL JSM-7000S (JEOL USA, Inc., Peabody, MA) scanning electron microscope with an accelerating voltage of 2.5 kV, working distance of 6 mm, and low probe current of 30 μA.

3.3.12. Structure Analysis of Structured Nanobiocomposite Films

The characteristic wrinkle length (ζ) of the structured films was defined as the width of the resulting wrinkles, which is proportional to the persistence length (ξ) described by Groenewold,[33] and, like the persistence length, also shows a linear correlation to the film's thickness. The values for ζ at the different thicknesses and film compositions were calculated from the 2D FFT power spectra of the corresponding SEM images (Figure A-1). SEM images taken at various magnifications were cropped into 900 × 900 pixel images and analyzed individually. Each image was adjusted for its brightness and contrast, after which the Canny threshold method on MATLAB was used to determine the edges of the wrinkled structures, which were rendered as a binary image. A MATLAB program was used to run a 2D FFT of the binary image. The power spectrum and the probability vs. length scale (μm) plot were generated from the binary image. The probability values were normalized to the maximum probability, then averaged for all SEM images and analyzed for each data point. A probability vs. log (length scale) plot was used to identify the values

corresponding to the highest probability, which were averaged to determine the ζ of the structured films.

3.3.13. Elastic Modulus Calculations

To determine the elastic modulus of the nanobiocomposite films, plots of the characteristic wrinkle length (ζ) vs. film thickness (h) were generated. A linear regression to $\xi = a\zeta = 2\pi\eta^{\frac{2}{3}}h$, allowed us to extract the value for the parameter

$$\boldsymbol{\eta} = \frac{\boldsymbol{E_f\left(1-\nu_{PS}^2\right)}}{\boldsymbol{3E_{PS}\left(1-\nu_f^2\right)}} \tag{3.1}$$

where E_f, ν_f are the elastic modulus and Poisson's ratio for the rigid film and E_{PS}, ν_{PS} are the elastic modulus and Poisson's ratio for bulk polystyrene at 135°C (the temperature at which the films were shrunken).[33,34] The scaling factor a was calibrated by using the reported modulus (70 GPa)[35,36] and Poisson's ratio (0.42)[36] for thin gold films deposited by sputtering (for full detail on the calibration, see Supplementary Information). Values of E_{PS} = 1.63 GPa and $\nu_{PS} = 0.36$ were used for the PS substrate at 135°C in the calculations.[37] To obtain the final elastic moduli of the polymer-CNC nanobiocomposite films, a Poisson's ratio of 0.3 was used, which has been reported to match that of the cell wall material (hemicelluloses and cellulose)[38] and is intermediate to that reported for CNCs (0.28) and the polymers used in the formation of the nanobiocomposite films (0.33).[39]

3.3.14. RAW264.7 Cell Culturing

Frozen RAW264.7 cell aliquots were thawed rapidly in a 37°C water bath and suspended in DMEM pre-heated to 37°C. The cells were then centrifuged for 5 minutes at 500*g*. The supernatant was removed and the cell pellet was resuspended in DMEM, which was incubated in a 75 cm^3 tissue culture flask at 37°C and 5% CO_2. When 80% cell confluence was achieved (3-5 days), the cells were subcultured by removing DMEM from the flasks, washing the cells with PBS, and incubating the cells with 10 mL TrypLETM-EDTA at 37°C for 5-15 minutes. The cell suspension was then transferred into 20 mL DMEM and centrifuged for 5 minutes at 500*g*. The supernatant was discarded, and the cell pellet was resuspended in fresh DMEM. A total of 10 µL of the cell suspension was mixed with 10 µL trypan blue, and used to obtain a cell count with a hemacytometer. The cell suspension was then added to unshrunken and shrunken PS substrates consisting of CNC-$PEI_{1.0}$ films prepared from 2 to 10.5 BLs, at concentrations of 10^5 and 10^3 cells per substrate for the LIVE/DEAD assay and cell morphology study, respectively. The cells were incubated on the substrates for 24 hours at 37°C and 5% CO_2.

3.3.15. Cell Viability

A LIVE/DEAD assay was performed as outlined in the standard protocol available from Invitrogen. The number of viable cells was quantified using a SpectraMax i3 Multi-mode plate reader (Molecular Devices, Sunnyvale, CA). The cells were imaged in PBS, using a Nikon Eclipse LV100N POL epifluorescence microscope (Nikon Instruments, Mississauga, ON, Canada), equipped with a CFI TU Plan Fluor EPI 20x physiological

objective. Excitation and emission filters for the dyes Calcein and ethidium homodimer-1 were used. The cells were visualized using a Retiga 2000R cooled CCD camera (QImaging, Surrey, BC, Canada) and images were captured using the NIS-Elements AR software (Nikon Instruments, Mississauga, ON, Canada).

3.3.16. Cell Fixation, Staining, and Imaging Using Fluorescence Microscopy

DMEM media was removed from each substrate, and the substrates were washed with PBS (3x). The substrates were then incubated in 4% p-formaldehyde and 0.1% glutaraldehyde fixation solution in the dark for 15 minutes. The substrates were then washed with PBS (3x) and incubated with 25 mM glycine in PBS for 10 minutes to cap any free aldehyde groups. The glycine solution was removed and the substrates were incubated for 15 minutes in a blocking solution consisting of 0.2% BSA and 0.2% fish gelatin in PBS. The blocking solution was removed and the cells were incubated for 5 minutes in a 600 nM DAPI solution in PBS and washed with PBS (3x). Next, the cells were incubated for 5 minutes in a 0.2% Triton-X 100 solution in PBS, washed once with fresh PBS, and incubated for 20 minutes in 165 nM Phalloidin-AlexaFluor 488 (Invitrogen) in PBS. The staining solution was removed and replaced with fresh PBS. The cells were imaged in PBS using the Nikon Eclipse LV100N POL epifluorescence microscope, equipped with a CFI TU Plan Fluor EPI 60x physiological objective. Excitation and emission filters for the dyes DAPI and AlexaFluor 488 were used. The cells were visualized using a Retiga 2000R cooled CCD camera and images were captured using the NIS-Elements AR software. All steps described in this section were performed at room temperature.

3.3.17. Fractal Analysis

Fluorescence images obtained for RAW264.7 cells seeded onto planar and structured CNC-$PEI_{1.0}$ films were thresholded and converted into binary images using MATLAB. The fractal dimension for the area and perimeter of the binary cell images was calculated using a box-counting algorithm programmed in MATLAB.[40] The program generated plots of log(N) versus $\log(1/s^2)$, where N is the number of boxes fitted within the cell image, and s was the size of the boxes of varying sizes. The slope of the plots was equal to the fractal dimension (D).

3.4. Results and Discussion

3.4.1. Structuring of CNC-Polymer Nanobiocomposite Films

Nanobiocomposite films containing CNCs and a complementary polymer were prepared using the LbL method. The films were deposited onto pre-stressed PS substrates pretreated with a monolayer of poly(allylamine hydrochloride) (PAH), which is known to enhance the adsorption of the first layer of CNCs (Figure 3-1a).[9] The LbL deposition process was entirely water-based, where the films were built to the desired thickness through the alternating adsorption of CNCs and either XG or PEI from dilute aqueous solutions. The prepared CNC-polymer films consisted of full (N) or half-integer bilayers (N+0.5), where either polymer or CNCs (Figure 3-1b) were the topmost layer, respectively. XG and PEI (Figure 3-1c) were chosen as polymers for the LbL build-up of the nanobiocomposite films because they interact strongly with CNCs and have been previously shown to deposit as uniform coatings onto CNC layers.[9,23,26,28–30] Following LbL

film build-up, the PS substrates were heated above their glass transition temperature and shrunken isotropically. This shrinking process generated compressive stress, which turned the smooth CNC-polymer films into rough wrinkled surfaces with tuneable topographies that spanned the nano- to micrometer scale.

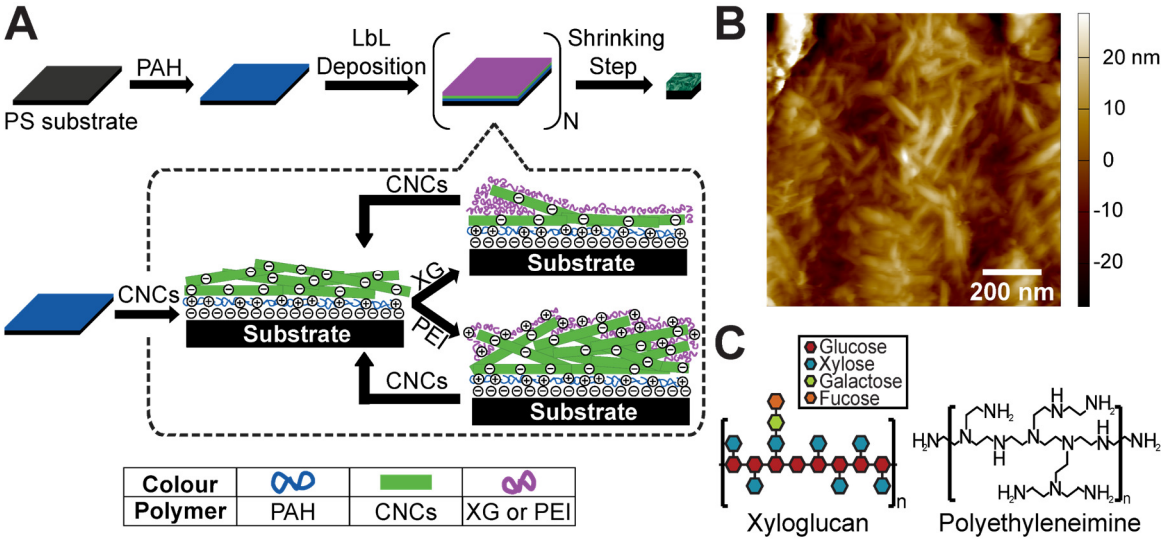

Figure 3-1. Fabrication of LbL nanobiocomposite structured films. A) LbL films were fabricated on pre-stressed PS substrates. PAH was first deposited onto the substrates, followed by the deposition of CNC-polymer bilayers. In the LbL fabrication process, an alternating layer of CNCs and polymer (XG or PEI) were successively adsorbed from solution onto the substrates, forming one bilayer (N = 1). This bilayer deposition process was repeated to form films of varied thicknesses. The CNC-polymer films were then structured by heating the PS substrates, which caused them to shrink biaxially and wrinkle the CNC-polymer films. B) Atomic force microscopy (AFM) height image of a structured CNC-polymer film composed of 20 bilayers (image zoomed into a flat area that allowed AFM tracing). C) Chemical structures of xyloglucan and polyethyleneimine.

In addition to the final film thickness (dependent on N), LbL deposition parameters (type of polymer and polymer concentration) were varied to assess their impact on the morphology and mechanical properties of the CNC-polymer films before and after

structuring. The polymer concentrations investigated were 0.1 wt% for films made with XG and PEI (labeled as CNC-$XG_{0.1}$ and CNC-$PEI_{0.1}$ films) and 1 wt% for PEI (labeled as CNC-$PEI_{1.0}$ films). Scanning electron microscopy (SEM) images of the structured nanobiocomposite films showed that the size of the wrinkles formed through shrinking increased as the number of deposited bilayers increased (Figure 3-2), and were present across the whole film surface (1×1 cm). The increase in structure size suggested that the nanobiocomposite film thickness was proportional to the number of bilayers deposited (confirmed through ellipsometry measurements, *cf.* Figure 3-3).

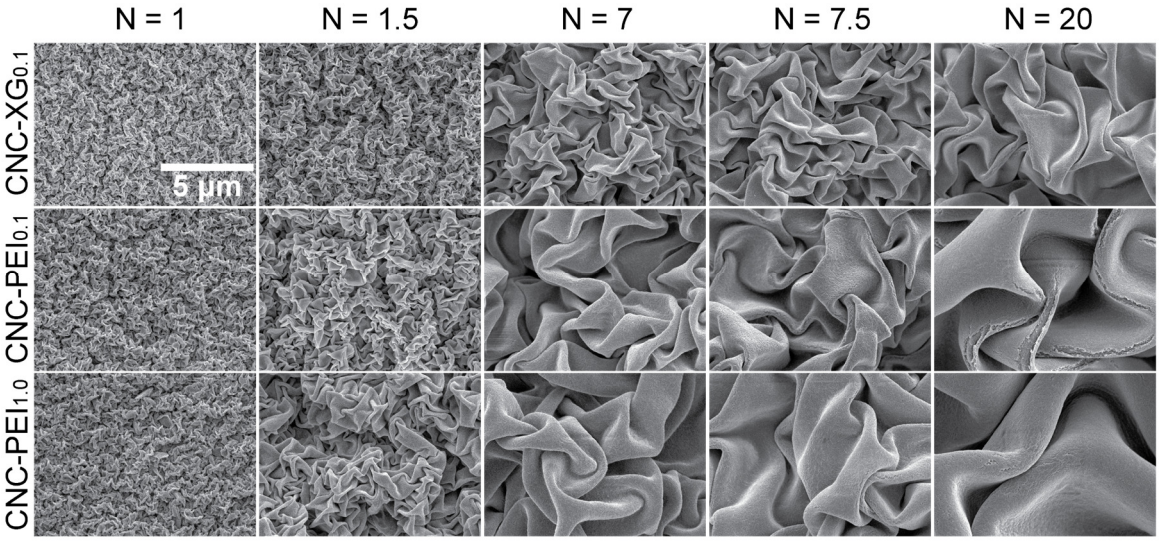

Figure 3-2. SEM images of biaxially wrinkled CNC-polymer films with varying number of deposited bilayers.

It is worth noting that films where the CNCs were the topmost layer (N+0.5 bilayers) formed wrinkled features of comparable size to those formed with the additional polymer layer (N+1 bilayers), indicating that the bulk of the film thickness arises from the

addition of CNC layers. It was also observed that the nanobiocomposite films cracked at a lower number of layers when the topmost layer was made up of CNCs (Figure A-2), which implies that the half bilayer film (N+0.5) has a lower fracture toughness than the full bilayer one (N+1). Film cracking was consistently observed throughout the wrinkled films when they contained more than 20 bilayers (Figures 3-2 and A-3). These observations suggest that most of the film thickness and stiffness arises from the CNC layers, and that the polymer is a filler for the crevices left by the nanocrystals where it acts as a plasticizer; but also, that there is a thickness beyond which the films can no longer accommodate the compressive stress generated, and fracture at the points of maximum strain (wrinkle ridges).

It was also observed that the amount of polymer incorporated played a significant role in the mechanics and structuring of the CNC-polymer films. A comparison between CNC-$PEI_{1.0}$ and CNC-$PEI_{0.1}$ films showed that the films prepared with the lower polymer concentration cracked at lower N, despite being thinner. This is evidence of PEI acting as a plasticizer, where increasing the polymer content in the film increased the film elasticity and effectively reduced the strain present within the films. Despite the cracking observed in thicker films, the structured CNC-polymer films were highly stable, as evidenced by the fact that they retained their integrity and structured morphology even after being lifted-off and transferred from the underlying PS substrate (Figure A-4).

3.4.2. Characterization of CNC-Polymer Nanobiocomposite Films

After establishing the shape-memory polymer shrinking as a reproducible and reliable method for structuring the CNC-polymer films and observing their unique

characteristics, we evaluated their thickness and surface roughness as a function of film composition, polymer concentration, and composition of the outermost layer. Variable angle spectroscopic ellipsometry (VASE) measurements on unstructured films confirmed the linear correlation between N and film thickness (Figure 3-3). However, it was observed that the thickness of the film remained relatively constant between films containing N+0.5 and N+1 bilayers. This confirmed our previous observation that CNCs are the main contributors to the film thickness and agrees with previous reports, where CNCs deposited onto flat surfaces from dilute suspensions resulted in open films with interstices between the nanoparticles that could be filled in and smoothed over by the subsequent addition of a polymer layer.[41,42] Thicker bilayers were obtained with higher polymer concentrations, as CNC-$PEI_{1.0}$ films exhibited thicker bilayers than CNC-$PEI_{0.1}$ films (28 ± 1 *vs.* 19.0 ± 0.5 nm/bilayer), and with PEI as the polymer layer over XG (19.0 ± 0.5 *vs.* 6.5 ± 0.4 nm/bilayer for CNC-$PEI_{0.1}$ and CNC-$XG_{0.1}$ films). The thickness per bilayer indicates that at least one layer of CNCs is adsorbing onto each polymer layer (given that CNCs have cross sections in the 5-10 nm range) and are consistent with previously reported thicknesses, which range from 6 to 39 nm/bilayer.[9,26,43–47]

The difference in bilayer thickness for films prepared from 0.1 wt% aqueous solutions of PEI versus XG can be attributed to the polymer structure and interaction with the CNCs. XG is known to adopt a flat linear conformation when deposited onto an underlying CNC layer,[29] which limits the total amount of polymer adsorbed and, subsequently, limits CNC adsorption. On the other hand, the branched and cationic nature of the deposited PEI allows the polymer chains to extend above the film surface, and

increases its surface charge.[9] Electrostatic interactions cause a larger amount of CNCs to adsorb onto this layer, resulting in a thicker CNC layer and thus a thicker bilayer. The interactions between the polymer and CNC layers, and the ability to tune the thickness of the bilayers and the films can be translated into the fine tuning of the nanobiocomposite film mechanical properties and, ultimately, the size and periodicity of the structures fabricated through compressive stress.

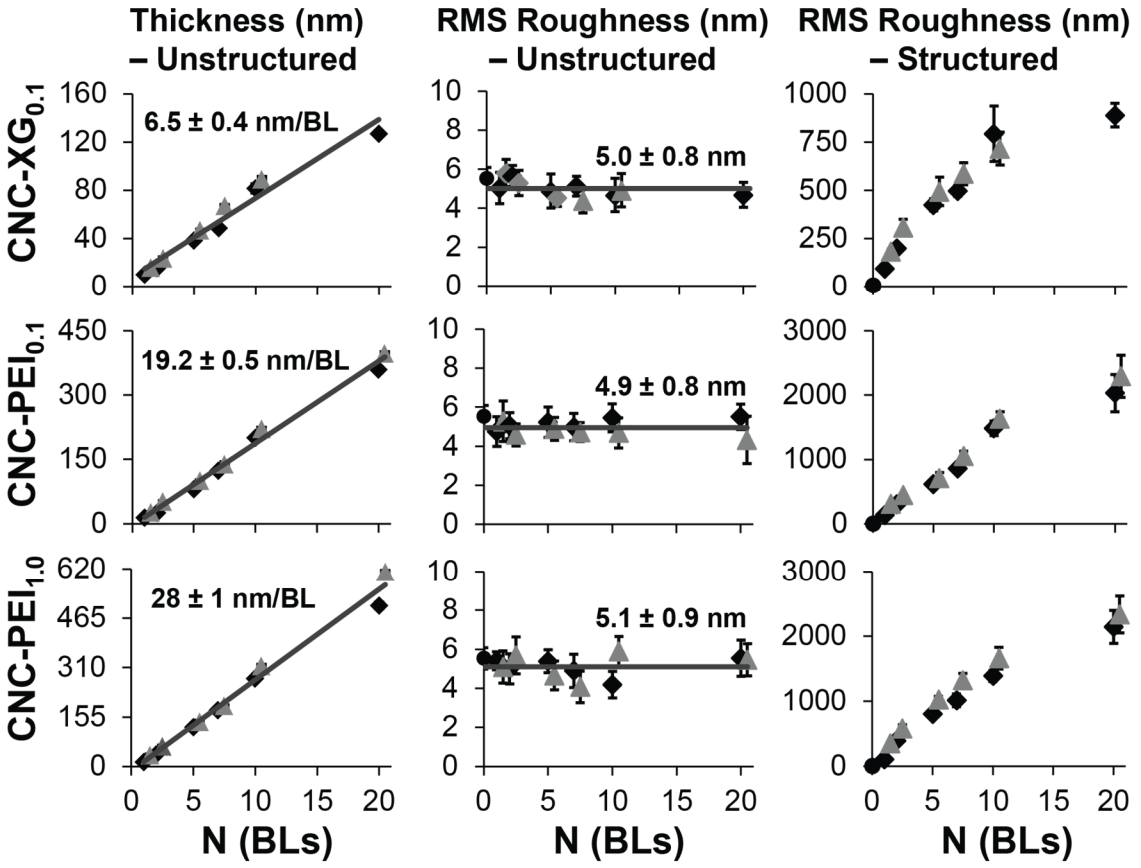

Figure 3-3. Thickness measurements were obtained for all CNC-polymer films using variable angle spectroscopic ellipsometry, where the slopes indicate average thicknesses per bilayer in nanometers, n = 3, all $R^2 \geq 0.96$. White light interferometry was used to characterize the roughness of the nanobiocomposite films prior to structuring (lines and number indicate average roughness) and following structuring, n ≥ 15. For all plots zero (●), full (♦) and half bilayers (▲) are indicated.

White light interferometry microscopy measurements were used to assess the surface roughness of unstructured and structured CNC-polymer films. It was observed that while the film thickness increased with the number of layers present in the unstructured CNC-polymer films, their root mean squared (RMS) surface roughness remained constant at *ca.* 5 nm (Figure 3-3) regardless of the topmost layer, film composition, or film thickness. These roughness values suggest that the topography of the unstructured films was dominated by the widths of the CNCs and are similar to RMS roughness values previously reported for CNC-polymer films.[23,42,48] Following the shrinking of the shape-memory substrate, the topography of the structured CNC-polymer films became substantially rougher, where the roughness increased the thicker the films were (Figure 3-3), with CNC-$PEI_{1.0}$ films exhibiting the largest RMS roughness for any given number of bilayers. In addition, it was observed that in most instances N+0.5 bilayer films had RMS roughness values comparable to those of N+1 bilayer films. This observation agrees with the notion that CNCs are the main contributors to the film thickness (Figure 3-3) and structure size (*cf.* Figure 3-2), and further suggests that the CNC layer is also the key component to determining the rigidity of the films. It was also observed that as N increased, particularly for the CNC-$XG_{0.1}$ films, the roughness plateaued and no increase in roughness was observed for films with additional bilayers (Figure 3-3). The levelling-off of the surface roughness is attributed to the cracking observed in the films (*cf.* Figure 3-2) and has previously been observed in oxide films with thicknesses > 20 nm.[22] Thus, thicker films (larger N) cracked during the shrinking process to relieve strain and did not result in wrinkled features with ever-increasing size.

3.4.3. Mechanical Properties and Composition of CNC-Polymer Nanobiocomposite Films

The elastic modulus of the different nanobiocomposite films was obtained in a humidity-independent way from the morphological data for the structured films and their corresponding thickness measurements. To this end, the periodicity in the topography of the wrinkled surfaces was quantified through 2D fast Fourier transform (2D FFT) analysis of SEM images (Figure A-1). Intensity *vs*. characteristic length plots were generated (Figures 3-4a and A-1) and the peaks with the highest intensity (inset box in Figure 3-4a) were averaged to determine the characteristic wrinkle length (ζ) of the film. This quantity is proportional to the persistence length of the films ($\boldsymbol{\xi = a\zeta}$), which represents the distance at which the wrinkle direction no longer recalls its original direction. Consistent with the film morphology (*cf.* Figure 3-2) and roughness analysis (*cf.* Figure 3-3), we observed that ζ increased linearly with film thickness (Figures 3-4b-d). The elastic modulus was then determined by plotting the thickness (*h*) of the nanobiocomposite film *vs.* its characteristic wrinkle length (ζ). The theory describing these plots[33,34,49] relates $\boldsymbol{\xi}$ (and ζ) to *h* through the relation $\boldsymbol{\xi = 2\pi\eta^{2/3}h}$, where $\boldsymbol{\eta}$ incorporates the elastic modulus and Poisson's ratio of the rigid film ($\boldsymbol{E_f, \nu_f}$) and the underlying substrate ($\boldsymbol{E_{PS}, \nu_{PS}}$). The scaling factor between $\boldsymbol{\xi}$ and ζ was estimated using gold as a reference material. Thin gold films with thicknesses between 20-200 nm were structured, after which the analysis was performed using reported values for the elastic modulus and Poisson's ratio of sputtered gold films and bulk

polystyrene at 135°C. Through this analysis, it was found that the scaling factor $\boldsymbol{\alpha = 5.2 \pm 0.5}$, which was used in all subsequent analysis for the nanobiocomposite films.

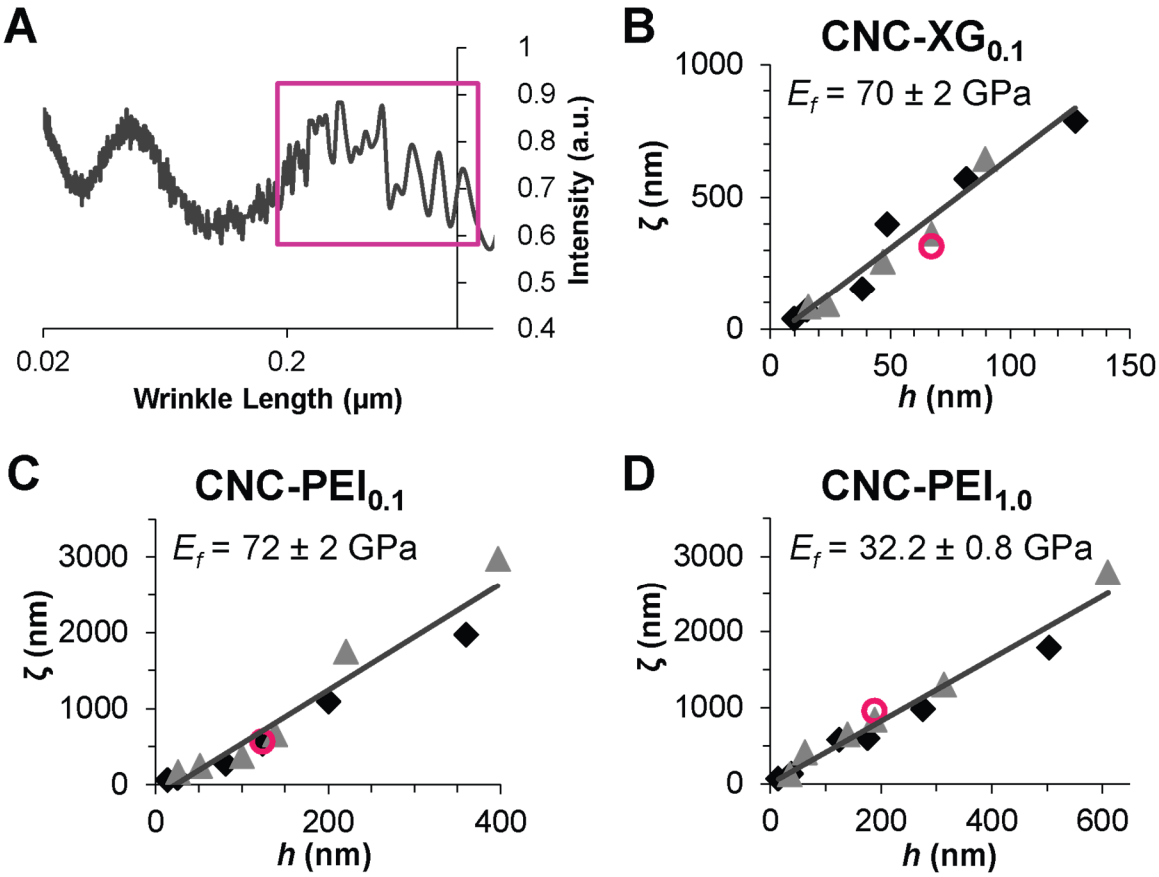

Figure 3-4. Calculation of the elastic modulus from the morphological analysis of the structured nanobiocomposite films. A) Intensity versus characteristic length plots were generated via 2D FFT analysis for the corresponding wrinkled structures. These plots were averaged, where the wrinkle length values at the highest intensities were determined (peaks in boxed area), and averaged to calculate the characteristic length. Plots of characteristic wrinkle length (ζ) vs. film thickness were generated for (B) CNC-$XG_{0.1}$, (C) CNC-$PEI_{0.1}$, and (D) CNC-$PEI_{1.0}$ films, where the slopes were used with Equation 1 to calculate the elastic moduli. Full (♦) and half (▲) bilayers are indicated, $n \geq 3$, all $R^2 > 0.94$-0.97. Open circles indicate films that were hydrated by immersion in water for 30 minutes prior to structuring.

The elastic moduli obtained for the CNC-polymer films through this morphological analysis were 70 ± 2 GPa (CNC-$XG_{0.1}$, Figure 3-4b), 72 ± 2 GPa (CNC-$PEI_{0.1}$, Figure 3-4c), and 32.2 ± 0.8 GPa (CNC-$PEI_{1.0}$, Figure 3-4d). These values are reasonable given that the elastic modulus of a CNC-polymer film is dependent on its relative composition and on the interfacial interactions between the components, and that the reported elastic modulus for CNCs is in the 57-143 GPa range,[12,50] while PEI and XG have elastic moduli of 0.3 GPa[10] and 5.95 GPa,[51] respectively. Furthermore, the calculated values for the elastic modulus are in line with those previously reported for similar CNC-PEI LbL films, where the modulus was calculated as a function of relative humidity through the traditional SIEBIMM method.[9] We propose that our nanocomposites possess a larger modulus than those reported because most of the water entrapped in the films was removed during the shrinking step. To support this, we obtained identical morphology (elastic modulus) for films that were structured from a dry state and films that were fully hydrated (immersed in water for 30 minutes) prior to structuring (Figures 3-4b-d, open circles). This shows that our structuring method is unaffected by the degree of hydration in the films and yields a value for the modulus that depends only on the intrinsic film composition.

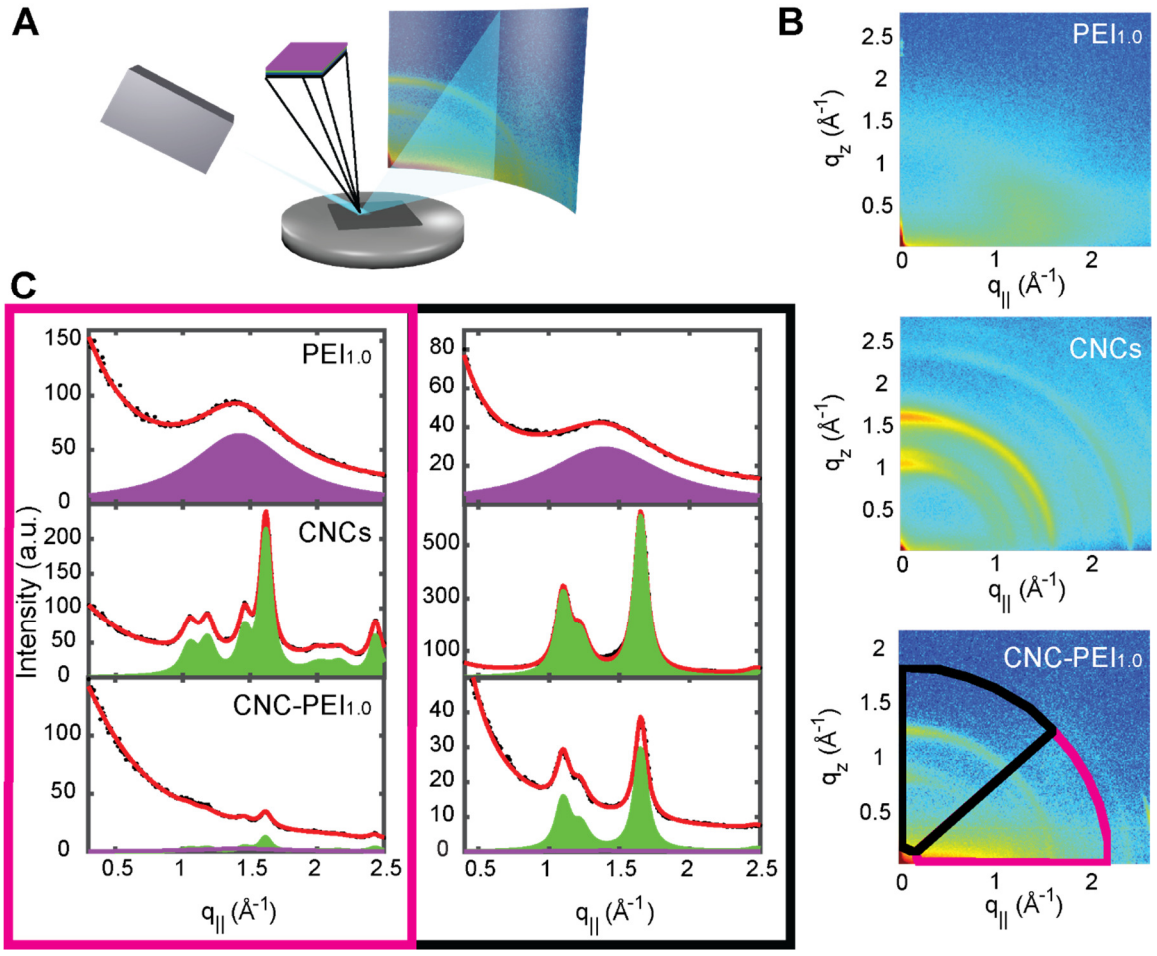

Figure 3-5. X-ray diffraction measurements were used to determine the relative film compositions. A) Schematic for the XRD set-up. B) 2D X-ray plots in the xy plane ($q_{||}$) and xz plane (q_z) for pure polymer samples $PEI_{1.0}$ and CNCs, and a composite CNC-$PEI_{1.0}$ film (N = 20 bilayers). C) Intensity data extracted from the 2D X-ray plot for the CNC-$PEI_{1.0}$ film was analyzed in two sections (black and pink outlines), and fitted using the X-ray profile obtained from the pure polymer samples.

It was interesting to note that significant differences in the mechanical properties of the nanobiocomposite films could be induced by simple changes in the film fabrication method, such as the type of polymer or polymer concentration used. This was attributed to the resulting film thickness (*cf.* Figure 3-3) and to the film's relative composition. The

composition of the CNC-polymer films was determined using X-ray diffraction (XRD), where the scattering perpendicular (q_z) and parallel to the substrate surface ($q_{||}$) yielded characteristic 2-dimensional diffraction intensity patterns (Figures 3-5a-b and A-5 – A-7). To extract the relative composition of the CNC-polymer nanocomposite films, base scattering functions were generated from pure CNC and pure polymer samples deposited through drop-casting. Then, a weighted sum of these functions was used to fit the scattering intensities of the films (Figures 3-5c, A-5 and A-6), where the relative weight of the function corresponded to the proportional mass of each component within the CNC-polymer film. The XRD methodology to calculate the nanobiocomposite film composition was validated using films prepared by drop-casting, where the solution contained CNC:$PEI_{1.0}$ at 50:50 composition by mass (Figure A-7), and the calculated composition was 45:55.

The relative film compositions obtained through XRD analysis were 72:28 (CNC-$XG_{0.1}$), 82:18 (CNC-$PEI_{0.1}$), and 77:23 (CNC-$PEI_{1.0}$) CNC:polymer. In films fabricated with stock polymer solutions of the same weight percentage (0.1 wt%), films with PEI had a higher proportion of CNCs to polymer compared to XG. This compositional analysis matches the thicker bilayers and similar film stiffness observed for CNC-$PEI_{0.1}$ films over CNC-$XG_{0.1}$ films. Similarly, nanobiocomposite films fabricated from lower concentration PEI solutions (0.1 *vs.* 1 wt%) presented a higher CNC mass fraction, which correlates with the higher elastic modulus but not with thicker bilayers. Based on the observations for PEI-containing films, it can be concluded that the higher film stiffness was a result of the film proportion constituted by CNCs, and that this fraction decreased when more polymer was

available to bind to the CNC layers. However, this could not be generalized for all nanobiocomposite films, as CNC-$XG_{0.1}$ films consisted of a lower proportion of CNCs to polymer but were significantly stiffer than CNC-$PEI_{1.0}$ films. The increased film modulus likely stems from the higher elastic modulus of XG (which could be structured as a polymer-only film, Figure A-8a), and its ability to crosslink individual layers of CNCs to form a stronger nanobiocomposite network with an increased stiffness, which would be akin to its role in crosslinking cellulose microfibrils in plant cell walls.[28,51–53]

From all the experiments combined, it is evident that CNCs are the key component that define the mechanical properties of the nanocomposite films, since they make up most of the film, contribute the majority of each bilayer thickness (*cf.* Figure 3-3), provide the bulk of the rigidity (*cf.* Figure 3-4), and thus are mainly responsible for the structuring of the thin film during compression. Yet the nature of the polymer and its interactions with cellulose are also important, since this strongly impacts the film, its rigidity, and ultimately its ability to buckle without fracturing, where CNC-only films readily cracked under compressive stress (Figure A-8b).

3.4.4. Cell Viability and Morphology on CNC-Polymer Nanobiocomposite Films

As a proof-of-concept, we cultured murine macrophage cell line RAW264.7 cells (24 hours, at 37°C and 5% CO_2) on structured CNC-polymer nanobiocomposite films, to assess their suitability as platforms for the study of cell adhesion, proliferation, and morphology. Through a fluorescence viability/cytotoxicity assay, we observed that cells remained viable on the biocomposite films regardless of film topography, film thickness,

or topmost layer (Figure 3-6a), as indicated by the presence of green cells (calcein staining = live) and the lack of red ones (ethidium homodimer-1 staining = dead). The viability of the cells on the unstructured and structured nanobiocomposite surfaces was not statistically different from those on PS controls, indicating that the CNC-polymer films were not cytotoxic (Figure A-9a). While cell viability remained the same across all surfaces, it was interesting to note that a higher number of cells adhered to structured nanobiocomposite surfaces compared to untreated PS and unstructured nanobiocomposite surfaces (Figures A-9b and c). This may be due to differences in the polarity of these surfaces, where the nanobiocomposite films were hydrophilic while the PS surfaces were hydrophobic. RAW264.7 cells preferentially adhered to the structured nanocomposite surfaces, since they were more hydrophilic than their unstructured counterparts due to the increased surface area of the wrinkled features. And so, differences in cell adhesion were a result of changes in the polarity of these surfaces, where more cells adhered to the highly hydrophilic surfaces (wrinkled films) compared to the less hydrophilic surfaces (unstructured films and untreated PS surfaces). Knowing that these structured films were non-cytotoxic and had good cell adhesion, we next wanted to assess how cell morphology was affected by the nanobiocomposite surfaces.

To visually observe changes in cell morphology, we stained RAW264.7 cells with AlexaFluor 488-phalloidin (actin filaments) and 4',6-diamino-2-phenylindole (DAPI, nucleus), and imaged the cells using fluorescence microscopy. Qualitatively, we observed that cells cultured on structured films with large RMS roughness values produced less cytoplasmic protrusions (filopodia) than those cultured on their unstructured counterparts

(Figure 3-6b). To quantify these changes in cell morphology, the fractal dimension of the cell area and perimeter were determined using a box-counting method, as previously reported.[22,40] In such analysis, a higher area fractal dimension indicates that cells are elongated, while a higher perimeter fractal dimension indicates higher complexity in the cell boundary. No significant differences were observed in the fractal dimension obtained from the area of the cells cultured on the biocomposite films regardless of film topography, thickness, or topmost layer (Figure A-10a). On the other hand, the fractal dimension calculated from the perimeter showed that the cell boundaries lost their complexity when the cells were cultured on structured films with increasing RMS roughness values (Figure A-10b). This implies that RAW264.7 cells extended less protrusions on larger wrinkled surfaces.

Our results indicate that these structured CNC-polymer nanobiocomposite surfaces were non-cytotoxic, showed good cell adhesion, and were able to induced changes in cell morphology. The behavior of different types of cells (*e.g.*, fibroblasts, macrophages, stem cells) have been modified using different polymer-based surfaces that had unique topographies such as fibers,[54,55] grating arrays,[56] grooves (or uniaxial features),[57–59] and biaxial wrinkles.[22,59] These surfaces induced changes in the morphology and biochemical response of cells where, for instance, cell alignment and function were altered with changes in surface topography. And so, our observations, together with those seen in the literature, suggest that these structured CNC-polymer surfaces could be used as tissue engineering platforms to alter the response of cells through physical, as well as, biochemical cues.

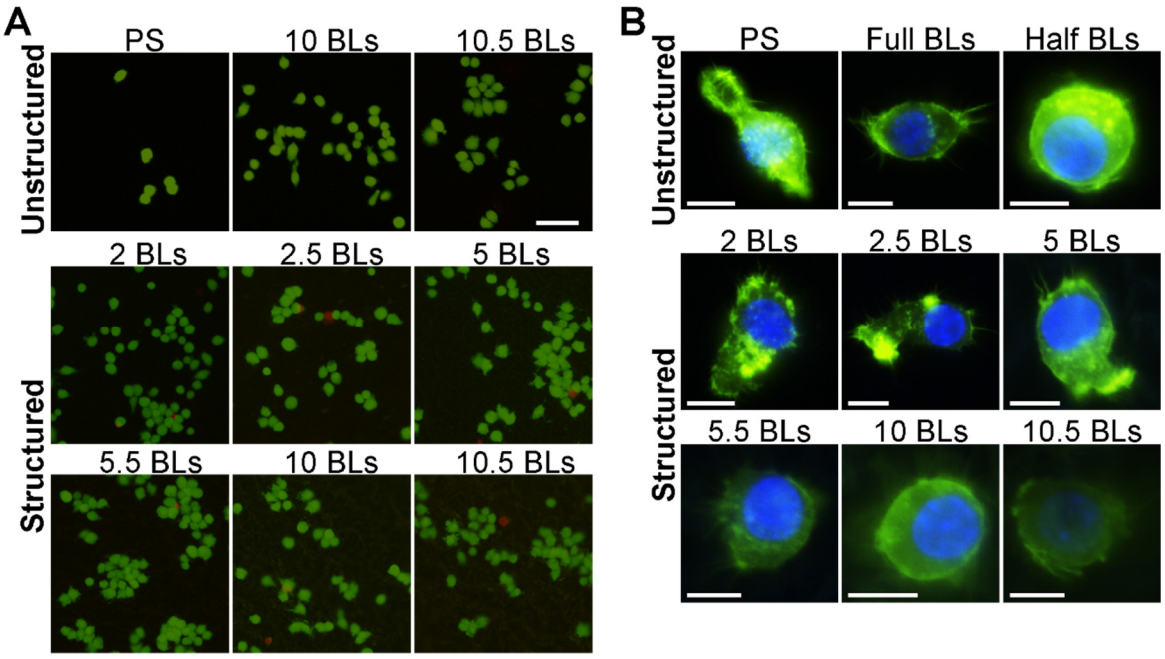

Figure 3-6. Fluorescence images of RAW264.7 cells seeded onto unstructured and structured CNC-$PEI_{1.0}$ surfaces that were prepared at various bilayers (BLs). A) The LIVE/DEAD cytotoxicity assay indicates living cells stained by calcein (green) and dead cells stained by ethidium homodimer-1 (red); scale bar = 50 µm. B) Epifluorescence images of individual cells were obtained by staining the cells with 4',6-diamino-2-phenylindole (DAPI) (blue) and AlexaFluor 488-phalloidin (green) for their nuclei and actin filaments, respectively; scale bars = 10 µm.

3.5. Conclusions

In this work, we have introduced a shape-memory polymer shrinking approach as a humidity-independent way to quantify the mechanical properties of CNC-polymer nanobiocomposite films, and have obtained elastic modulus values that depend solely on nanobiocomposite film composition. To our knowledge, this is the first implementation of this structuring approach on nanobiocomposite thin films, where we have shown that the size, morphology, topography, and elastic modulus of the structured CNC-polymer films can easily be tuned through simple changes in the LbL deposition parameters (*i.e.,* type of

polymer used, polymer concentration, and the number of deposited bilayers). The resulting structured biocomposites are found to be stable, irreversible, and reproducible, making them viable candidates for applications as sensors, in packaging, or as tissue engineering platforms. The elastic moduli calculated from the nanobiocomposite films show that the polymer identity and concentration during the film assembly process have a strong influence on its mechanical properties. The linear polymer xyloglucan can provide higher crosslinking interactions that result in films with high mechanical stiffness at lower thicknesses and CNC loadings, compared to films assembled from a branched polycationic polymer. The technique presented here can be applied to evaluate the mechanical properties of a wide range of materials deposited through sputtering, chemical vapour deposition and evaporation, as well as through solvent- and aqueous-based deposition processes, and is particularly well suited for materials where humidity can have a large impact on the measured mechanical properties. Finally, as proof-of-concept the structured nanobiocomposite films can be employed as cell culture substrates. It is observed that the structured CNC-polymer films do not disrupt cell viability regardless of film topography, thickness, or outermost layer. Furthermore, these structured films adhere to cells more strongly than their unstructured counterparts, where structured topographies at the nanoscale are also shown to induce the enhanced formation of filopodia. In addition to applications in packaging and coating development, the non-toxic, cell adhering nature of these structured CNC-polymer nanobiocomposites opens up potential applications in areas involving cell-based biosensors, extracellular matrix mimics, and tissue engineering.

3.6. Acknowledgements

We thank S Saem for help with scanning electron microscopy, E Niinivaara for help with atomic force microscopy, and JP Boyle for help with cell work. We also thank P Mascher and J Wojcik for access to VASE instrumentation, training on measurements and analysis, DME Bowdish for access to RAW264.7 cells and cell culturing facilities, and T Hoare for access to viability/cytotoxicity assays. UG is the recipient of an Ontario Graduate Scholarship, and JMM and EDC are recipients of Early Researcher Awards from the Ontario Ministry of Research and Innovation. This research was supported by funding through the Natural Sciences and Engineering Research Council and made use of instrumentation from the McMaster Manufacturing Research Institute, Canadian Centre for Electron Microscopy, Brockhouse Institute for Materials Research, Biointerfaces Institute, and the Centre for Emerging Device Technology.

3.7. References

(1) Rogers, B.; Pennathur, S.; Adams, J. *Nanotechnology: Understanding Small Systems*, 2nd Ed.; CRC Press: Boca Raton, FL, 2011.

(2) Cao, G.; Wang, Y. *Nanostructures and Nanomaterials: Synthesis, Properties and Applications*, 2nd Ed.; World Scientific: Singapore, 2011.

(3) Xu, X.; Heng, L.; Zhao, X.; Ma, J.; Lin, L.; Jiang, L. Multiscale Bio-Inspired Honeycomb Structure Material with High Mechanical Strength and Low Density. *J. Mater. Chem.* **2012**, *22*, 10883–10888.

(4) Heng, L.; Guo, X.; Guo, T.; Wang, B.; Jiang, L. Strengthening of Polymer Ordered Porous Materials Based on a Layered Nanocomposite Internal Structure. *Nanoscale* **2016**, *8*, 13507–13512.

(5) *Front Matter, in Polymer Composites: Volume 2*; Thomas, S., Joseph, K., Malhotra, S. K., Goda, K., Sreekala, M. S., Eds.; Wiley-VCH Verlag GmbH & Co. KGaA: Weinheim, Germany, 2013.

(6) Stafford, C. M.; Harrison, C.; Beers, K. L.; Karim, A.; Amis, E. J.; VanLandingham, M. R.; Kim, H.-C.; Volksen, W.; Miller, R. D.; Simonyi, E. E. A Buckling-Based Metrology for Measuring the Elastic Moduli of Polymeric Thin Films. *Nat. Mater.* **2004**, *3* (8), 545–550.

(7) Aulin, C.; Ahola, S.; Josefsson, P.; Nishino, T.; Hirose, Y.; Österberg, M.; Wågberg, L. Nanoscale Cellulose Films with Different Crystallinities and Mesostructures—Their Surface Properties and Interaction with Water. *Langmuir* **2009**, *25* (13), 7675–7685.

(8) Moon, R. J.; Martini, A.; Nairn, J.; Simonsen, J.; Youngblood, J. Cellulose Nanomaterials Review: Structure, Properties and Nanocomposites. *Chem. Soc. Rev.* **2011**, *40*, 3941–3994.

(9) Kan, K. H. M.; Cranston, E. D. Mechanical Testing of Thin Film Nanocellulose Composites Using Buckling Mechanics. *TAPPI J.* **2013**, *12* (4), 9–17.

(10) Cranston, E. D.; Eita, M.; Johansson, E.; Netrval, J.; Salajková, M.; Arwin, H.; Wågberg, L. Determination of Young's Modulus for Nanofibrillated Cellulose Multilayer Thin Films Using Buckling Mechanics. *Biomacromolecules* **2011**, *12*, 961–969.

(11) Roman, M. Toxicity of Cellulose Nanocrystals: A Review. *Ind. Biotechnol.* **2015**, *11* (1), 25–33.

(12) Habibi, Y.; Lucia, L. A.; Rojas, O. J. Cellulose Nanocrystals: Chemistry, Self-Assembly, and Applications. *Chem. Rev.* **2010**, *110* (6), 3479–3500.

(13) Eichhorn, S. J.; Dufresne, A.; Aranguren, M.; Marcovich, N. E.; Capadona, J. R.; Rowan, S. J.; Weder, C.; Thielemans, W.; Roman, M.; Renneckar, S.; Gindl, W.; Veigel, S.; Keckes, J.; Yano, H.; Abe, K.; Nogi, M.; Nakagaito, A. N.; Mangalam, A.; Simonsen, J.; Benight, A. S.; Bismarck, A.; Berglund, L. A.; Peijs, T. Review: Current International Research into Cellulose Nanofibres and Nanocomposites. *J. Mater. Sci.* **2010**, *45* (1), 1–33.

(14) Lahiji, R. R.; Xu, X.; Reifenberger, R.; Raman, A.; Rudie, A.; Moon, R. J. Atomic Force Microscopy Characterization of Cellulose Nanocrystals. *Langmuir* **2010**, *26* (6), 4480–4488.

(15) Šturcová, A.; Davies, G. R.; Eichhorn, S. J. Elastic Modulus and Stress-Transfer Properties of Tunicate Cellulose Whiskers. *Biomacromolecules* **2005**, *6* (2), 1055–1061.

(16) Cao, Y.; Zavattieri, P.; Youngblood, J.; Moon, R.; Weiss, J. The Relationship between Cellulose Nanocrystal Dispersion and Strength. *Constr. Build. Mater.* **2016**, *119*, 71–79.

(17) Stafford, C. M.; Guo, S.; Harrison, C.; Chiang, M. Y. M. Combinatorial and High-Throughput Measurements of the Modulus of Thin Polymer Films. *Rev. Sci. Instrum.* **2005**, *76* (6), 62207.

(18) Gabardo, C. M.; Zhu, Y.; Soleymani, L.; Moran-Mirabal, J. M. Bench-Top Fabrication of Hierarchically Structured High-Surface-Area Electrodes. *Adv. Funct. Mater.* **2013**, *23* (24), 3030–3039.

(19) Lin, S.; Lee, E. K.; Nguyen, N.; Khine, M. Thermally-Induced Miniaturization for Micro- and Nanofabrication: Progress and Updates. *Lab Chip* **2014**, *14*, 3475–3488.

(20) Sonney, S.; Shek, N.; Moran-Mirabal, J. M. Rapid Bench-Top Fabrication of Poly(dimethylsiloxane)/polystyrene Microfluidic Devices Incorporating High-Surface-Area Sensing Electrodes. *Biomicrofluidics* **2015**, *9* (2), 26501.

(21) Park, S.-J.; Kim, J.; Chu, M.; Khine, M. Highly Flexible Wrinkled Carbon Nanotube Thin Film Strain Sensor to Monitor Human Movement. *Adv. Mater. Technol.* **2016**, *1* (5), 1600053.

(22) Zhu, Y.; Boyle, J. P.; Bonin, K.; Chowdhury, T.; Moran-Mirabal, J. M. Micro/nanostructured SiO2 and TiO2 Films Fabricated through Polymer Shrinking as Tunable Topography Substrates for Cell Studies. *Integr. Biol.* Submitted.

(23) Jean, B.; Heux, L.; Dubreuil, F.; Chambat, G.; Cousin, F. Non-Electrostatic Building of Biomimetic Cellulose-Xyloglucan Multilayers. *Langmuir* **2009**, *25* (7), 3920–3923.

(24) Aulin, C.; Varga, I.; Claesson, P. M.; Wågberg, L.; Lindström, T. Buildup of Polyelectrolyte Multilayers of Polyethyleneimine and Microfibrillated Cellulose Studied by in Situ Dual-Polarization Interferometry and Quartz Crystal Microbalance with Dissipation. *Langmuir* **2008**, *24* (6), 2509–2518.

(25) Carpita, N. C.; Gibeaut, D. M. Structural Models of Primary Cell Walls in Flowering Plants: Consistency of Molecular Structure with the Physical Properties of the Walls during Growth. *Plant J.* **1993**, *3* (1), 1–30.

(26) Cerclier, C.; Guyomard-Lack, A.; Moreau, C.; Cousin, F.; Beury, N.; Bonnin, E.; Jean, B.; Cathala, B. Coloured Semi-Reflective Thin Films for Biomass-Hydrolyzing Enzyme Detection. *Adv. Mater.* **2011**, *23*, 3791–3795.

(27) Guyomard-Lack, A.; Cerclier, C.; Beury, N.; Jean, B.; Cousin, F.; Moreau, C.; Cathala, B. Nano-Structured Cellulose Nanocrystals-Xyloglucan Multilayered Films for the Detection of Cellulase Activity. *Eur. Phys. J. Spec. Top.* **2012**, *213*, 291–294.

(28) Cerclier, C.; Cousin, F.; Bizot, H.; Moreau, C.; Cathala, B. Elaboration of Spin-Coated Cellulose-Xyloglucan Multilayered Thin Films. *Langmuir* **2010**, *26* (22),

17248–17255.

(29) Villares, A.; Moreau, C.; Dammak, A.; Capron, I.; Cathala, B. Kinetic Aspects of the Adsorption of Xyloglucan onto Cellulose Nanocrystals. *Soft Matter* **2015**, *11*, 6472–6481.

(30) Dammak, A.; Moreau, C.; Azzam, F.; Jean, B.; Cousin, F.; Cathala, B. Influence of Cellulose Nanocrystals Concentration and Ionic Strength on the Elaboration of Cellulose Nanocrystals–Xyloglucan Multilayered Thin Films. *J. Colloid Interface Sci.* **2015**, *460*, 214–220.

(31) Revol, J.-F.; Bradford, H.; Giasson, J.; Marchessault, R. H.; Gray, D. G. Helicoidal Self-Ordering of Cellulose Microfibrils in Aqueous Suspension. *Int. J. Biol. Macromol.* **1992**, *14*, 170–172.

(32) Abitbol, T.; Kloser, E.; Gray, D. G. Estimation of the Surface Sulfur Content of Cellulose Nanocrystals Prepared by Sulfuric Acid Hydrolysis. *Cellulose* **2013**, *20*, 785–794.

(33) Groenewold, J. Wrinkling of Plates Coupled with Soft Elastic Media. *Physica A* **2001**, *298*, 32–45.

(34) Greco, F.; Bellacicca, A.; Gemmi, M.; Cappello, V.; Mattoli, V.; Milani, P. Conducting Shrinkable Nanocomposite Based on Au-Nanoparticle Implanted Plastic Sheet: Tunable Thermally Induced Surface Wrinkling. *ACS Appl. Mater. Interfaces* **2015**, *7* (13), 7060–7065.

(35) Salvadori, M. C.; Brown, I. G.; Vaz, A. R.; Melo, L. L.; Cattani, M. Measurement of the Elastic Modulus of Nanostructured Gold and Platinum Thin Films. *Phys. Rev. B* **2003**, *67* (15), 153404.

(36) Hodge, T. C.; Bidstrup-allen, S. A.; Kohl, P. A. Stresses in Thin Film Metallization. *IEEE Trans. Components, Packag. Manuf. Technol. Part A* **1997**, *20* (2), 241–250.

(37) Mott, P. H.; Dorgan, J. R.; Roland, C. M. The Bulk Modulus and Poisson's Ratio of "incompressible" Materials. *J. Sound Vib.* **2008**, *312*, 572–575.

(38) Chanliaud, E.; Burrows, K. M.; Jeronimidis, G.; Gidley, M. J. Mechanical Properties of Primary Plant Cell Wall Analogues. *Planta* **2002**, *215*, 989–996.

(39) Shir Mohammadi, M.; Hammerquist, C.; Simonsen, J.; Nairn, J. A. The Fracture Toughness of Polymer Cellulose Nanocomposites Using the Essential Work of Fracture Method. *J. Mater. Sci.* **2016**, *51* (19), 8916–8927.

(40) Moran-Mirabal, J. M.; Aubrecht, D. M.; Craighead, H. G. Phase Separation and Fractal Domain Formation in Phospholipid/diacetylene-Supported Lipid Bilayers. *Langmuir* **2007**, *23* (21), 10661–10671.

(41) Kontturi, E.; Johansson, L.-S.; Kontturi, K. S.; Ahonen, P.; Thüne, P. C.; Laine, J. Cellulose Nanocrystal Submonolayers by Spin Coating. *Langmuir* **2007**, *23* (19), 9674–9680.

(42) Cranston, E. D.; Gray, D. G. Morphological and Optical Characterization of Polyelectrolyte Multilayers Incorporating Nanocrystalline Cellulose. *Biomacromolecules* **2006**, *7* (9), 2522–2530.

(43) Sui, L.; Huang, L.; Podsiadlo, P.; Kotov, N. A.; Kieffer, J. Brillouin Light Scattering Investigation of the Mechanical Properties of Layer-by-Layer Assembled Cellulose Nanocrystal Films. *Macromolecules* **2010**, *43* (22), 9541–9548.

(44) Cranston, E. D.; Gray, D. G. Formation of Cellulose-Based Electrostatic Layer-by-Layer Films in a Magnetic Field. *Sci. Technol. Adv. Mater.* **2006**, *7* (4), 319–321.

(45) Cranston, E. D.; Gray, D. G.; Rutland, M. W. Direct Surface Force Measurements of Polyelectrolyte Multilayer Films Containing Nanocrystalline Cellulose. *Langmuir* **2010**, *26* (22), 17190–17197.

(46) Podsiadlo, P.; Choi, S.-Y.; Shim, B.; Lee, J.; Cuddihy, M.; Kotov, N. A. Molecularly Engineered Nanocomposites: Layer-by-Layer Assembly of Cellulose Nanocrystals. *Biomacromolecules* **2005**, *6* (6), 2914–2918.

(47) Dammak, A.; Moreau, C.; Beury, N.; Schwikal, K.; Winter, H. T.; Bonnin, E.; Saake, B.; Cathala, B. Elaboration of Multilayered Thin Films Based on Cellulose Nanocrystals and Cationic Xylans: Application to Xylanase Activity Detection. *Holzforschung* **2013**, *67* (5), 579–586.

(48) Edgar, C. D.; Gray, D. G. Smooth Model Cellulose I Surfaces from Nanocrystal Suspensions. *Cellulose* **2003**, *10*, 299–306.

(49) Fu, C.-C.; Grimes, A.; Long, M.; Ferri, C. G. L.; Rich, B. D.; Ghosh, S.; Ghosh, S.; Lee, L. P.; Gopinathan, A.; Khine, M. Tunable Nanowrinkles on Shape Memory Polymer Sheets. *Adv. Mater.* **2009**, *21* (44), 4472–4476.

(50) Mariano, M.; El Kissi, N.; Dufresne, A. Cellulose Nanocrystals and Related Nanocomposites: Review of Some Properties and Challenges. *J. Polym. Sci., Part B Polym. Phys.* **2014**, *52*, 791–806.

(51) Kochumalayil, J.; Sehaqui, H.; Zhou, Q.; Berglund, L. A. Tamarind Seed Xyloglucan – a Thermostable High-Performance Biopolymer from Non-Food Feedstock. *J. Mater. Chem.* **2010**, *20*, 4321–4327.

(52) Kochumalayil, J. J.; Berglund, L. A. Water-Soluble Hemicelluloses for High Humidity Applications – Enzymatic Modification of Xyloglucan for Mechanical and Oxygen Barrier Properties. *Green Chem.* **2014**, *16* (4), 1904–1910.

(53) Hayashi, T.; Kaida, R. Functions of Xyloglucan in Plant Cells. *Mol. Plant* **2011**, *4* (1), 17–24.

(54) Han, J.; Wu, Q.; Xia, Y.; Wagner, M. B.; Xu, C. Cell Alignment Induced by Anisotropic Electrospun Fibrous Scaffolds Alone Has Limited Effect on Cardiomyocyte Maturation. *Stem Cell Res.* **2016**, *16* (3), 740–750.

(55) Tseng, L. F.; Mather, P. T.; Henderson, J. H. Shape-Memory-Actuated Change in Scaffold Fiber Alignment Directs Stem Cell Morphology. *Acta Biomater.* **2013**, *9* (11), 8790–8801.

(56) Pholpabu, P.; Kustra, S.; Wu, H.; Balasubramanian, A.; Bettinger, C. J. Lithography-Free Fabrication of Reconfigurable Substrate Topography for Contact Guidance. *Biomaterials* **2015**, *39*, 164–172.

(57) Yang, P.; Baker, R. M.; Henderson, J. H.; Mather, P. T. In Vitro Wrinkle Formation via Shape Memory Dynamically Aligns Adherent Cells. *Soft Matter* **2013**, *9* (18), 4705–4714.

(58) Chen, A.; Lieu, D. K.; Freschauf, L.; Lew, V.; Sharma, H.; Wang, J.; Nguyen, D.; Karakikes, I.; Hajjar, R. J.; Gopinathan, A.; Botvinick, E.; Fowlkes, C. C.; Li, R. A.; Khine, M. Shrink-Film Configurable Multiscale Wrinkles for Functional Alignment of Human Embryonic Stem Cells and Their Cardiac Derivatives. *Adv. Mater.* **2011**, *23* (48), 5785–5791.

(59) Wang, T.; Luu, T. U.; Chen, A.; Khine, M.; Liu, W. F. Topographical Modulation of Macrophage Phenotype by Shrink-Film Multi-Scale Wrinkles. *Biomater. Sci.* **2016**, 0–4.

Chapter 4 – Mechanical Properties of All-Cellulose Nanocrystal Thin Films as a Function of Nanoparticle Orientation

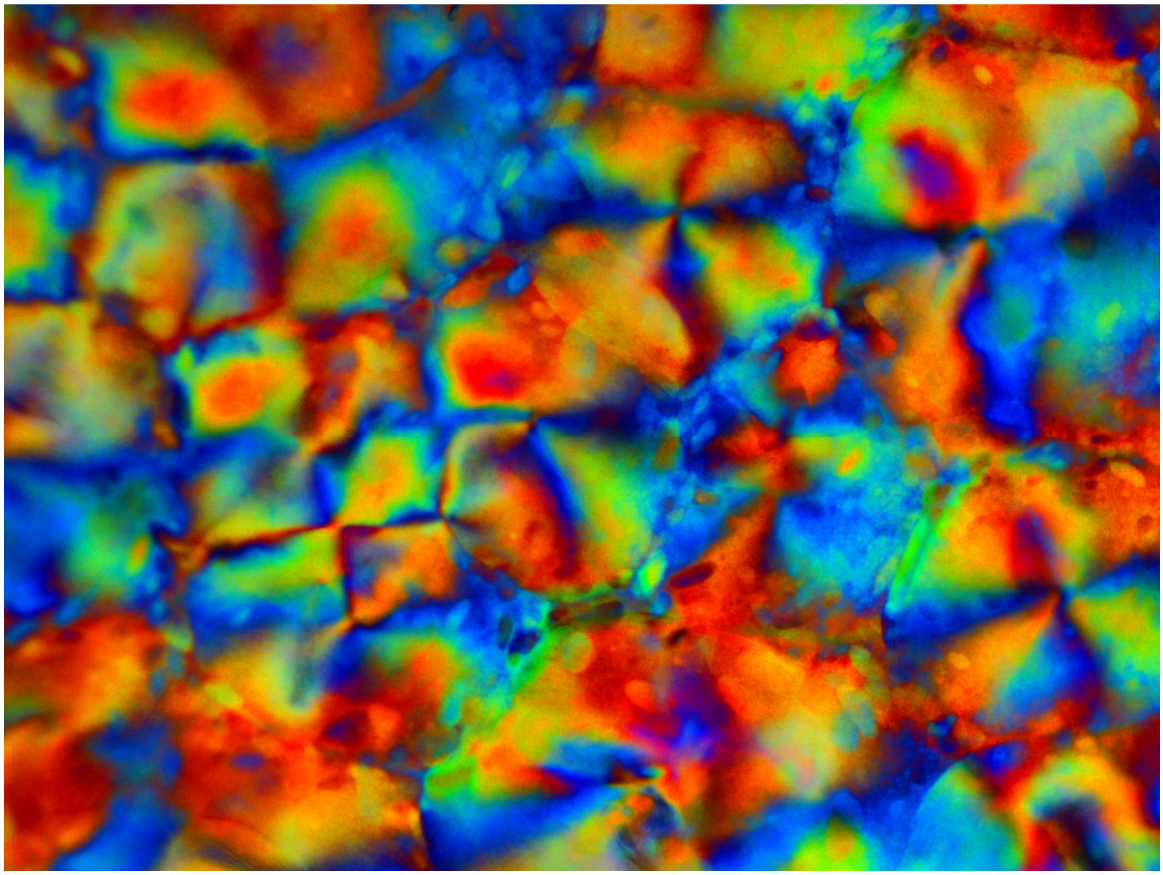

Urooj Gill did experimental design, data analysis, and writing for this chapter with editorial assistance and supervision from Dr. Jose M. Moran-Mirabal and Dr. Emily D. Cranston.

4.1. Abstract

A fundamental understanding of the mechanical properties of nanocellulose thin films is essential to be able to expand on their applications. Quantitative analysis of the mechanical properties of all-nanocellulose thin films is lacking in the literature, and the few studies that have measured the elastic modulus have reported significantly lower values than those predicted from the modulus of crystalline cellulose. In this work, we have used a pre-stressed polystyrene (PS) structuring approach to form wrinkled nanocellulose thin films as a way to measure their mechanical properties. Films containing cellulose nanocrystals (CNCs) and no other components (*i.e.*, "all-CNC" thin films) were fabricated, ranging in thickness from 0.04 – 71.1 μm and having one of three types of CNC orientation: chiral nematic, isotropic, or uniaxial (radial). This was achieved by depositing the CNCs on shrinkable PS substrates from suspensions ranging in concentration from 0.005 wt% – 8 wt%, which were dried under different conditions: i) slowly under vacuum (resulting in chiral nematic films), ii) rapidly with heating (leading to isotropic films), or iii) by spin-coating (yielding uniaxially, or radially, aligned films). These films were first assessed for changes in CNC optical anisotropy by polarized optical microscopy, which showed that the films had unique textures that changed with the drying conditions used (or with CNC orientation). These films were then structured through heat-induced shrinking of the PS substrate, where thick films delaminated from the substrate or completely cracked, while thinner films formed biaxially wrinkled features. Further investigation of the structured thin films showed that the surface and wrinkle morphology of the structured films could be easily tuned by changing the drying conditions used in the film fabrication procedure.

Future work involves evaluation of thin film mechanical properties as a function of CNC orientation where, with this knowledge, potential applications of these CNC films can be explored in areas such as tissue engineering, food packaging, and paper-based electronics.

4.2. Introduction

Understanding the mechanical properties of nanocellulose thin films is essential to guide current and future applications of these films in areas such as disposable packaging, optical coatings, biosensing, membrane filtration devices, electrodes, tissue engineering, antimicrobial films, food packaging materials, and paper-based electronics. In particular, the interest in using nanocellulose-based thin films as model cellulose surfaces[1–3] stems from their ability to mimic the robust interactions of cellulose microfibrils within plant cell walls. Understanding the structure and mechanics of plant cell walls is important because they are able to achieve high mechanical, tensile, and load-bearing strengths, and have a reported elastic modulus of around 130 GPa.[4–6] Within the cell wall, cellulose microfibrils form complex interactions with lignin and various hemicelluloses through cross-linking, hydrogen bonding, and van der Waals interactions, essentially forming a "nanocomposite". The combination and strength of the interactions in this "nanocomposite" are specifically what give the cell walls their impressive mechanical and tensile strengths. The motivation to use nanocellulose-based thin films as mimics for these complex interactions arises from their chemical and structural similarity to cellulose microfibrils. And so, the goal of working with nanocellulose-based films has been to produce neat films and composites that can mimic the strong mechanical properties of the cell wall, in order to expand on applications of these films and composites into areas that require high mechanical strength

materials. In this chapter, we study all-nanocellulose films which consist of nanoparticles with different orientations, in order to assess their mechanical properties using the structuring approach presented in Chapter 3.

Current knowledge of the elastic moduli of all-nanocellulose films is limited. The mechanical properties of thin films composed solely of cellulose nanofibrils (CNFs), cellulose nanocrystals (CNCs), or bacterial cellulose (BC) have been measured using dynamic mechanical analysis and tensile testing, where their reported elastic moduli are 6-15 GPa, 5-10 GPa, and 10-35 GPa, respectively.[7] Upper bound elastic moduli values have been calculated for cellulose nanoparticle-containing films through use of a concentric cylinders model,[8,9] which makes the assumption that the cellulose nanoparticles have long lengths, in order to treat them as continuous fibers.[7] In this model, cellulose nanoparticles have been treated as concentric cylinders, where an elastic modulus of 150 GPa for individual cellulose nanoparticles is used in these calculations. The upper bound elastic moduli for all-nanoparticle films, considering a 70-100 wt% loading of nanoparticles, have been calculated to be 50-60 GPa for films with fully isotropic (or random) nanoparticle orientations and 100-150 GPa for films with uniaxial nanoparticle orientations.[7] Experimentally, the thin films that most closely approach the upper bound limits are those composed of BC with isotropic nanoparticle orientations (25-35 GPa range)[10–12] and CNCs with > 72 wt% loadings (32.2-72 GPa range).[13] The mechanical properties of nanocellulose thin films are lower than the estimated upper bound values, which is hypothesized to be due to overestimations made by the model in terms of: the degree of interfacial interactions

between cellulose nanoparticles, the nanoparticle aspect ratio, and the degree of alignment in uniaxially aligned films.[7]

All-CNC films can be prepared through dip-coating of a substrate into a CNC suspension, or by or solvent-casting and drying a CNC suspension onto a substrate.[2,7,14] Drying methods used include evaporation, vacuum filtration, pressing, or freeze-drying, solvent exchange, or a combination of these methods, which produces films that consist of different CNC orientations.[7] Three specific types of nanoparticle orientations can be introduced into all-CNC thin films – chiral nematic, isotropic, and uniaxial (linear/radial).[7,15] Chiral nematic order, or helicoidal alignment, implies that each plane of CNCs is aligned in one linear direction (defined as the director), and the director of the subsequent CNC planes is rotated anticlockwise relative to the lower planes, achieving CNC ordering that is reminiscent of a spiral staircase.[16] This type of structure is accessible due to the self-assembling tendencies of CNCs to form a chiral nematic liquid crystal in aqueous suspensions, above a critical concentration. This organization can be locked into a dry film by evaporating the water in a controlled environment.[16] To produce all-CNC films with an isotropic orientation (*i.e.*, random orientation), CNCs can be adsorbed onto a substrate from a fully isotropic CNC suspension, or a solution-cast suspension can be dried rapidly onto a substrate (*e.g.*, by heating).[14] And lastly, to obtain a uniaxial orientation of CNCs, all-CNC films can be prepared with either linearly or radially aligned nanoparticles. Linear CNC alignments can be obtained in CNC films with applied shear forces,[14] dip-coating in anisotropic CNC suspensions,[17] or using Langmuir-Blodgett[18] or Langmuir-Schaeffer[19] depositions. Radial CNC alignments can be achieved by using magnetic fields

(with dilute suspensions, *i.e.*, below the critical concentration),[20] electric fields,[21] or by spin-coating of a suspension.[22,23] In this chapter, we used a few of these methods to produce all-CNC films with chiral nematic, isotropic, and uniaxial orientations.

To study the mechanical properties of these all-CNC films, we use a benchtop structuring approach, where thin films are prepared on pre-stressed polystyrene (PS) substrates which can be thermally shrunken to wrinkle the films.[24,25] When a film with a high elastic modulus is prepared on the PS substrates, the compressive stress generated during substrate shrinkage causes the film to wrinkle with the shrinking substrate, producing biaxially wrinkled surfaces. To date, this structuring approach has been used to structure metallic, glassy, and organic thin films.[13,24–27] Furthermore, this method has been used to extract the elastic modulus of CNC-polymer films, where changes in the mechanical properties of the biocomposite films were investigated as a function of film composition.[13]

As an extension of our previous work, we use this PS shrinking approach to investigate the mechanical properties of all-CNC thin films, and to assess how these properties change with nanoparticle orientation. All-CNC films are prepared through the direct evaporation of CNC suspensions (0.005 wt% – 8 wt%) onto pre-stressed PS substrates. Here, the suspensions are dried using three different evaporation conditions: 1) evaporation under vacuum (to achieve chiral nematic CNC order), 2) evaporation by heating (to achieve an isotropic orientation), and 3) evaporation by spin-coating (to achieve uniaxial CNC alignment). Once formed, these films are characterized for their texture as a function of the drying conditions used and the film thickness. Next, the films are structured by thermally shrinking the PS substrates. Thick films (prepared from high wt% CNC

suspensions), delaminate from the underlying substrate during the shrinking step, films of intermediate thicknesses (prepared from intermediate wt% suspensions) crack across the entire film surface, and thin films (prepared from low wt% suspensions) biaxially wrinkle without any film delamination or cracking occurring. From these results, we observe that structured all-CNC films have unique morphologies that are dependant on the CNC orientation within the films. In ongoing work, we are investigating whether these unique morphologies are a result of changes in the film's mechanical properties, due to varying nanoparticle orientations. With the knowledge of their modulus, the all-CNC thin films can be studied in applications most suitable to their mechanical properties, which includes areas such as tissue engineering, food packaging, and paper-based electronics.

4.3. Experimental

4.3.1. Production of Cellulose Nanocrystals (CNCs)

CNCs were produced through sulfuric acid hydrolysis of cotton, as reported previously.[16] Briefly, sulfuric acid (700 mL, 64 wt%, Sigma Aldrich, Oakville, ON, Canada) was added to 40 g cotton filter aid (Whatman ashless filter aid, GE Healthcare Canada, Mississauga, Canada),where it hydrolyzed the cotton source at 45°C for 45 minutes with constant mechanical stirring. The reaction was quenched by diluting the solution 10-fold in 18.2 MΩ cm Milli-Q water (Milli-Q A10 Purification System, Millipore, Etobicoke, Canada), after which it was decanted and repeatedly washed by centrifugation in 10-minute intervals at 5500*g* to remove excess acid. A stable CNC suspension was obtained when no pellet formed following centrifugation. This CNC

suspension was dialyzed against Milli-Q water with daily water exchanges for two weeks, until the pH of the external dialysis reservoir had stabilized, after which the suspension was sonicated in an ice bath using a point probe sonicator (Sonifier 450, Branson Ultrasonics, Danbury, CT), in three 15-minute intervals. The suspension was filtered through a glass microfiber filter (Whatman grade GF/B, VWR, Chicago, IL), yielding a suspension of 1 wt% CNCs with a pH of 3.89. The CNC suspension was prepared to the desired wt% concentrations through evaporation at ambient conditions, or by diluting with Milli-Q water. Sulfate half-ester content grafted to the CNCs was measured using conductometric titrations,[28] where sulfur content on the CNCs was determined to be 0.7 wt%. Dynamic light scattering (DLS) indicated that the average "apparent" size of the CNCs was 198 nm. Average CNC dimensions are typically 100-200 nm in length and 5-10 nm in height.[29]

4.3.2. Preparation of Polystyrene (PS) Substrates

PS substrates were prepared from pre-stressed PS shrink film (Graphix Shrink Film, Graphix, Maple Heights, OH). A CB15UB blade (Graphtec America Inc., Irvine, CA) was used with a force, quality and speed set of 30, 1, and 1, respectively, to cut the shrink film into 2 × 2 cm squares, using a Robo Pro CE5000-40-CRP cutter (Graphtec America Inc., Irvine, CA). Once cut, the PS squares were washed consecutively under orbital agitation in baths of isopropanol, ethanol and water for 5 minutes each at 50 rpm. Squares were dried using a nitrogen stream and stored until ready to use.

4.3.3. Fabrication of All-CNC Thin Films

Directly prior to using, PS squares were rinsed with isopropanol and dried using a nitrogen stream. Self-adhesive vinyl sheets (FDC-4300, FDC graphic films, South Bend, IN) were cut using the Robo Pro CE5000-40-CRP cutter, equipped with a CB09UA supersteel blade with force, quality and speed of 14, 1, and 1, respectively. These sheets were cut to have outer dimensions of 2 × 2 cm and inner circular dimensions with a radius of 0.846 cm. The circle in the center of the mask was removed, after which the masks were adhered to the PS substrates. Substrates were then oxidized by air plasma for 30 seconds at 600 mTorr (PDC001 Expanded Plasma Cleaner, Harrick Plasma, Ithaca, NY). The vinyl stencil was removed, directly after which CNC films were deposited in the plasma oxidized region of the PS. A total of 300 μL of CNC suspensions were drop-cast onto the oxidized PS, and three different evaporation protocols were used to dry the suspensions and form the all-CNC films: 1) drying under vacuum (chiral nematic ordering of CNCs), 2) drying by heat (isotropic ordering of CNCs), and 3) spin-coating (radial ordering of CNCs), as described further below.

To form thin films with chiral nematic ordering, CNC suspensions ranging in concentration from 0.005 – 8 wt% were drop-cast onto the plasma-treated region of the PS squares, then allowed to dry under vacuum (pressure < - 25 inHg) at room temperature, in an isotemp vacuum oven (Fisher Scientific, Ottawa, ON, Canada). Films with isotropically oriented CNCs were prepared by quickly drying suspensions (concentrations of 0.005 – 8 wt%) at 60°C under vacuum (pressure < - 25 inHg), in an isotemp vacuum oven for 1-2 hours. Lastly, to obtain a uniaxial (radial) alignment of CNCs in the films, 1 wt% CNC

suspensions were drop-cast onto the oxidized substrate, then spin-coated using a G3P Spincoat system (Specialty Coating Systems Inc., Indianapolis, IN) at 4000 rpm for 30 seconds, with a 7 second ramp. Films were annealed at 80°C for 1-2 hours in between each round of spin-coating, where films of varying thicknesses were prepared by varying the number of spin-coating rounds.

4.3.4. Structuring of All-CNC Films

To structure the all-CNC films, the PS substrates were shrunken above their T_g at 135°C for 5-10 minutes in the isotemp vacuum oven, in aluminum boats lined with parchment paper. The time was reduced from the previously reported protocol[13,24] in order to avoid the thermal degradation of cellulose.

4.3.5. Polarized Optical Microscopy (POM)

The planar and structured CNC films were imaged using the Nikon Eclipse LV100N POL epifluorescence microscope (Nikon Instruments, Mississauga, ON, Canada), equipped with 4, 10, 40, and 100x objectives. Transmitted images were taken between cross-polarizers with and without using a 530-nm retardation waveplate. The films were imaged with an Infinity 1 colour camera (Lumenera, Ottawa, ON, Canada) and the images were captured and saved using the Infinity Capture software (Lumenera, Ottawa, ON, Canada).

4.3.6. Variable Angle Spectroscopic Ellipsometry (VASE)

Ellipsometric data was obtained for all-CNC films prepared on PS substrates using a M-2000UI™ variable angle spectroscopic ellipsometer (J.A. Woollam Co., Inc., Lincoln, NE)

which spanned wavelengths of 250 – 1680 nm and angles from 55 – 70- degrees, in 5 degree increments. The CompleteEASE® Software was used to extract the thickness values of the films, where the Cauchy model was used to fit the ellipsometric data with the assumption that transparent films were present on the PS substrates.

4.3.7. Scanning Electron Microscopy (SEM)

SEM images of structured all-CNC films with varying CNC orientations were obtained using a JEOL JSM-7000S scanning electron microscope (JEOL USA, Inc., Peabody, MA), with an accelerating voltage of 2.5 kV, working distance of 6 mm, and a low probe current.

4.4. Results and Discussion

4.4.1. Fabrication of All-CNC Films

All-CNC films of thicknesses < 100 μm were prepared on 2 × 2 cm pre-stressed polystyrene (PS) substrates. A circular area in the center of these substrates (r = 0.846 cm) was selectively oxidized through plasma pre-treatment, and was the area of focus in the film fabrication process (Figure 4-1). CNC suspensions of varying concentrations were drop-cast onto the pre-treated PS and dried, where the method of suspension evaporation dictated the CNC arrangement within the films. It was observed that the cast CNC suspensions did not extend beyond the plasma oxidized area of the PS substrate. To obtain chiral nematic ordering of the CNCs, suspensions were slowly dried under vacuum, where the CNCs self-assembled into a chiral nematic orientation that was retained as the suspension dried down to a film. To form films with isotropically ordered CNCs,

suspensions were dried quickly by heating at 60°C. And lastly, CNC films with uniaxially (or radially) aligned nanoparticles were prepared by repeatedly spin-coating CNC suspensions onto PS substrates, with annealing steps following each coating step. Once these films were prepared, they were characterized for their optical anisotropy as a function of the evaporation method used and the film thickness.

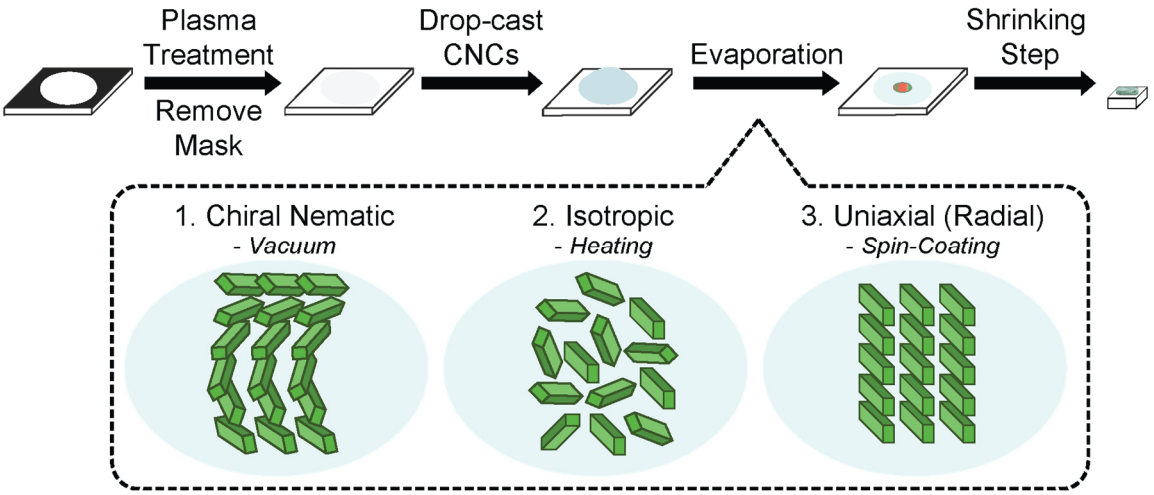

Figure 4-1. Fabrication method used to prepare all-cellulose nanocrystal (CNC) thin films. Polystyrene (PS) substrates were masked with a vinyl sheet, exposing only a circular region in the center of the substrates (r = 0.846 cm). The substrates were then oxidized with plasma, after which the vinyl sheets were removed from the PS. CNC suspensions of varying concentrations were drop-cast onto the PS substrates and allowed to evaporate. The method of evaporation used – drying under vacuum, heating, or spin-coating – dictated CNC orientation within the films – chiral nematic, isotropic, or uniaxial (radial). Once these films were prepared, they were then structured using a shrinking approach. PS substrates were heated above their glass transition temperature, which caused the substrates to shrink and the all-CNC films to subsequently structure.

Macroscopically, films prepared under vacuum and by heating looked very different from one another (Figure 4-2). Films dried under vacuum were iridescent, meaning that the colours observed changed with viewing angle. The iridescence was not

present in films of lower thicknesses (lower wt% suspensions), where it was completely absent in the 0.5 wt% film. The colour seen in the 0.5 wt% film was white, which is the characteristic colour of CNCs. All-CNC films prepared through heating were not iridescent and only showed a white colour for the full thickness range in Figure 4-2. These observations suggest that the CNC ordering in all-CNC films differs based on the drying conditions used and the film thickness. To confirm this, we next visualized the films using polarized optical microscopy (POM).

Films prepared with CNC suspensions ranging in concentration from 0.005 – 8 wt% were dried under vacuum and by heating (Figures 4-2 – 4-5). The thickness of these films was estimated with a known cellulose density of 1.5 g/cm^3,[30] which was used to determine the total volume of CNCs used per wt% suspension. Taking into account the dimensions of the film's area (restricted through plasma treatment), the volume was then used to calculate for h (film thickness). These thickness values are shown as insets in Figures 4-3 and 4-5. Films were imaged by POM to assess changes in CNC orientation as a function of the drying method used and the film thickness, where the center of the films was the area of focus for all imaging. When using a polarized optical microscope (equipped with a 530 nm red waveplate) for qualitative assessment of a sample, an array of colours can be seen. When a magenta (or purple) colour is seen there is no optical anisotropy present within the sample (*e.g.*, the sample has randomly oriented molecules). When an array of colours (other than magenta) are seen in a sample, this indicates that the sample is birefringent and consists of preferentially oriented specimen, where changes in the direction and type of specimen orientation changes the colours seen under the polarized optical microscope.

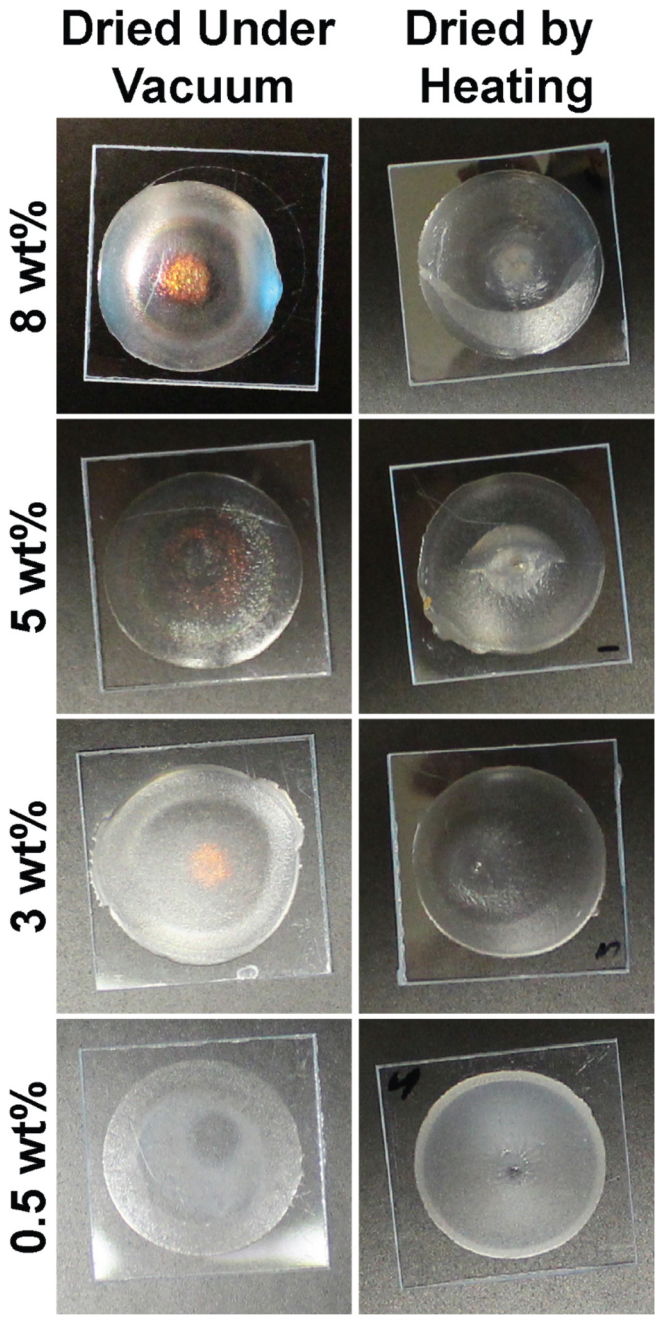

Figure 4-2. Macroscopic view of all-CNC films prepared from concentrated CNC suspensions, that were either dried slowly under vacuum (left) or quickly by heating (right).

Films prepared under vacuum and by heating showed an array of colours under the polarized microscope, indicating that the CNCs had a preferred orientation within the films

(Figures 4-3 – 4-5). When looking at films dried under vacuum, we observed that films with thicknesses ranging from 8.9 – 71.1 μm (1 wt% – 8 wt% suspensions) showed a fingerprint texture (Figures 4-3 and 4-4). This fingerprint pattern has previously been seen under the polarized optical microscope for CNC suspensions and all-CNC thin films that consist of a chiral nematic ordering of CNCs,[16,31] where the spacing between two consecutive lines corresponds to half the chiral nematic pitch. A film that has a full chiral nematic pitch on the order of visible light is iridescent by eye, and this iridescence was observed in films of thicknesses ranging from 8.9 – 71.1 μm (*c.f.* Figure 4-2). These results tell us that all-CNC films prepared under vacuum had a chiral nematic ordering of CNCs. This chiral nematic order was continuous throughout films of thicknesses beyond 44 μm (5 and 8 wt% films) (Figure 4-4). However, this continuity was disrupted in films with thicknesses ranging from 8.9 – 26.7 μm (1 and 3 wt% films), where the fingerprint pattern became more short-ranged (tactoid-like pattern). This indicates that the chiral nematic order within these films did not extend indefinitely across the whole film surface. The 4.4 μm thick film (0.5 wt% film) showed a Maltese cross-like pattern by POM (Figure 4-3), where the film had a radial nanoparticle alignment that extended outwards from the center of the Maltese cross pattern. This film may also consist of tactoids (short-ranged chiral nematic order), but could not be visualized since the radial planes of CNCs produced dominant textures that overshadowed other textures present within the film. With these observations in mind, we then looked at all-CNC films prepared by heating, to see how their optical anisotropy differed from the all-CNC films prepared under vacuum.

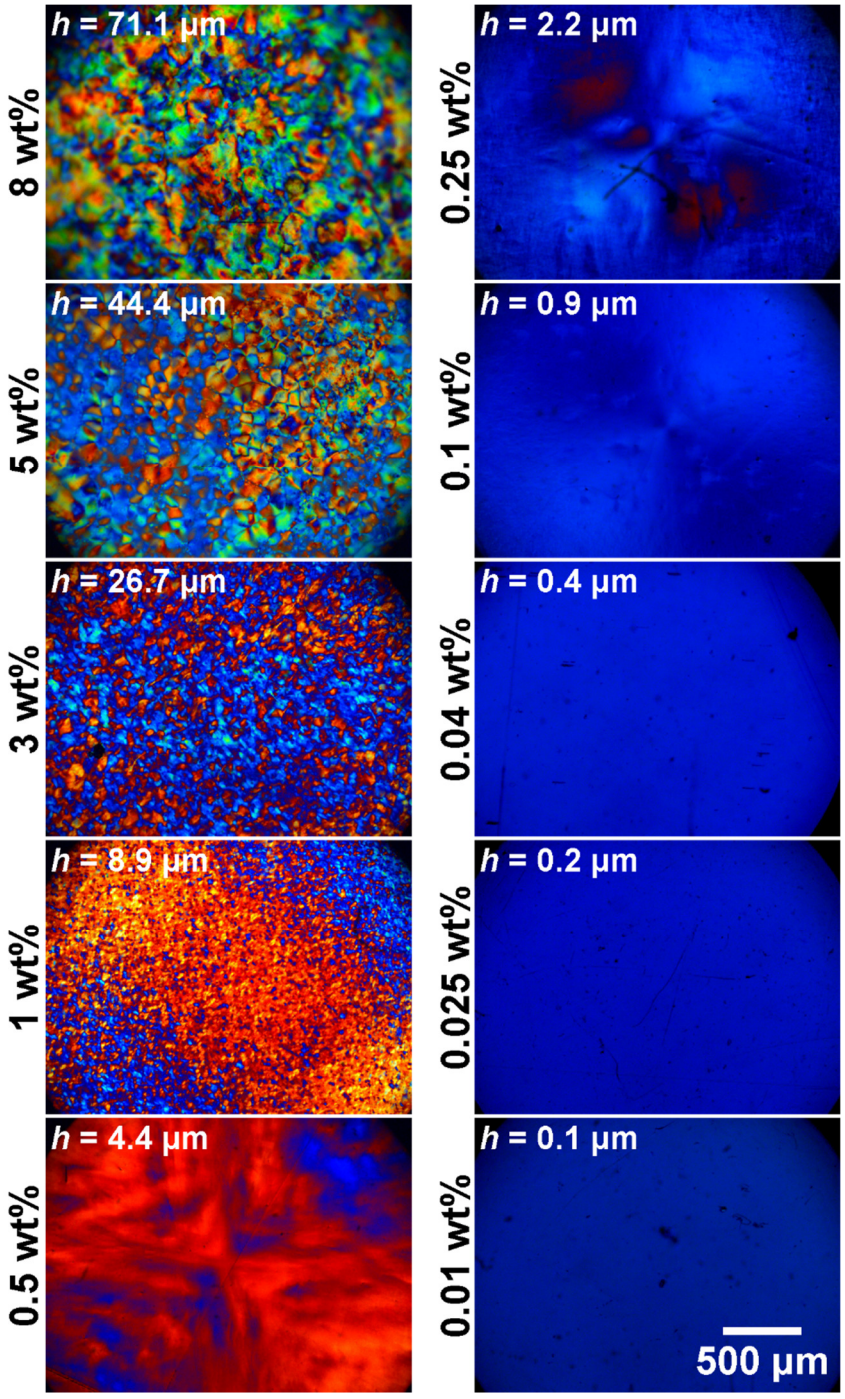

Figure 4-3. Polarized optical microscopy (POM) images of all-CNC films prepared by drying CNC suspensions under vacuum. Films showed distinct textures when prepared at thicknesses beyond 0.8 µm (CNC wt% ≥ 0.1), but showed little-to-no texturing at thicknesses lower than 0.5 µm (CNC wt% ≤ 0.04). The estimated film thickness (h) at each wt% suspension is shown as an inset in the POM images. Images were taken in the centre of the film between crossed polarizers, using a 530 nm retardation waveplate.

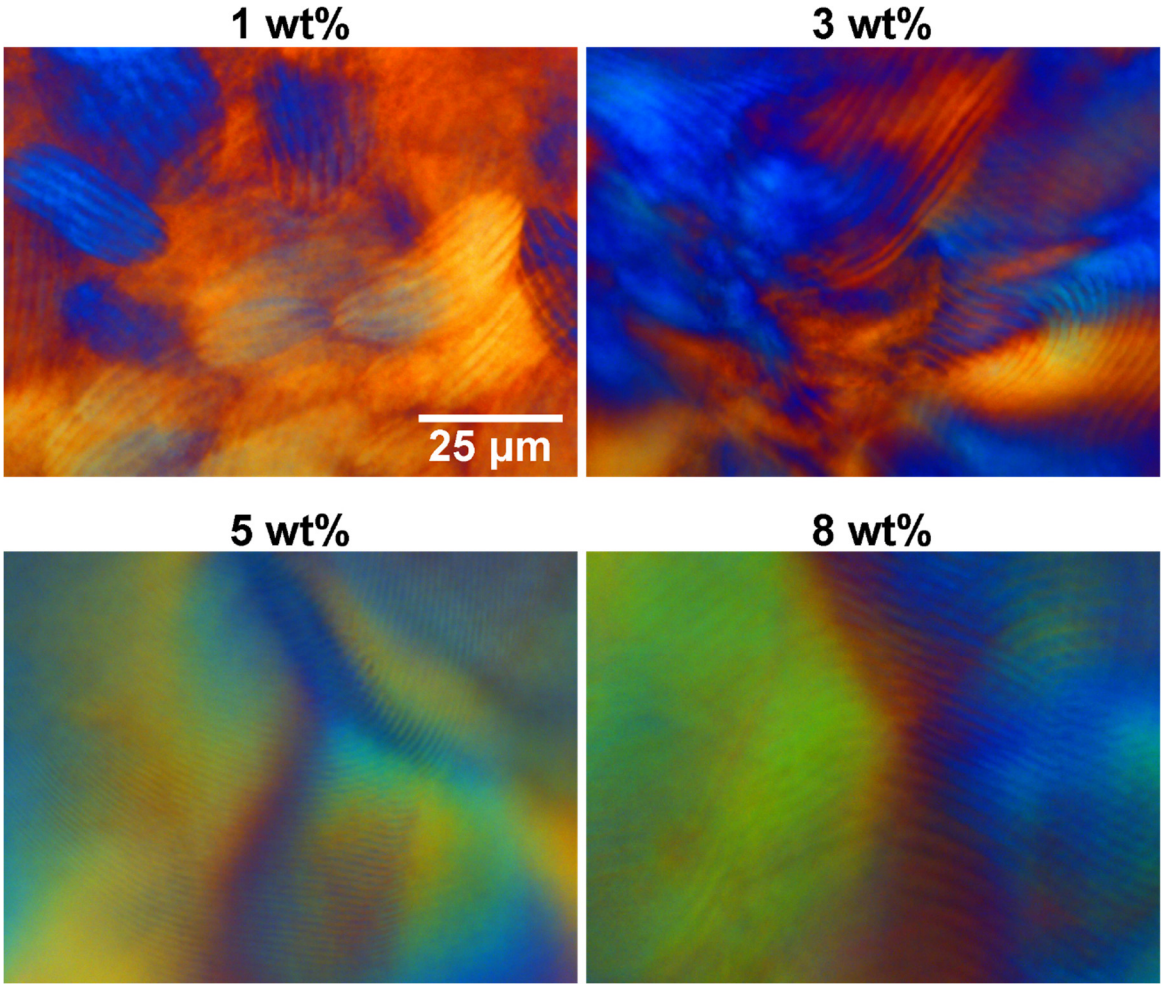

Figure 4-4. POM images taken at 100x of all-CNC films prepared under vacuum. Fingerprint texture is present in these films, and is a result of chiral nematic CNC orientations. Images were taken in the centre of the film between crossed polarizers, using a 530 nm retardation waveplate.

All-CNC films fabricated by drying suspensions under heat showed very distinct textures by POM (Figures 4-5 and B-1) compared to films dried under vacuum (*c.f.* Figures 4-3 and 4-4). The goal of drying CNC suspensions by heat was to prepare films with isotropically oriented CNCs. Films with thicknesses ranging from 26.7 – 71.1 µm (3 wt% – 8 wt% films) showed highly polydomain textures throughout the film surface by POM.

This polydomain texture was a result of short-ranged ordering of the nanoparticles, which occurred due to the high CNC content within the suspensions and their close proximity to one another. Higher magnification images of these films showed that there was some fingerprint texture present within these films, indicating the presence of some chiral nematic CNC order (Figure B-1). The fingerprint texture was more continuous in the 5 wt% and 8 wt% films, but was short-ranged (tactoids) in the 3 wt% films (similar to our observations for films dried under vacuum, *c.f.* Figure 4-4). Films with thicknesses ranging from 4.4 – 8.9 μm (0.5 wt% and 1 wt% films) showed a Maltese cross-like pattern by POM, indicating that there was a radial alignment of CNCs within these films (Figures 4-5 and B-1). At higher magnifications, these films did not show tactoid formation, but instead had a grainy polydomain texture (Figure B-1) which was of shorter-range than the polydomain texture seen in films with thicknesses of 26.7 – 71.1 μm (dried by heat). With the knowledge obtained from films dried under vacuum and by heat, we next assessed whether the textures seen in these films could also be observed in thinner films prepared using the same drying conditions.

Films dried under vacuum with thicknesses of 0.9 – 2.2 μm (0.1 wt% – 0.25 wt% films) showed a Maltese cross-like pattern by POM, indicating a radial alignment of CNCs (Figure 4-3). Once again, these films may consist of tactoids, but this could not be visualized by POM due to the dominant Maltese cross-like texture present. When films of thicknesses below 0.5 μm (0.01 wt% – 0.04 wt% films) were prepared and visualized by POM, we observed a blue colour (Figure 4-3). This blue colour was not a result of CNC orientation within the films, but was seen due to the birefringence of the pre-stressed PS

substrate (Figure B-2). There was no obvious texture present in the films other than the PS substrate background; however, there may still be a preferred CNC orientation within these films in the form of tactoids. This was difficult to visualize due to the low film thickness, where the pitch of the tactoids may be reaching sub-nanometer ranges that are too small for the microscope to detect (particularly over the PS background colour). Other potential methods that could be used to assess these films for a chiral nematic orientation are UV-Vis diffuse reflectance, which could quantify a pitch if it is present, or scanning electron microscopy (SEM), which could be used to visualize a cross-section of these films.

We next visualized films dried by heat which had thicknesses of 0.9 – 2.2 μm (0.1 wt% – 0.25 wt% films) (Figure 4-5). These films showed grainy polydomain textures by POM, suggesting that these films had an isotropic ordering of CNCs. When we prepared thinner films ($h \leq 0.4$ μm; 0.01 wt% – 0.04 wt% films), we observed that no texture could be seen in these films other than the blue colour of the birefringent PS substrate (Figure B-2). Once again, this suggests that the order that was present within these films may be on the sub-nanometer range, and is too short-ranged to detect using the microscope. In the literature (when using POM), it has been reported that undisturbed dilute CNC suspensions (below the critical concentration) show tactoid formation,[16] while rapidly drying CNC suspensions show distorted and grainy polydomain textures,[32] where all of these suspensions can be dried down to "lock" these CNC orientations in place. With the texturing that our all-CNC films showed at thicknesses > 0.5 μm, we inferred that films prepared at thicknesses < 0.5 μm had short-range chiral nematic ordering (in the form of

tactoids) and short-range isotropic ordering (in the form of polydomain texturing) for films dried under vacuum and by heat, respectively.

Lastly, to obtain a uniaxial (radial) orientation of CNCs, a 1 wt% CNC suspension was spin-coated onto pre-stressed PS substrates several times (N) to produce films of thicknesses ranging from 0.2 – 0.49 μm (determined by variable angle spectroscopic ellipsometry (VASE), since these values could not be estimated by the calculations discussed above) (Figure 4-6). These films did not show any texture under the polarized microscope, other than the blue colour seen for the birefringent pre-stressed PS (Figures 4-6 and B-3). Previously, CNC films produced via spin-coating have shown radial CNC orientations by POM for micrometer-scale ordering; however, this ordering becomes difficult to distinguish when working on the nanometer-scale,[22] which is also what we observe in our spin-coated films. From this, we infer that the CNCs in our all-CNC films are radially aligned but have short-ranged ordering that is difficult to distinguish with POM.

Characterization of these all-CNC films by POM showed that we could produce all-CNC films with unique optical anisotropies, by simply adjusting the film preparation method used (vacuum, heat, or spin-coating) and the film thickness (wt% suspension, or number of spin-coating rounds). We fabricated CNC films with different CNC orientations – chiral nematic, isotropic, and uniaxial (radial), where the next step in our procedure was then to structure the films and assess the morphology of the resulting wrinkles.

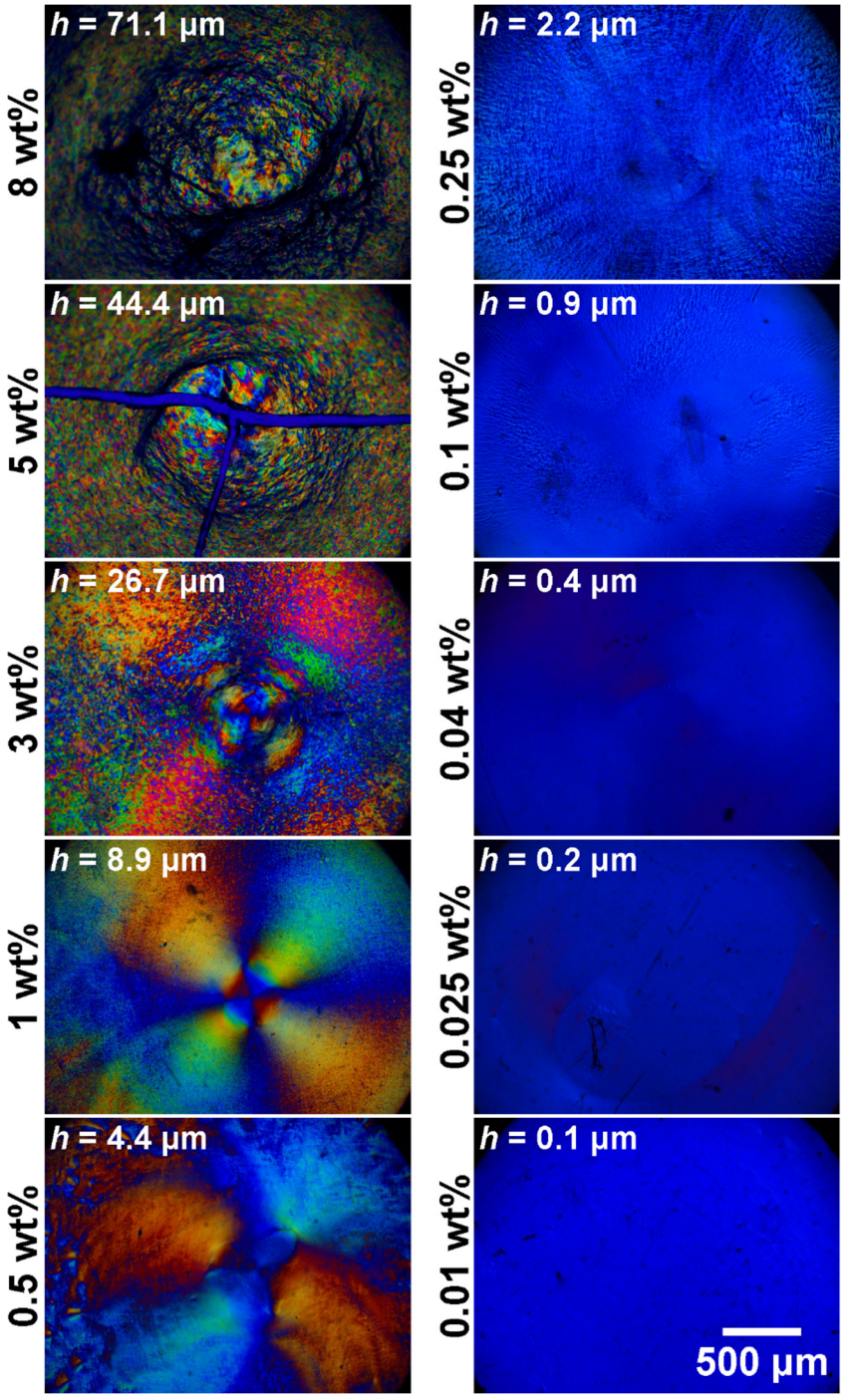

Figure 4-5. POM images of all-CNC films prepared by drying CNC suspensions through heating. Films showed distinct textures when prepared at thicknesses beyond 2 µm (CNC wt% ≥ 0.25), but exhibited little-to-no texturing at thicknesses below 1 µm (CNC wt% ≤ 0.1). The estimated film thickness (h) at each wt% suspension is shown as an inset in the POM images. Images were taken in the centre of the film between crossed polarizers, using a 530 nm retardation waveplate.

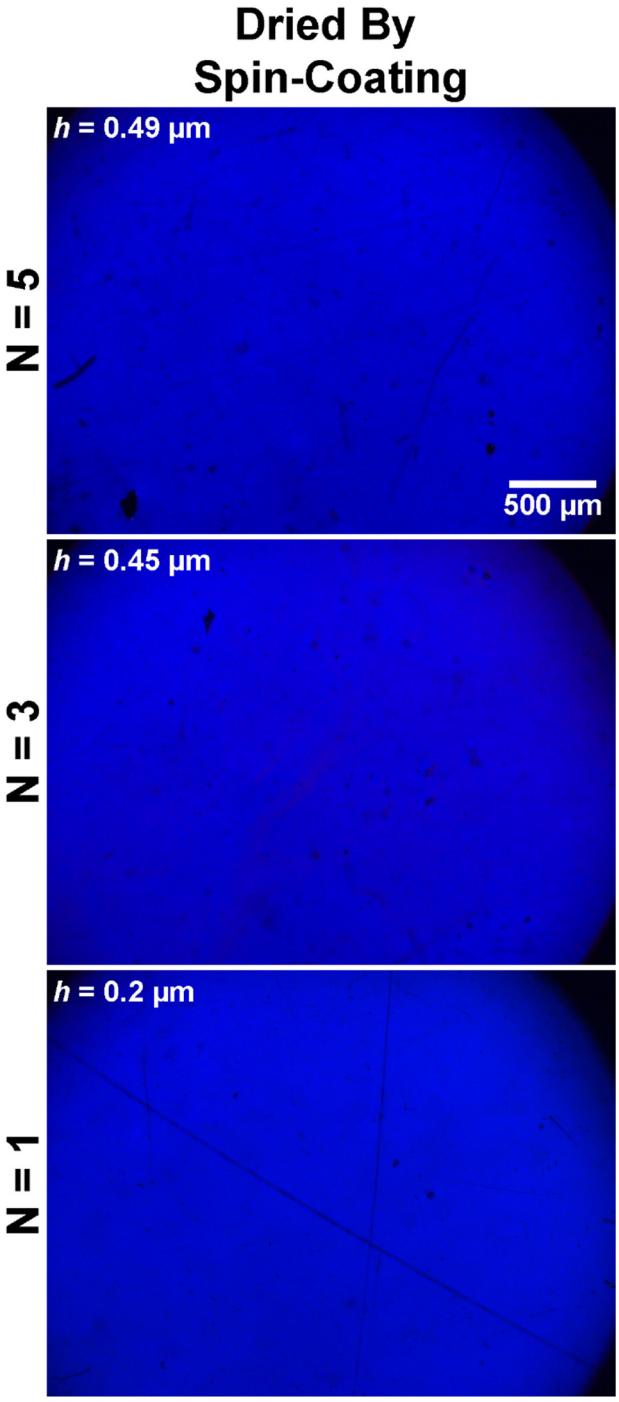

Figure 4-6. POM images of all-CNC films prepared by spin-coating of CNC suspensions. A 1 wt% CNC suspension was spin-coated multiple times (N) on PS substrates to produce films of thicknesses ranging from 0.2 – 0.49 µm. Film thickness (h) was determined by variable angle spectroscopic ellipsometry (VASE), and is shown as an inset within the POM images. Images were taken in the centre of the film between crossed polarizers, using a 530 nm retardation waveplate.

4.4.2. Structuring of All-CNC Films

Once these all-CNC films were prepared and characterized, they were structured using a shrinking approach (Figure 4-1).[24,25] Heating PS substrates above their glass transition temperature (100°C) causes them to shrink, generating compressive stress where the films buckle and wrinkle with the shrinking substrate. The wrinkling occurs as a result of the elastic modulus mismatch between the film and the underlying PS substrate. Using this PS-based structuring approach, we wrinkled all-CNC films (that were dried under vacuum) at different thicknesses (prepared from high, intermediate, and low wt% CNC suspensions), and assessed their morphology using SEM (Figure 4-7).

Thicker films (wt% $\geq$ 3, h $\geq$ 26.7 μm) delaminated from the PS substrate during shrinking, leaving behind a thin layer of CNCs that remained adhered to the underlying PS substrate. When viewed by SEM, we observed that this thin CNC layer had structured with the shrinking substrate, producing structured films with a wispy and rough morphology (Figure 4-7). While these films wrinkled, they could not be analyzed for their elastic modulus since the wrinkled features were not representative of a continuous film. Next, we structured intermediate thickness films (0.1 – 1 wt%, 0.9 μm $\leq$ h $\leq$ 8.9 μm). These films did not delaminate from the PS substrate, but instead structured and cracked across the entire film surface (Figure 4-7). This occurred because the compressive stress generated during shrinking could not be released solely through wrinkling of the films, and so the films also cracked at the regions of highest stress (the wrinkle ridges). While these films were successfully structured, the fact that they severely cracked prevented their use in the calculation of the film's mechanical properties. From this, we next structured thinner films

(≤ 0.05 wt%, thickness ≤ 0.4 μm) and found that these films did not delaminate or crack during the structuring process, but instead formed biaxially wrinkled surfaces (Figure 4-7). These films had a sufficient stiffness mismatch with the soft underlying PS substrate, which is the reason they were able to form biaxially wrinkled features following the shrinking step. Here, we observed that as films were prepared with lower wt% suspensions, we approached low enough film thicknesses where delamination and cracking no longer occurred. Through these experiments, we identified a CNC film thickness (wt%) range (thickness ≤ 0.4 μm, corresponding to films of concentration ≤ 0.05 wt%) that was suitable for forming biaxially wrinkled CNC films (dried under vacuum) with little-to-no defects present in the wrinkles (*e.g.*, cracking).

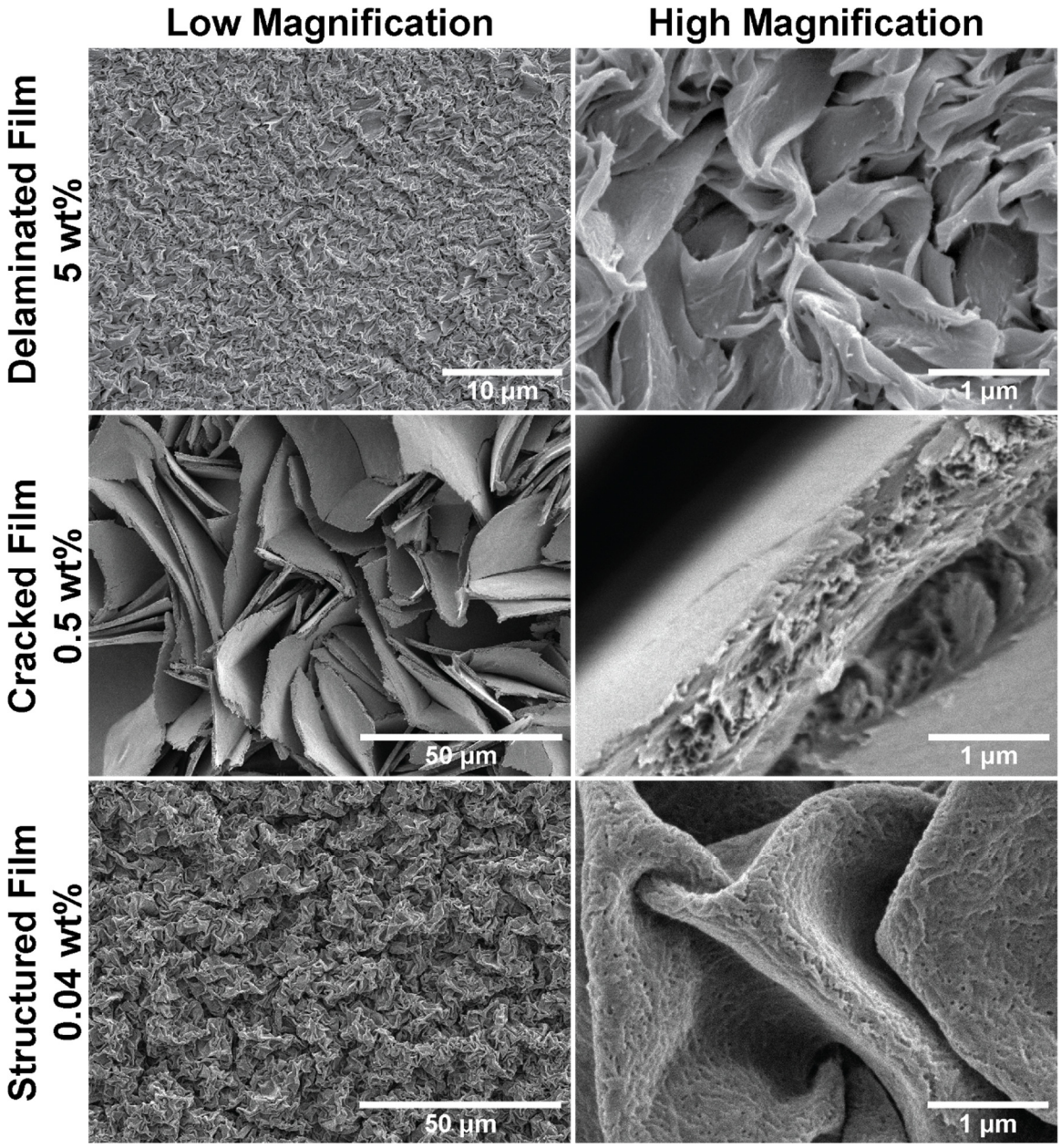

Figure 4-7. SEM images of structured all-CNC films that were prepared under vacuum. Films of thicknesses beyond 26 µm (CNC wt% ≥ 3) delaminated from the underlying substrate during structuring, leaving behind a thin CNC film that structured with the shrinking substrate. Structured films of thicknesses ranging from 0.9 – 8.9 µm (CNC wt% between 0.1 and 1) did not delaminate from the substrate, but were cracked across the entire film surface. When films were structured with thicknesses below 0.5 µm (CNC wt% ≤ 0.05), they biaxially wrinkled with the shrinking substrate and did not delaminate or crack.

Next, we structured thin films prepared through rapid thermal-drying, to find the thickness range that produced biaxially wrinkled features with no film cracking or delamination taking place. Films at intermediate and low wt% concentrations were structured (0.25 wt% – 0.04 wt%, 2.2 μm ≥ h ≥ 0.4 μm) and viewed under SEM (Figure B-4). All of these films cracked at the wrinkle ridges, with the exception of the 0.04 wt% film (h = 0.4 μm), which formed biaxially wrinkled features with no full wrinkle cracking present. From these experiments, we learned that films prepared by heating with thicknesses at or below 0.4 μm formed continuous wrinkled features. From our observations of the structured films prepared under vacuum and by heating, it is clear that CNC films have a maximum thickness at which they can be uniformly structured, beyond which they will crack at the wrinkle ridges. Based on the estimated thickness of these drop-cast films (0.4 μm), an upper bound for the ability to structure the thin films without cracking was determined to be on the order of 0.5 μm.

With the upper bound thickness for continuous film structuring in mind, we prepared thin all-CNC films (low CNC wt% or low number of spin-coating rounds) by drying under vacuum, by heat, or through spin-coating, structured them, and then assessed their morphology by POM and SEM (Figure 4-8). POM images of these wrinkles showed that the CNCs in the wrinkles had a preferred orientation that was the same across all films, regardless of the drying conditions used or the film thickness, an observation which could not be observed prior to film structuring (*c.f.* Figures 4-3 and 4-5). The colours observed were most likely because a 3-dimensional distribution of CNCs was introduced following structuring. In this distribution, the CNCs changed from being primarily aligned parallel to

the substrate surface (wrinkle ridges), to having alignments perpendicular to the surface (regions of steepest slope), along with alignments anywhere in between the parallel and perpendicular directions.

By SEM, we observed that as the film thickness increased (higher wt% suspensions in films dried by vacuum and heat, higher N in spin-coated films) the size of the biaxial wrinkles increased as well (Figure 4-8), which agrees with previous observations for continuous films.[13,24,33] A qualitative assessment of the wrinkle morphology showed that the roughness and topography of the wrinkled features was affected by the drying conditions used to prepare the films (Figures 4-8 and 4-9). This was especially apparent when looking at films prepared to similar thicknesses, as seen in Figure 4-9. The all-CNC films also had a rougher morphology than CNC-polymer films[13] prepared using this PS structuring approach. This was expected, since the structured all-CNC films were not plasticized by the addition of a component polymer. A comparison of wrinkle morphology based on drying conditions suggests that all-CNC films prepared by heating had the roughest morphology, while films prepared under vacuum had the smoothest morphology. In addition, differences in wrinkle morphology were also observed, where spin-coated films exhibited very narrow wrinkle ridges and had closely packed wrinkled features compared to the other films prepared.

The difference in wrinkle morphology is likely a result of the CNC orientation within the all-CNC films, where wrinkling in these films primarily occurs at the "defect" spots within the film (*e.g.*, areas of weaker CNC-CNC interactions). Films that were dried under vacuum or by heat had areas of short-range chiral nematic order (tactoid formation)

or polydomain order, respectively. Defects in these films occurred around these ordered regions, which had sizes on the order of the length of CNCs. In spin-coated films, the CNCs were aligned uniaxially, and so defects in these films occurred across the width (or several widths) of the CNCs, where the width of a CNC is 10-20 times shorter than its length. When films prepared under vacuum or by heat were structured, wrinkling occurred at defect regions external to the tactoid and polydomain regions (which are not entropically favourable to break), producing larger wrinkled features. When spin-coated films were structured, the wrinkling occurred at defect regions between areas of uniaxially aligned CNCs. The spacings of these defects were on the order of one or a few CNC widths, and so the resulting structured films produced narrower wrinkled features.

Through these experiments, we have observed that structured all-CNC films could be produced without film delamination or film cracking, by reducing film thicknesses below 0.5 μm. Thinner films were prepared by solvent-casting from lower wt% suspensions (in films dried under vacuum or by heat) or by reducing the number of deposition rounds (in spin-coated films). It was also observed that the morphology of structured all-CNC films could easily be tuned by changing the drying method used, where the roughness and wrinkle morphology drastically changed between drying methods, due to the underlying CNC arrangement in the films.

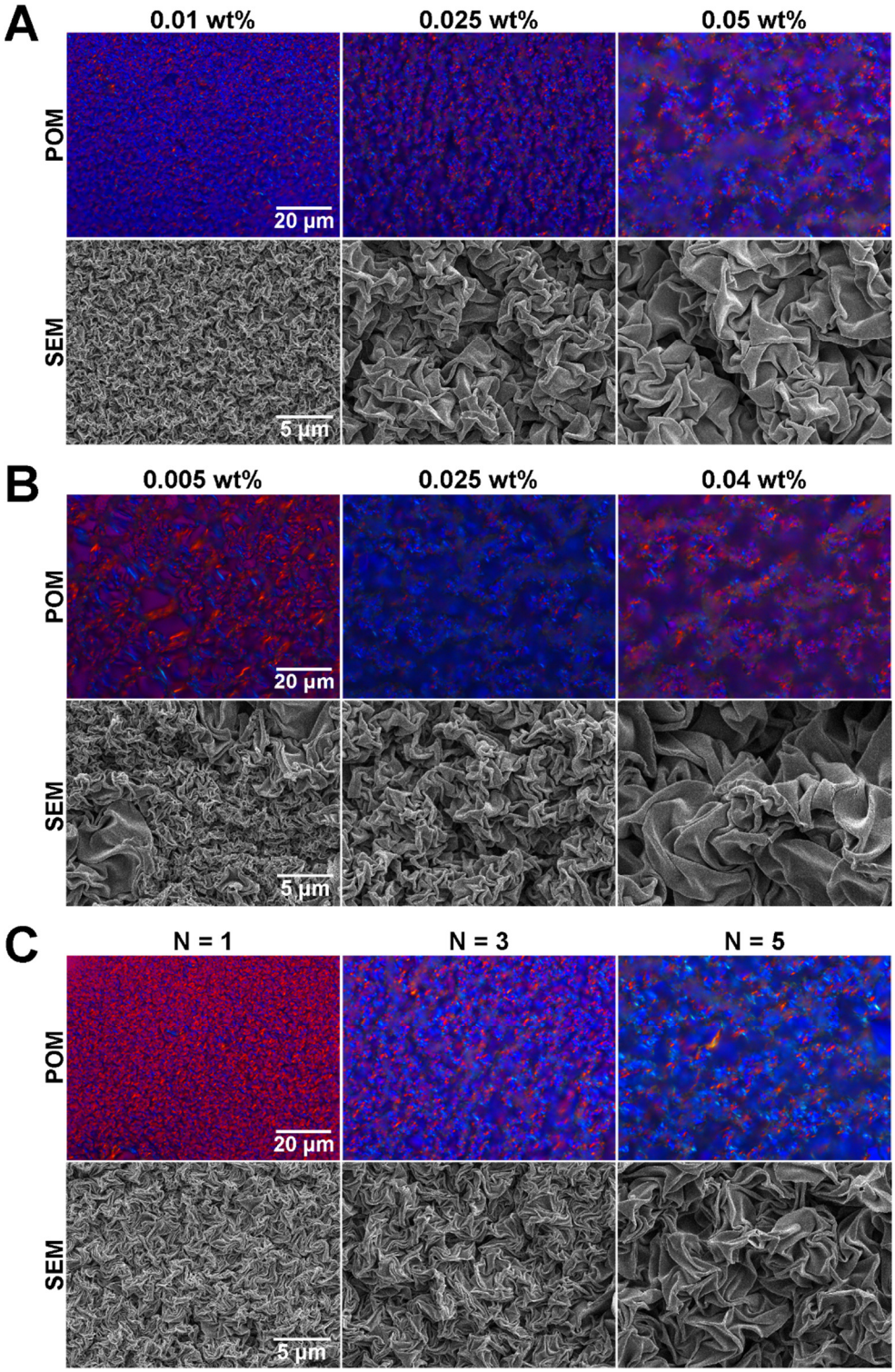

Figure 4-8. POM and SEM images for structured thin all-CNC films dried A) under vacuum, B) by heating, or C) through spin-coating (with N number of subsequent depositions, or varying film thicknesses).

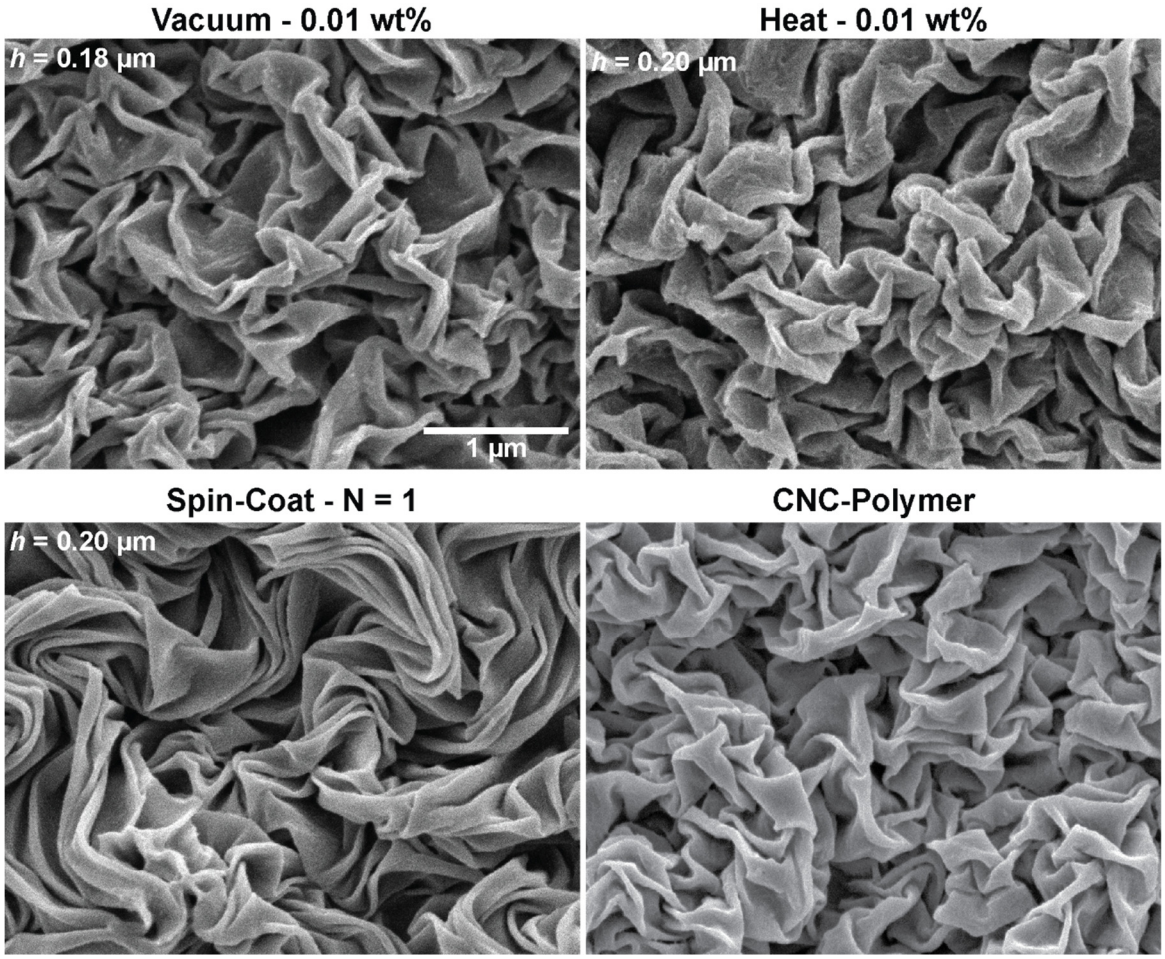

Figure 4-9. SEM comparison of structured all-CNC films prepared at near identical thicknesses. Thickness (h) values are shown as an inset of the SEM images, and were measured by VASE. An SEM image of a CNC-polymer film is also shown.

4.5. Conclusions

In this study, we have reported the use of a structuring approach to wrinkle all-nanocellulose thin films that had unique morphologies and were easily tunable through simple modifications in the film fabrication process. This is the first report of a structuring approach being used to wrinkle all-CNC thin films, something that has been difficult to achieve in the past due to the brittle nature of nanocellulose films. To overcome these

limitations, we adjusted the drying conditions used (drying under vacuum, by heating, or by spin-coating) and the film thickness (varying wt% suspensions, or various rounds of deposition steps) to produce films that consisted of CNCs with varying orientations (chiral nematic, isotropic, or uniaxial). When these films were structured, films of thicknesses ≥ 26.7 μm delaminated from the underlying substrate, films of thicknesses between 0.9 – 8.9 μm completely cracked, and films of thicknesses below 0.5 μm biaxially wrinkled with little-to-no cracking present. Knowing the thickness range that produced structured morphologies with no film cracking, we next fabricated structured all-CNC films within this thickness range. The structured films had distinct surface and wrinkle morphologies between drying conditions, where films dried by heat showed the roughest morphology, and films dried via spin-coating had the narrowest and most tightly packed wrinkled features. Future work in the characterization of these thin films includes determining their characteristic wrinkle length, and using that to extract their mechanical properties, in order to relate this information to CNC orientation within the films. With the knowledge of the mechanical properties of these all-CNC thin films, they may find potential applications in areas such as tissue engineering, food packaging, and paper-based electronics.

4.6. Acknowledgements

We thank S Saem for help with scanning electron microscopy, and P Mascher for access to VASE instrumentation. UG is the recipient of an Ontario Graduate Scholarship, and JMM and EDC are recipients of Early Researcher Awards from the Ontario Ministry of Research and Innovation. This research was supported by funding through the Natural Sciences and Engineering Research Council, and made use of instrumentation from the

Canadian Centre for Electron Microscopy and the Centre for Emerging Device Technology.

4.7. References

(1) Kontturi, E.; Tammelin, T.; Österberg, M. Cellulose—model Films and the Fundamental Approach. *Chem. Soc. Rev.* **2006**, *35*, 1287–1304.

(2) Cranston, E. D.; Gray, D. G. Model Cellulose I Surfaces: A Review. In *Model Cellulosic Surfaces*; Roman, M., Ed.; ACS Symposium Series; ACS Publishing: Washington, DC, 2009; pp 75–93.

(3) Aulin, C.; Ahola, S.; Josefsson, P.; Nishino, T.; Hirose, Y.; Österberg, M.; Wågberg, L. Nanoscale Cellulose Films with Different Crystallinities and Mesostructures—Their Surface Properties and Interaction with Water. *Langmuir* **2009**, *25* (13), 7675–7685.

(4) Nakamae, K.; Nishino, T. 1998, 5, 73–78. *Cellul. Commun.* **1998**, *5*, 73–78.

(5) Nishino, T.; Takano, K.; Nakamae, K. J. Elastic Modulus of the Crystalline Regions of Cellulose Polymorphs. *Polym. Sci., Part B Polym. Phys.* **1995**, *33* (11), 1647–1651.

(6) Sakurada, I.; Nukushina, Y.; Ito, T. Experimental Determination of the Elastic Modulus of Crystalline Regions in Oriented Polymers. *J. Polym. Sci.* **1962**, *57* (165), 651–660.

(7) Moon, R. J.; Martini, A.; Nairn, J.; Simonsen, J.; Youngblood, J. Cellulose Nanomaterials Review: Structure, Properties and Nanocomposites. *Chem. Soc. Rev.* **2011**, *40*, 3941–3994.

(8) Hashin, Z.; Rosen, B. W. The Elastic Moduli of Fiber-Reinforced Materials. *J. Appl. Mech.* **1964**, *31*, 223–232.

(9) Hashin, Z. *Mechanics of Composite Materials*; Pergamon Press: Oxford, UK, 1969.

(10) Yamanaka, S.; Watanabe, K. *Cellulosic Polymers: Blends and Composites*; Gilbert, R., Ed.; Hanser: New York, 1994.

(11) Takai, M. *Cellulosic Polymers: Blends and Composites*; Gilbert, R. D., Ed.; Hanser: New York, 1994.

(12) Watanabe, K.; Tabuchi, M.; Morinaga, Y.; Yoshinaga, F. Structural Features and Properties of Bacterial Cellulose Produced in Agitated Culture. *Cellulose* **1998**, *5* (3), 187–200.

(13) Gill, U.; Sutherland, T.; Himbert, S.; Zhu, Y.; Rheinstädter, M. C.; Cranston, E. D.; Moran-Mirabal, J. M. Beyond Buckling: Humidity-Independent Measurement of the Mechanical Properties of Green Nanobiocomposite Films. *Nanoscale* **2017**, *9* (23), 7781–7790.

(14) Abitbol, T.; Cranston, E. D. Directed Assembly of Oriented Cellulose Nanocrystal Films. In *Handbook of Green Materials*; World Scientific: Hackensack, NJ, 2014; Vol. 3, pp 79–103.

(15) Abitbol, T.; Cranston, E. D. Chiral Nematic Self-Assembly of Cellulose Nanocrystals in Suspensions and Solid Films. In *Handbook of Green Materials*; World Scientific: Hackensack, NJ, 2014; Vol. 3, pp 37–56.

(16) Revol, J.-F.; Bradford, H.; Giasson, J.; Marchessault, R. H.; Gray, D. G. Helicoidal Self-Ordering of Cellulose Microfibrils in Aqueous Suspension. *Int. J. Biol. Macromol.* **1992**, *14*, 170–172.

(17) Jean, B.; Dubreuil, F.; Heux, L.; Cousin, F. Structural Details of Cellulose Nanocrystals/Polyelectrolytes Multilayers Probed by Neutron Reflectivity and AFM. *Langmuir* **2008**, *24* (7), 3452–3458.

(18) Habibi, Y.; Foulon, L.; Aguié-Béghin, V.; Molinari, M.; Douillard, R. Langmuir-Blodgett Films of Cellulose Nanocrystals: Preparation and Characterization. *J. Colloid Interface Sci.* **2007**, *316*, 388–397.

(19) Habibi, Y.; Hoeger, I.; Kelley, S. S.; Rojas, O. J. Development of Langmuir-Schaeffer Cellulose Nanocrystal Monolayers and Their Interfacial Behaviors. *Langmuir* **2010**, *26* (2), 990–1001.

(20) Revol, J.-F.; Godbout, L.; Dong, X.-M.; Gray, D. G.; Chanzy, H.; Maret, G. Chiral Nematic Suspensions of Cellulose Crystallites; Phase Separation and Magnetic Field Orientation. *Liq. Cryst.* **1994**, *16* (1), 127–134.

(21) Bordel, D.; Putaux, J.-L.; Heux, L. Orientation of Native Cellulose in an Electric Field. *Langmuir* **2006**, *22*, 4899–4901.

(22) Edgar, C. D.; Gray, D. G. Smooth Model Cellulose I Surfaces from Nanocrystal Suspensions. *Cellulose* **2003**, *10*, 299–306.

(23) Lefebvre, J.; Gray, D. G. AFM of Adsorbed Polyelectrolytes on Cellulose I Surfaces Spin-Coated on Silicon Wafers. *Cellulose* **2005**, *12*, 127–134.

(24) Gabardo, C. M.; Zhu, Y.; Soleymani, L.; Moran-Mirabal, J. M. Bench-Top Fabrication of Hierarchically Structured High-Surface-Area Electrodes. *Adv. Funct. Mater.* **2013**, *23* (24), 3030–3039.

(25) Fu, C.-C.; Grimes, A.; Long, M.; Ferri, C. G. L.; Rich, B. D.; Ghosh, S.; Ghosh, S.;

Lee, L. P.; Gopinathan, A.; Khine, M. Tunable Nanowrinkles on Shape Memory Polymer Sheets. *Adv. Mater.* **2009**, *21* (44), 4472–4476.

(26) Zhu, Y.; Boyle, J. P.; Bonin, K.; Chowdhury, T.; Moran-Mirabal, J. M. Micro/nanostructured SiO2 and TiO2 Films Fabricated through Polymer Shrinking as Tunable Topography Substrates for Cell Studies. *Integr. Biol.* Submitted.

(27) Park, S.-J.; Kim, J.; Chu, M.; Khine, M. Highly Flexible Wrinkled Carbon Nanotube Thin Film Strain Sensor to Monitor Human Movement. *Adv. Mater. Technol.* **2016**, *1* (5), 1600053.

(28) Abitbol, T.; Kloser, E.; Gray, D. G. Estimation of the Surface Sulfur Content of Cellulose Nanocrystals Prepared by Sulfuric Acid Hydrolysis. *Cellulose* **2013**, *20*, 785–794.

(29) Habibi, Y.; Lucia, L. A.; Rojas, O. J. Cellulose Nanocrystals: Chemistry, Self-Assembly, and Applications. *Chem. Rev.* **2010**, *110* (6), 3479–3500.

(30) Aulin, C.; Gällstedt, M.; Lindström, T. Oxygen and Oil Barrier Properties of Microfibrillated Cellulose Films and Coatings. *Cellulose* **2010**, *17* (3), 559–574.

(31) Revol, J.-F.; Godbout, L.; Gray, D. G. Solid Self-Assembled Films of Cellulose with Chiral Nematic Order and Optically Variable Properties. *J. Pulp Pap. Sci.* **1998**, *24* (5), 146–149.

(32) Gray, D. G.; Mu, X. Chiral Nematic Structure of Cellulose Nanocrystal Suspensions and Films; Polarized Light and Atomic Force Microscopy. *Mater.* **2015**, *8*, 7873–7888.

(33) Zhu, Y.; Moran-Mirabal, J. Highly Bendable and Stretchable Electrodes Based on Micro/Nanostructured Gold Films for Flexible Sensors and Electronics. *Adv. Electron. Mater.* **2016**, *2*, 1500345.

Chapter 5 – Conclusions and Future Outlooks

5.1. Conclusions

Determining the mechanical properties of CNC-based films has been challenging due to the hygroscopic nature of CNCs, where the mechanical properties of CNC-containing films have been found to change with relative humidity. To overcome this limitation, the work in this thesis presents a shape-memory polymer-based structuring method as an alternative way to study the mechanical properties of CNC-based thin films. The goal of using this structuring approach was two-fold: 1) to quantify the mechanical properties of CNC-based films in a humidity-independent manner, and 2) to assess whether changes in the film's mechanical properties could be linked to changes in the film fabrication protocol.

In the study of CNC-polymer films (Chapter 3), films of varying compositions were fabricated and studied. Films were prepared using the LbL approach, where the polymer used (XG or PEI), polymer concentration used (0.1 wt% or 1 wt%), and the film thickness (1– 20.5 deposited bilayers) were modified. These films were prepared on pre-stressed PS substrates which, when heated above the glass transition temperature of PS, shrunk biaxially. The compressive stress generated from the shrinking caused the CNC-polymer films to biaxially wrinkle. The wrinkles were assessed by 2D fast Fourier transform analysis, from which humidity-independent elastic moduli of the CNC-polymer films were determined to be 70 ± 2 GPa for CNC-$XG_{0.1}$, 72 ± 2 GPa for CNC-$PEI_{0.1}$, and 32.2 ± 0.8 GPa for CNC-$PEI_{1.0}$ films. These results show that the mechanical properties of CNC-

polymer films were easily tuneable by changing different film fabrication parameters. The findings from this chapter also suggest that this PS structuring method can provide a humidity-independent measurement of the modulus of bio-based thin films, due to the irreversible nature of the wrinkling.

Next, all-CNC films were fabricated with varying CNC orientations (Chapter 4). Films were prepared by solvent-casting CNC suspensions onto pre-stressed PS substrates and allowing these suspensions to evaporate. Two parameters were modified: the film thickness (controlled through CNC suspension concentration, ranging from 0.005 – 8 wt%) and the evaporation conditions used (drying under vacuum, by heating, or by spin-coating). Altering the drying conditions resulted in films with different nanoparticle orientations, where films had chiral nematic (dried under vacuum), isotropic (dried by heating), or uniaxial (dried by spin-coating) orientations. The films were then structured by heating and shrinking the PS substrates at 135°C, which caused the films to biaxially wrinkle. The resulting wrinkled films had distinct morphologies that varied with CNC orientation, where films with isotropic CNC orientations exhibited the roughest morphology, films with chiral nematic CNC ordering exhibited the smoothest morphology, and films with uniaxial (radial) CNC alignments had narrow ridges and tightly packed wrinkles. These unique wrinkle morphologies suggest that nanoparticle orientation in the all-CNC films induces changes in the mechanical properties of these films, and that the orientation axis in uniaxial (radial) films may cause an asymmetry in the elastic modulus of the film, resulting in an asymmetric wrinkle morphology.

This work shows that the mechanical properties of CNC-based films can be studied in a humidity-independent way, and can be tuned based on changes in the film composition and the CNC nanoparticle orientation. This is important, since a major limitation in studying the mechanical properties of these films thus far has been the humidity-dependence of the mechanical properties and the frequent cracking observed in films prepared on elastomeric substrates. Precise knowledge of the mechanical properties of these films is also crucial for finding the most suitable applications for such materials. In particular, as a renewable and environmentally-friendly bio-based nanomaterial, CNCs are being studied in various applications, where they could potentially be used as substitutes for fossil fuel-derived materials.

5.2. Future Outlooks

Future work should aim to expand on the knowledge of nanocellulose-based thin films through the use of the structuring method presented in this thesis. The following six directions of work are proposed:

1. First, the mechanical properties of all-CNC films should be determined and assessed to see whether they change with CNC orientation within the films.
2. Furthermore, the fracture toughness of CNC-polymer films and all-CNC films should be assessed quantitatively, to determine: A) at which points (*i.e.*, film thickness) the films will begin to crack at the wrinkle ridges, and B) to relate changes in fracture toughness to film composition (in CNC-polymer films), CNC

orientation (in all-CNC films), and polymer plasticization (whether the absence or presence of polymer in the CNC-based films affects their fracture toughness).

3. In addition, the optical properties of the structured all-CNC films should be assessed. Planar all-CNC films with a chiral nematic CNC ordering has found applications in anti-counterfeiting devices and security paper, as reflective coatings, and as photonic filters, where their unique assembly cannot be reproduced by photocopying, printing, or scanning. It would be interesting to assess if these properties are translated from planar all-CNC films to the wrinkled all-CNC films, or if they are altered (*e.g.*, enhanced or reduced) due to film wrinkling.
4. Other types of nanocelluloses (such as cellulose nanofibrils and bacterial cellulose) should also be used to form all-nanocellulose films, structured, then assessed for their mechanical properties. Mechanical properties of these films should be compared to all-CNC films, and should be related to changes in nanocellulose orientation within the films. It would also be interesting to look at the hydrolysis of cellulose films by enzymes such as cellulases. Studies should focus on how changes in the film's topography (planar vs. structured) affects the overall hydrolysis of the film, and how the enzymatic breakdown of cellulose links to a reduction in the mechanical properties of these films.
5. Nanocomposite films should be formed on pre-stressed PS substrates, with the goal of mimicking the complex interactions present within the plant cell wall (*e.g.*, hydrogen bonding and van der Waals interactions of cellulose microfibrils with one another, and also with lignin and hemicelluloses). Nanocomposite films should

consist of nanocellulose (*e.g.*, CNCs and CNFs), lignin, and hemicelluloses, where the composition of these films should be varied and studied using the PS structuring approach. Changes in the mechanical properties and fracture toughness of these films should be studied as a function of film composition, in order to see: A) how film composition affects the strength and flexibility of the nancomposites, and B) whether there is a film composition that most closely mimics the mechanical, tensile, and load-bearing properties of the cell wall.

6. Lastly, a comprehensive study should be performed to assess the limits of film structuring and elastic modulus characterization for this PS shrinking approach. Specifically, films with a range of thicknesses, elastic moduli, and fracture toughnesses should be prepared and studied. With this information, it would be interesting to also compare the advantages and limitations of this structuring method to other techniques that are used to characterize the mechanical properties of thin films (*e.g.*, DMA, nanoindentation).

Appendix A – Supplementary Information for Chapter 3

Beyond Buckling: Humidity-Independent Measurement of the Mechanical Properties of Green Nanobiocomposite Films

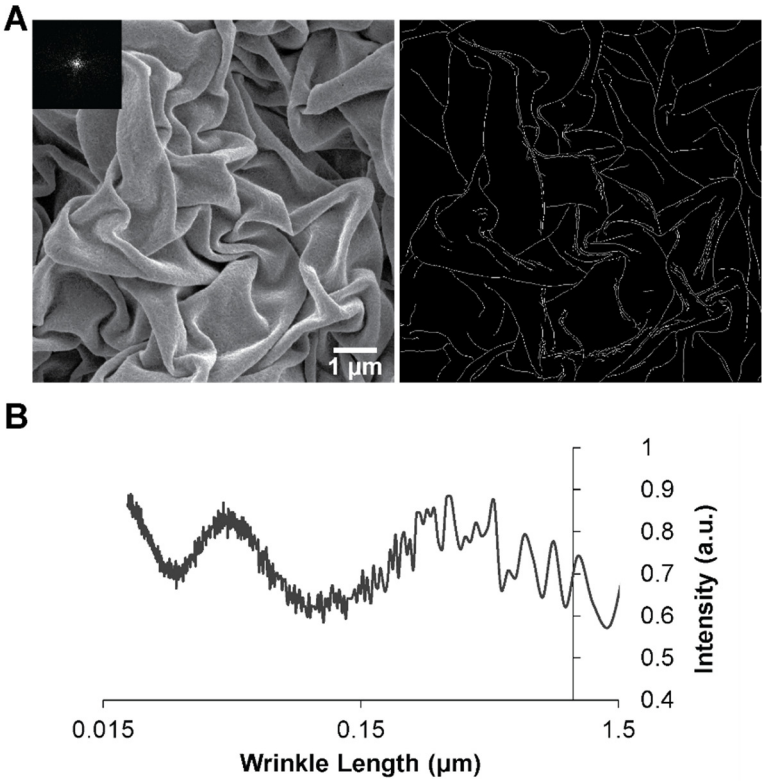

Figure A-1. Steps involved in 2D FFT analysis to determine characteristic wrinkle length of structured nanobiocomposite films, using a CNC-$PEI_{1.0}$ film (N = 2.5 bilayers) as an example. (A) SEM images were cropped to 900×900 pixels and adjusted for their brightness and contrast (right). Using the Canny threshold method, the edges of the wrinkles were highlighted and generated as a binary image (left). A MATLAB program was then used to run a 2D FFT on the binary image and produce a power spectrum, which is shown in the inset of the cropped SEM image. From the power spectrum, an intensity vs. wrinkle length plot was generated by the program, and the points were normalized to the maximum intensity. (B) All normalized intensity vs. wrinkle length (µm) plots generated for a film were averaged then graphed as an intensity vs. log (length) plot. The first maximum corresponds to thin lines next to each wrinkle that appear due to the intensity in the SEM images, while the second maximum corresponds to the wrinkle widths. The peaks with the highest probabilities within the wrinkle width region were averaged to determine the characteristic wrinkle length (ζ) of the film.

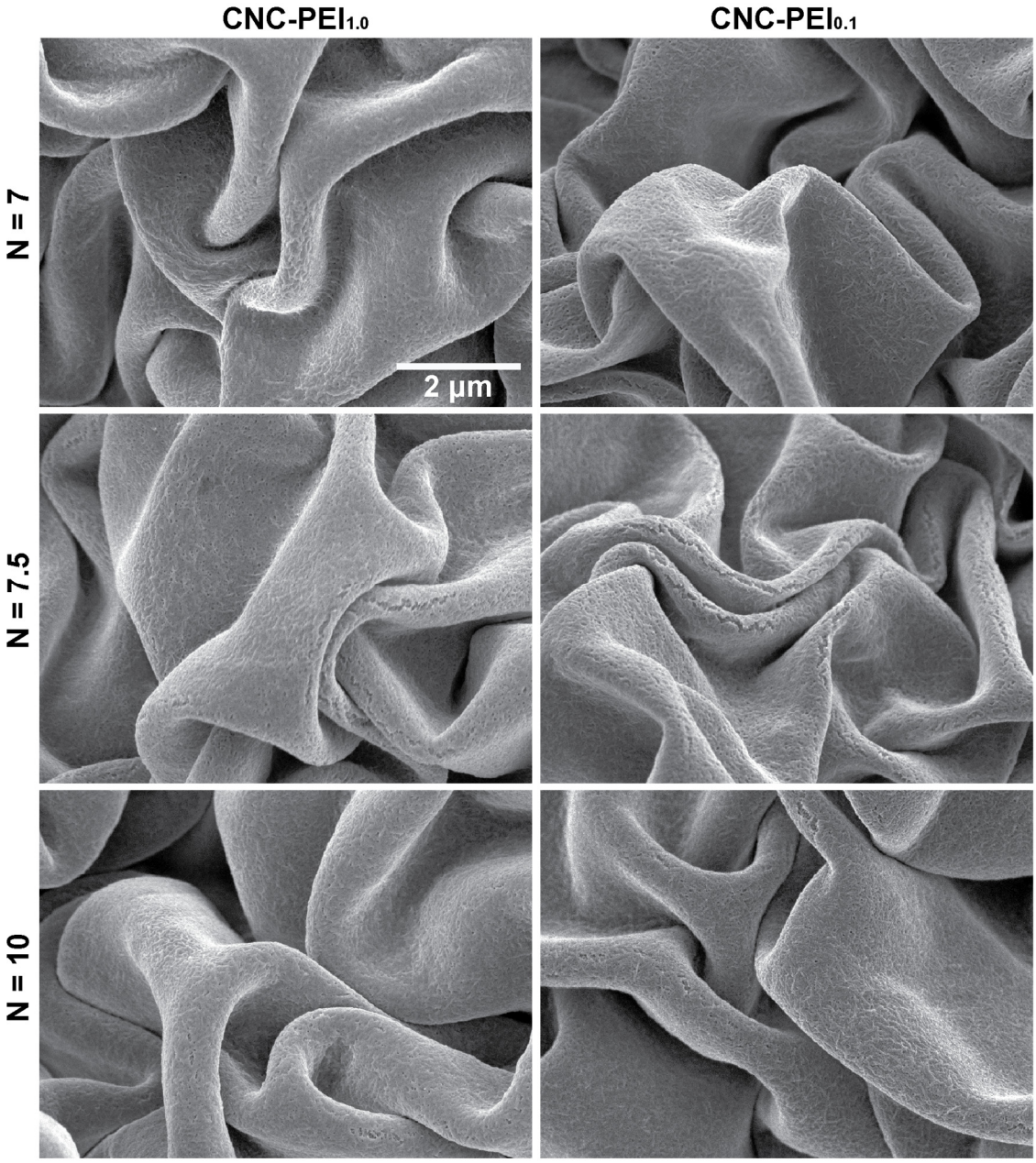

Figure A-2. Structured CNC-polymer films exhibited increased film cracking from 7 (N) to 7.5 (N + 0.5) bilayers, but reduced film cracking from 7.5 bilayers to 10 bilayers, the next full bilayer film prepared.

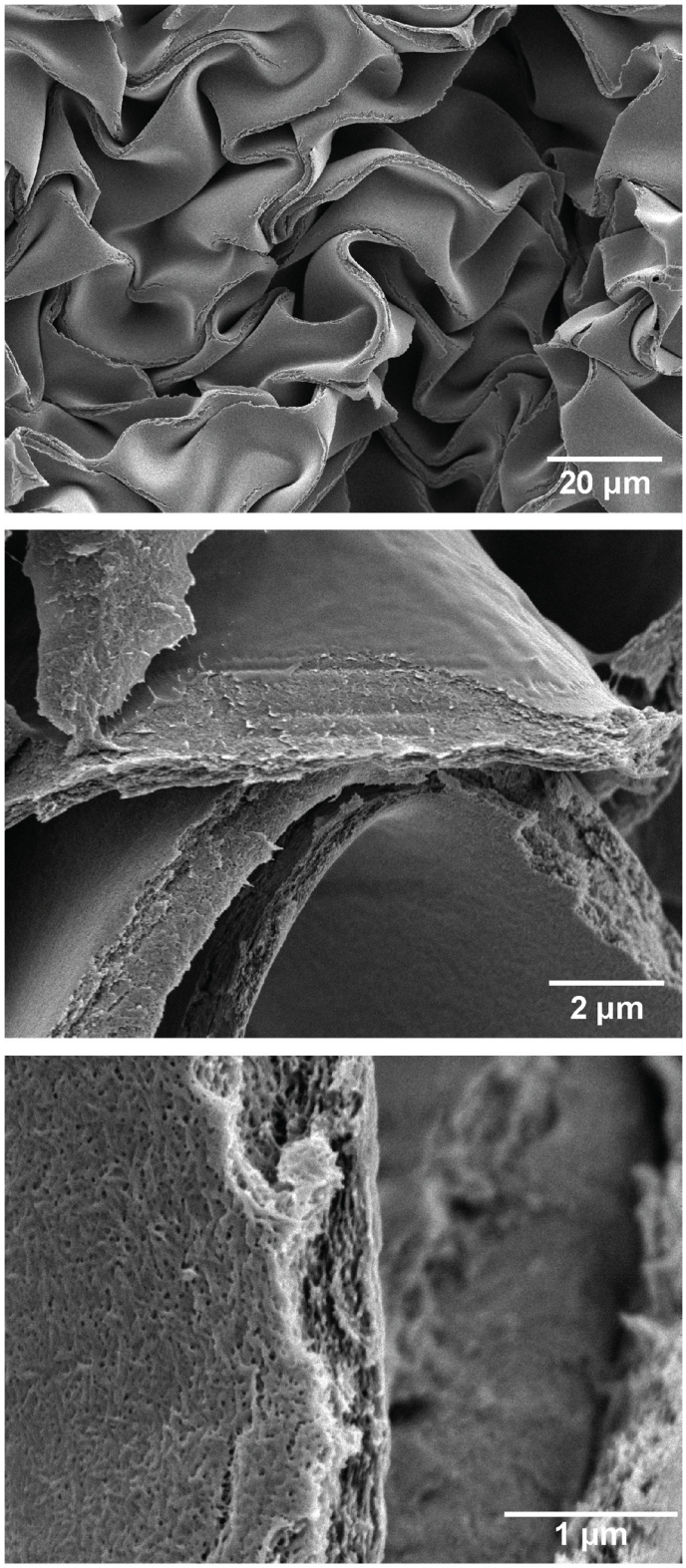

Figure A-3. Structured CNC-$PEI_{0.1}$ films with N = 40 bilayers.

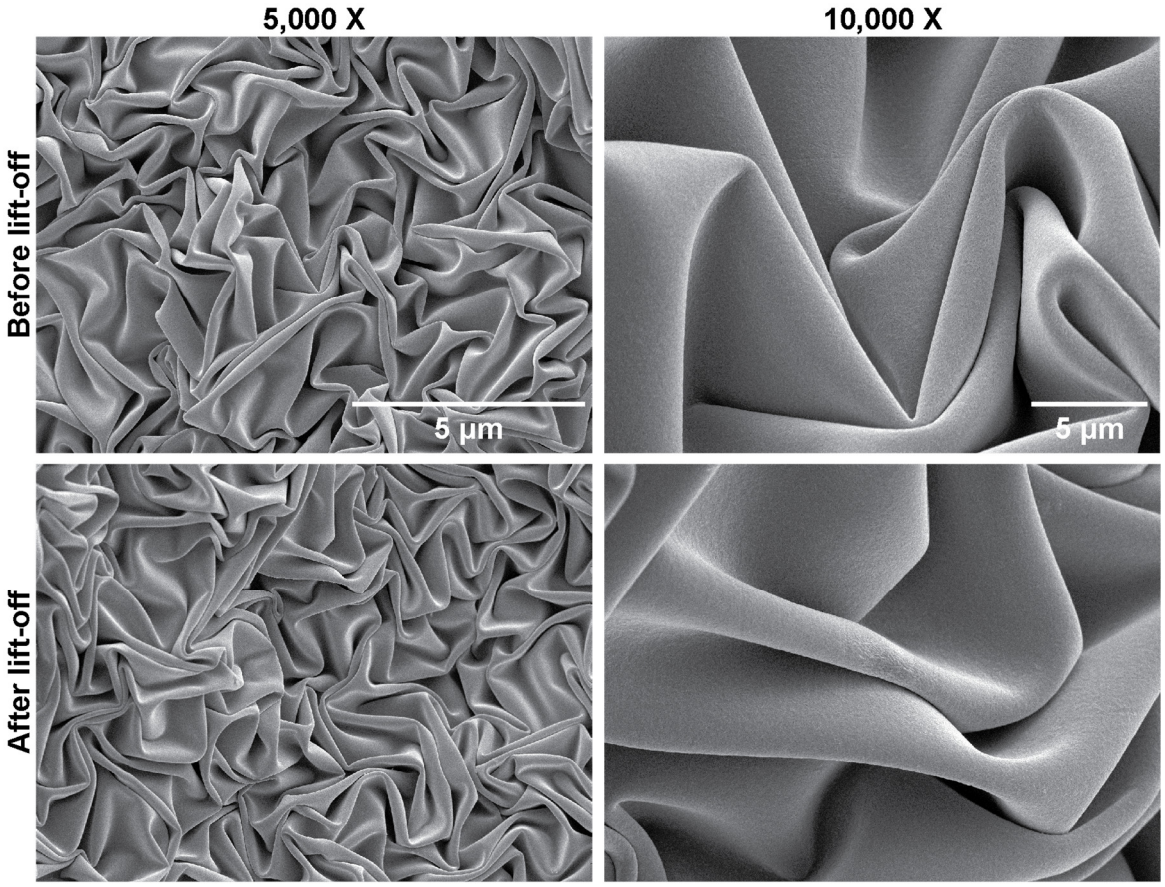

Figure A-4. CNC-PEI$_{1.0}$ films (N = 10 bilayers) were deposited on PS substrates, with an intermediate sacrificial layer between the film and the substrate. Films were structured by heating PS above its glass transition temperature (before lift-off). The sacrificial layer was then dissolved, causing the structured films to lift-off from the PS substrate (after lift-off). A 2D FFT analysis on these SEM images showed that the wavelength of the structures before lift-off and after lift-off remained identical, with average values of 2 µm and 1.95 µm, respectively.

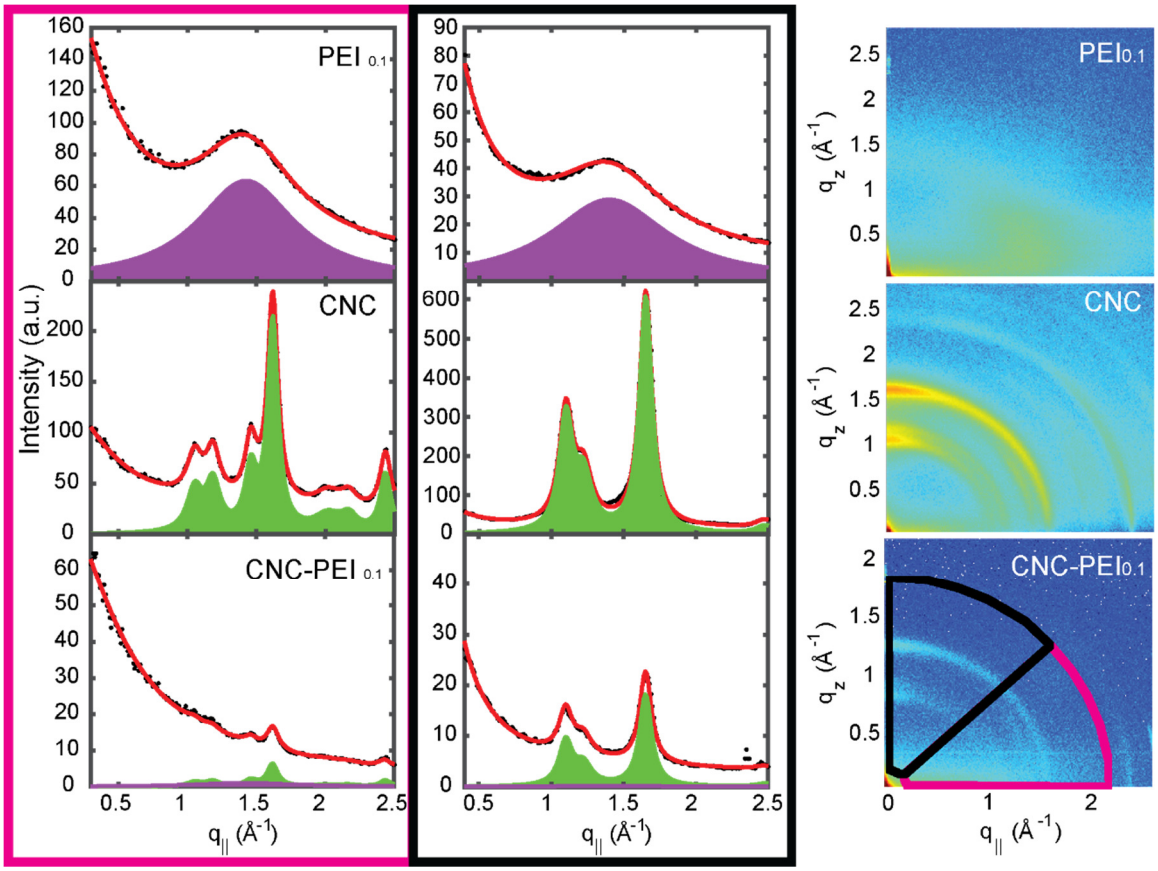

Figure A-5. 2D XRD plots and their corresponding intensity graphs for CNC-PEI$_{0.1}$ films with N = 40 bilayers.

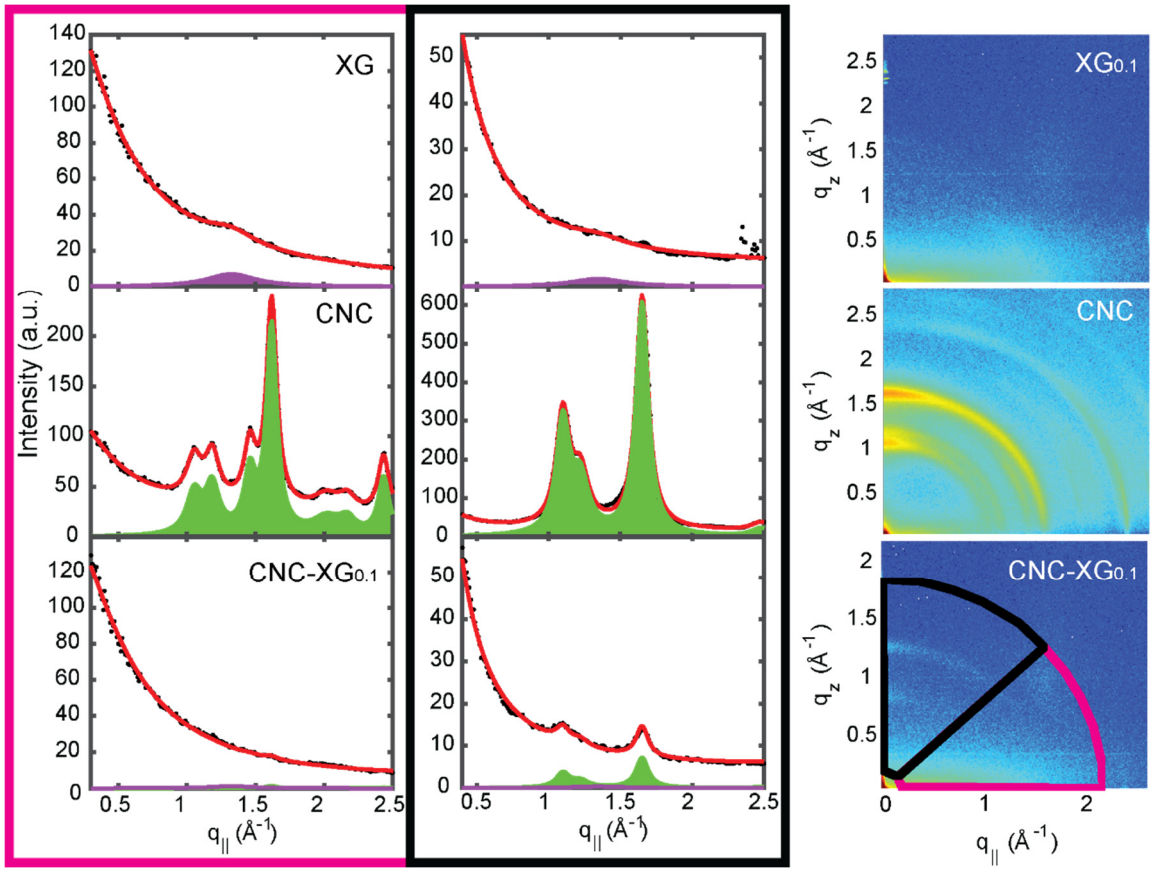

Figure A-6. 2D XRD plots and their corresponding intensity graphs for CNC-$XG_{0.1}$ films with N = 20 bilayers.

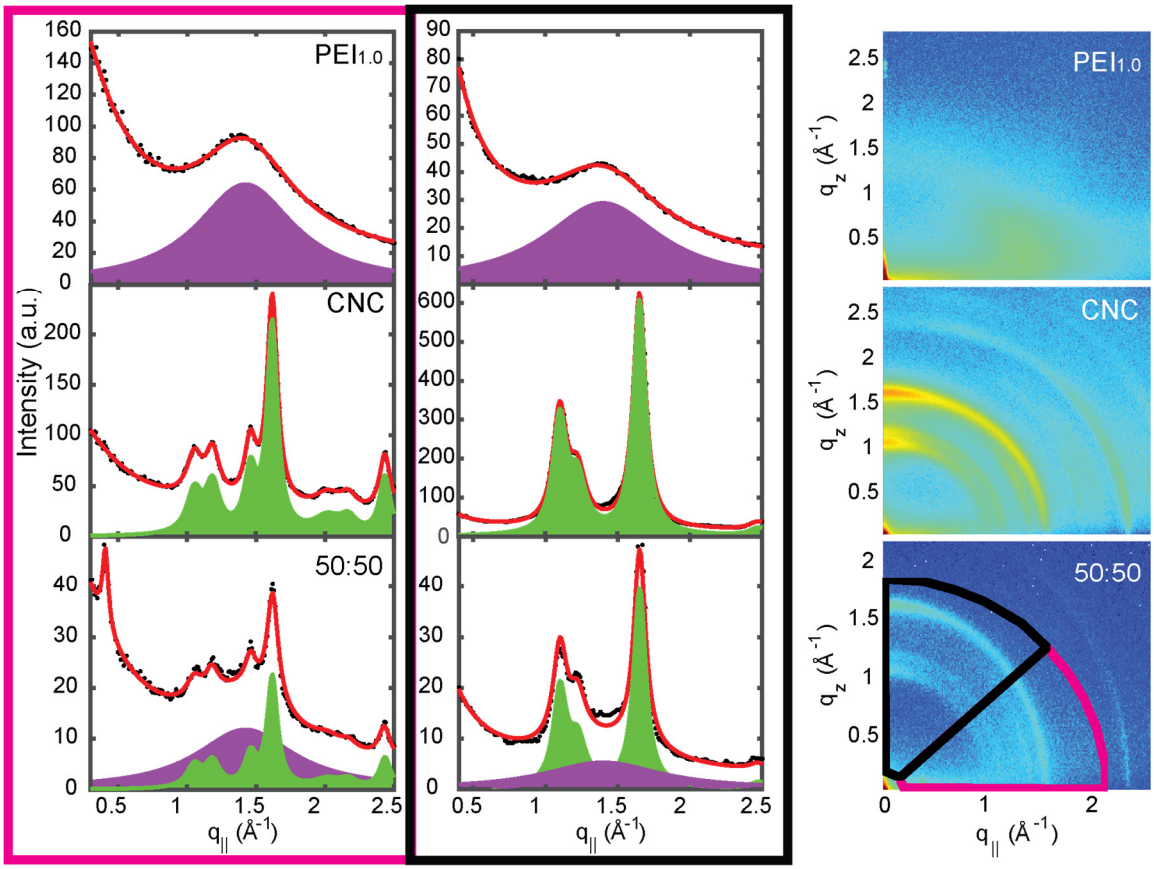

Figure A-7. 2D XRD plots and their corresponding intensity graphs for a drop-casted CNC:$PEI_{1.0}$ film, with a composition of 50:50 by mass.

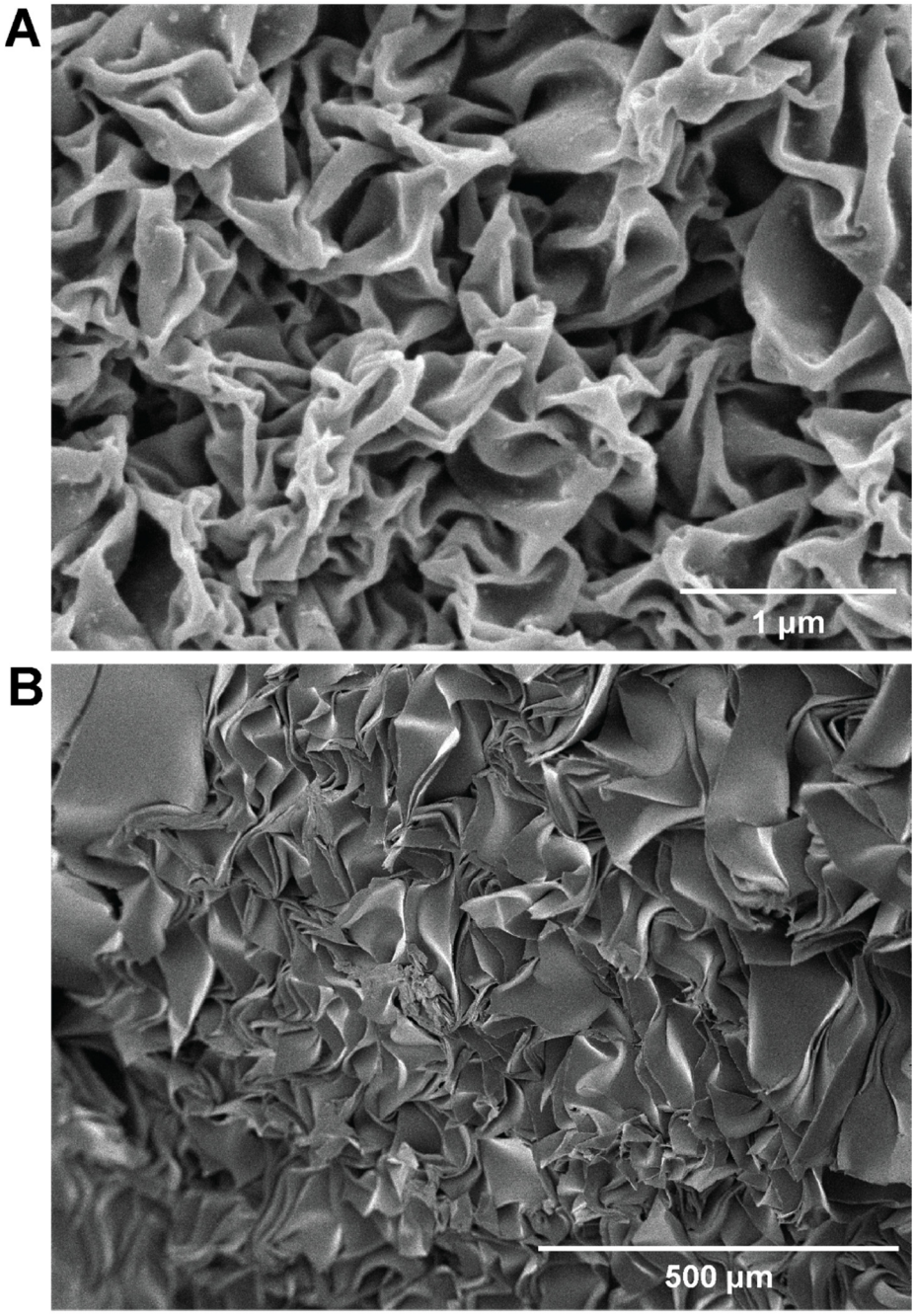

Figure A-8. (A) XG-only films and (B) CNC-only films were fabricated on pre-stressed PS substrates, then shrunken to form biaxially wrinkled surfaces.

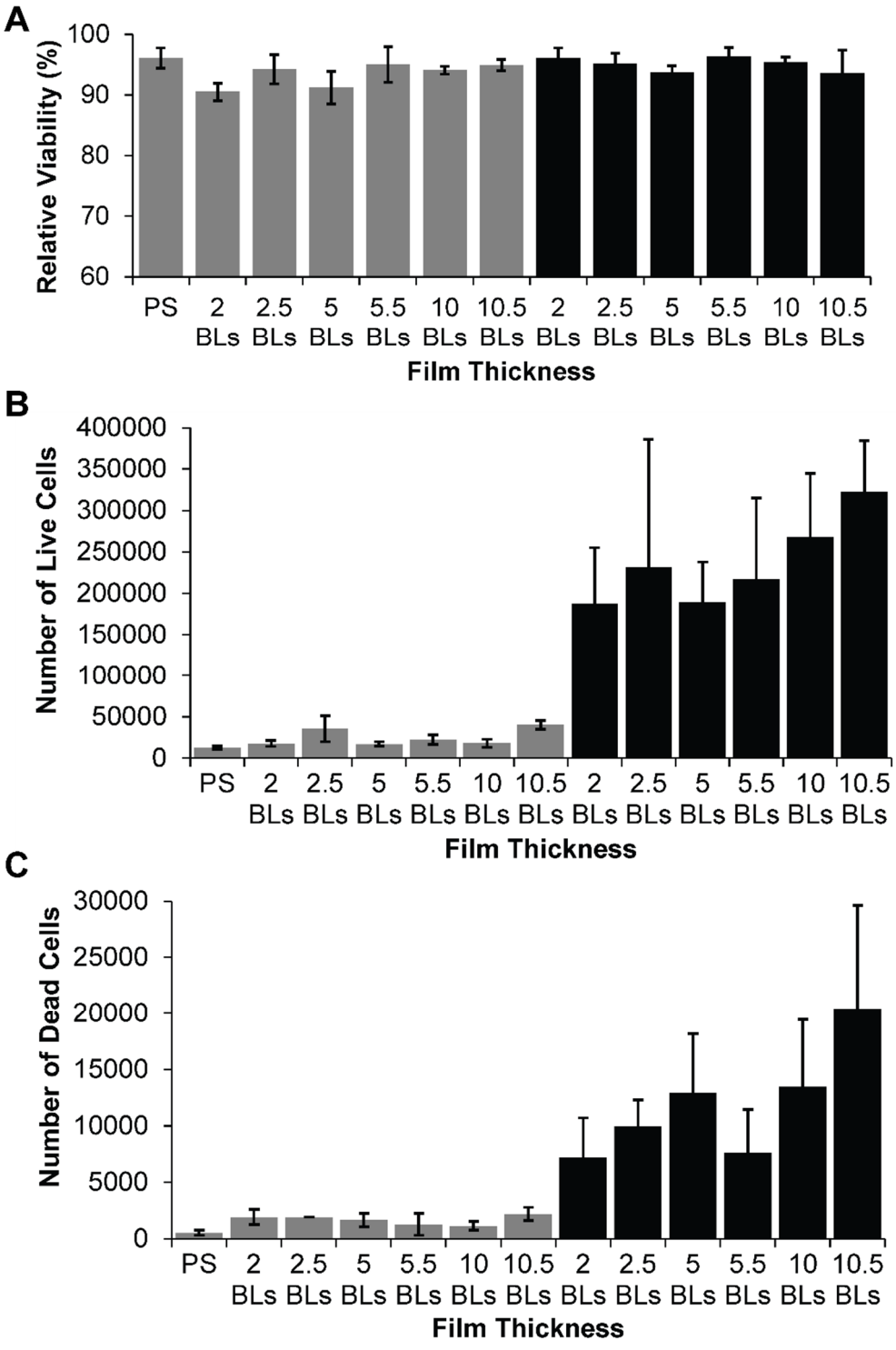

Figure A-9. Plots demonstrating (A) cell viability, (B) number of live cells and (C) number of dead cells for RAW264.7 cells that were cultured on unstructured (grey) and structured (black) CNC-$PEI_{1.0}$ films prepared to a varying number of bilayers (BLs); n = 3.

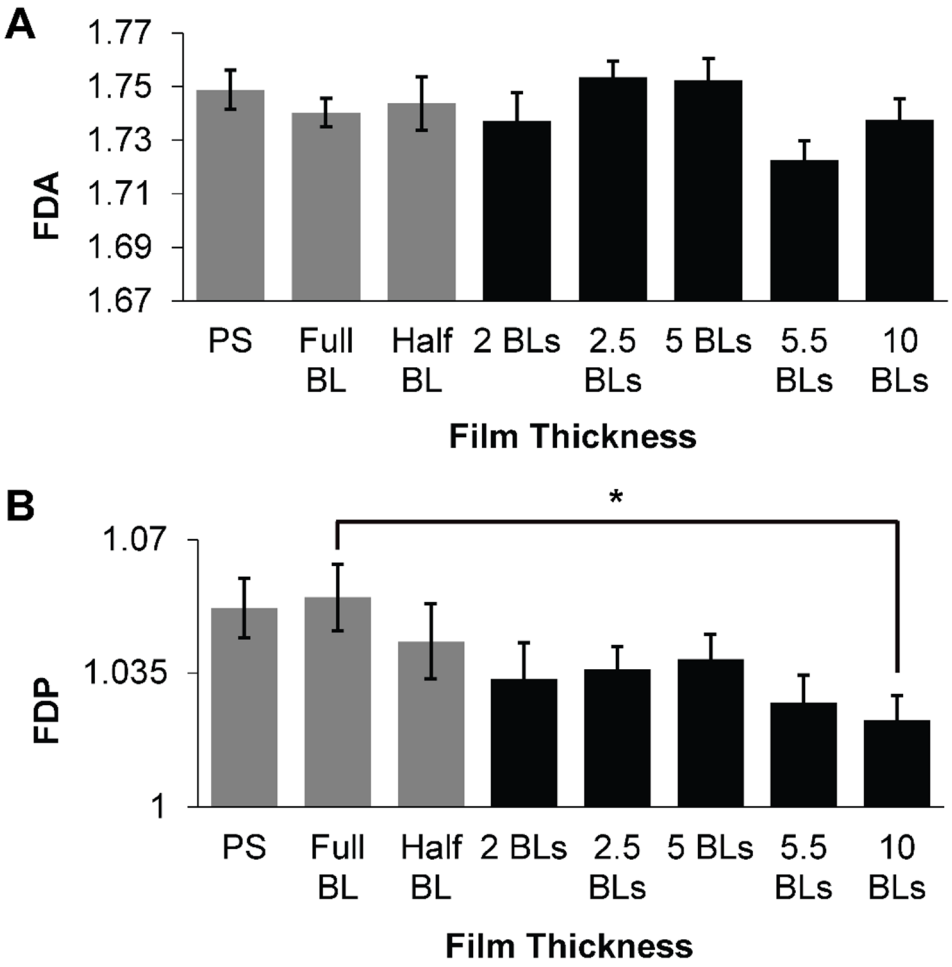

Figure A-10. Plots demonstrating (A) fractal analysis of cell area (FDA), and (B) fractal analysis of cell perimeter (FDP) for RAW264.7 cells cultured on unstructured (grey) and structured (black) CNC-$PEI_{1.0}$ films prepared to a varying number of bilayers (BLs). Statistical significance - * $p < 0.05$, $n \geq 30$.

Method for determination of the elastic moduli of CNC-polymer films

With ξ (persistence length), a (scaling factor, constant), ζ (characteristic wrinkle length) and h (thickness), the theory by Groenewold[1] describes the relationship $\xi = a\zeta = 2\pi\eta^{\frac{2}{3}}h$, where η itself is related to the elastic modulus and Poisson ratio of the substrate and the rigid film:

$$\eta = \frac{E_f(1-\nu_{PS}^2)}{3E_{PS}\left(1-\nu_f^2\right)} \quad \text{(A.1)}$$

E_{PS} and ν_{PS} are the elastic modulus and Poisson's ratio of the bulk polystyrene (PS) substrate, and E_f and ν_f are the elastic modulus and Poisson's ratio of the rigid CNC-polymer film on the PS substrate. Since $\frac{\xi}{h} = 2\pi\eta^{\frac{2}{3}}$, it can also be shown:

$$\frac{\zeta}{h} = \frac{2\pi}{a}\left(\frac{\left(1-\nu_{PS}^2\right)}{3E_{PS}}\right)^{\frac{2}{3}}\left(\frac{E_f}{\left(1-\nu_f^2\right)}\right)^{\frac{2}{3}} \quad \text{(A.2)}$$

where, $\frac{\zeta}{h}$ is equal to the slope ($m \pm e_m$) from plots of the characteristic wrinkle length vs. thickness for the structured films. This slope was determined for structured gold films sputtered onto pre-stressed polystyrene substrates, giving a value of 7.4 ± 0.8. To calculate the scaling factor a, we used E_{PS} = 1.63 GPa and ν_{PS} = 0.36 (both at 135°C), and E_f = 70 GPa and ν_f = 0.42 for sputtered thin gold films, and obtained a = 5.2 ± 0.5. A variable k was then defined as:

$$k = \frac{2\pi}{a}\left(\frac{\left(1-\nu_{PS}^2\right)}{3E_{PS}}\right)^{\frac{2}{3}} \quad \text{(A.3)}$$

as a constant used to calculate the moduli of all films with a value of 0.38 ± 0.04. Following this calibration with the structured gold films, Equation 4 was used to determine

the moduli of the CNC-polymer films. We assumed $\nu_f = 0.3$ for all nanobiocomposite films. The slopes of these plots and the corresponding elastic moduli were calculated and are listed in Table A-1.

$$E_f = \left(1 - \nu_f^2\right)\left(\frac{m}{k}\right)^{\frac{3}{2}} \quad \text{(A.4)}$$

Table A-1. Slopes of characteristic wrinkle length vs. thickness and the calculated elastic modulus for the bionanocomposite films.

CNC-Polymer Film	**Slope** $(\boldsymbol{m \pm e_m})$	**Elastic modulus** $(\boldsymbol{E_f \pm e_{E_f}})$
CNC-$XG_{0.1}$	6.8 ± 0.5	70 ± 2 GPa
CNC-$PEI_{0.1}$	7.0 ± 0.6	72 ± 2 GPa
CNC-$PEI_{1.0}$	4.1 ± 0.2	32.2 ± 0.8 GPa

References

(1) Groenewold, J. Wrinkling of Plates Coupled with Soft Elastic Media. *Physica A* **2001**, *298*, 32–45.

Appendix B – Supplementary Information for Chapter 4

Mechanical Properties of All-Cellulose Nanocrystal Thin Films as a Function of Nanoparticle Orientation

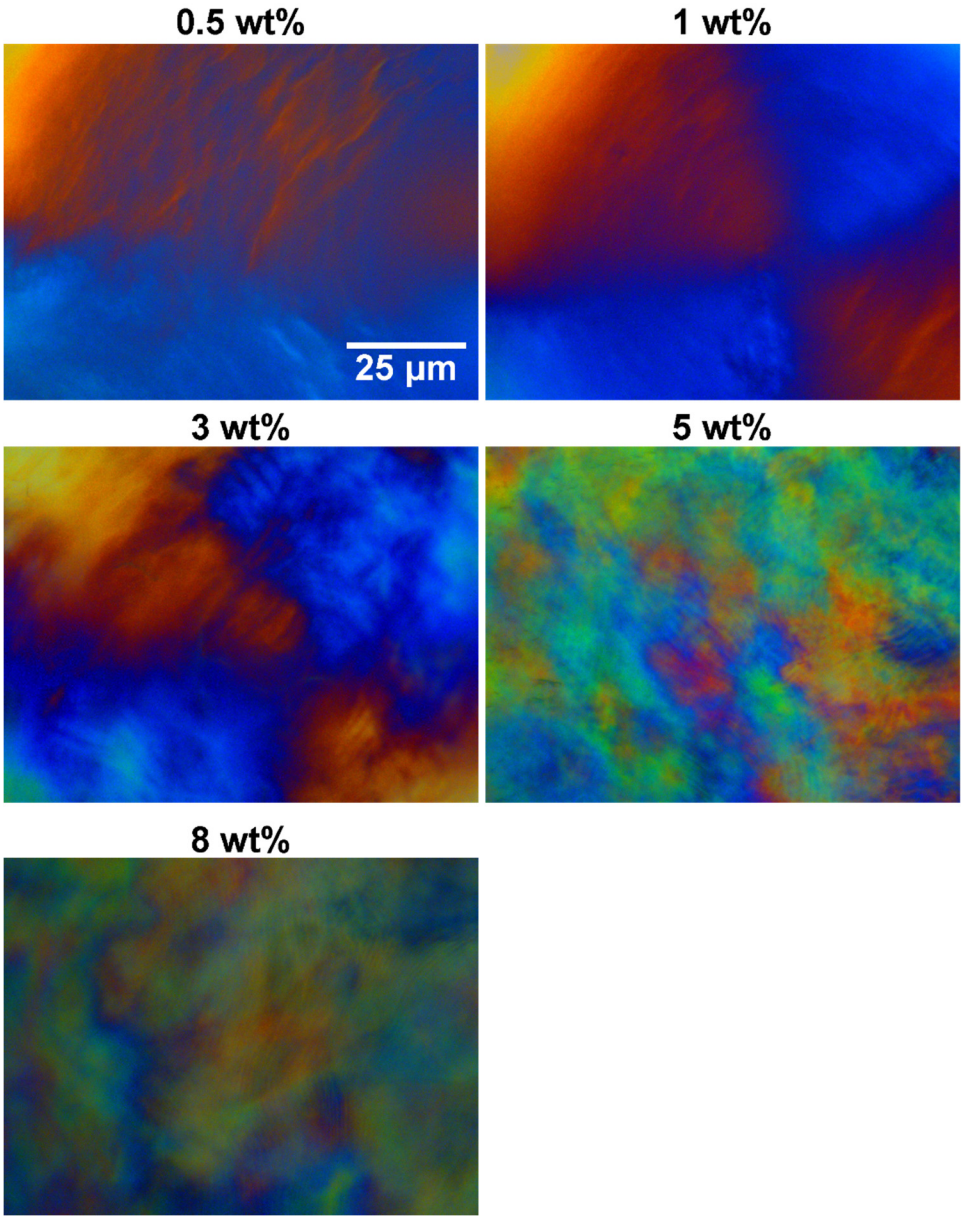

Figure B-1. POM images of all-CNC films prepared by heating of CNC suspensions. Images were taken at 40x, and show the polydomain and fingerprint texture present within these films. Images were taken in the centre of the film between crossed polarizers, using a 530 nm retardation waveplate.

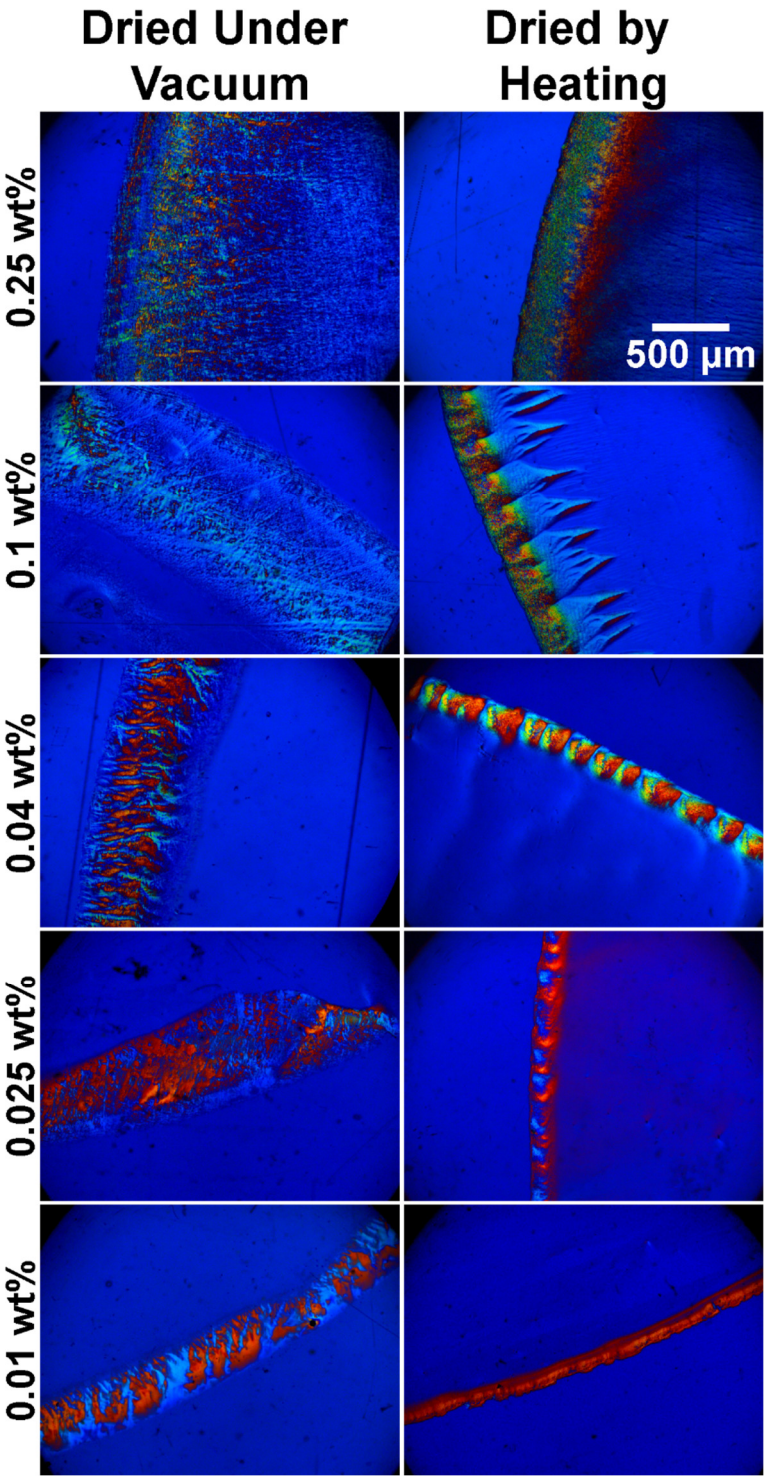

Figure B-2. POM images at the edge of CNC films that were prepared by drying suspensions under vacuum (left) and by heating (right). Images indicate that the blue colour seen throughout these films was due to the birefringence of the underlying PS substrate. Images were taken between crossed polarizers, using a 530 nm retardation waveplate.

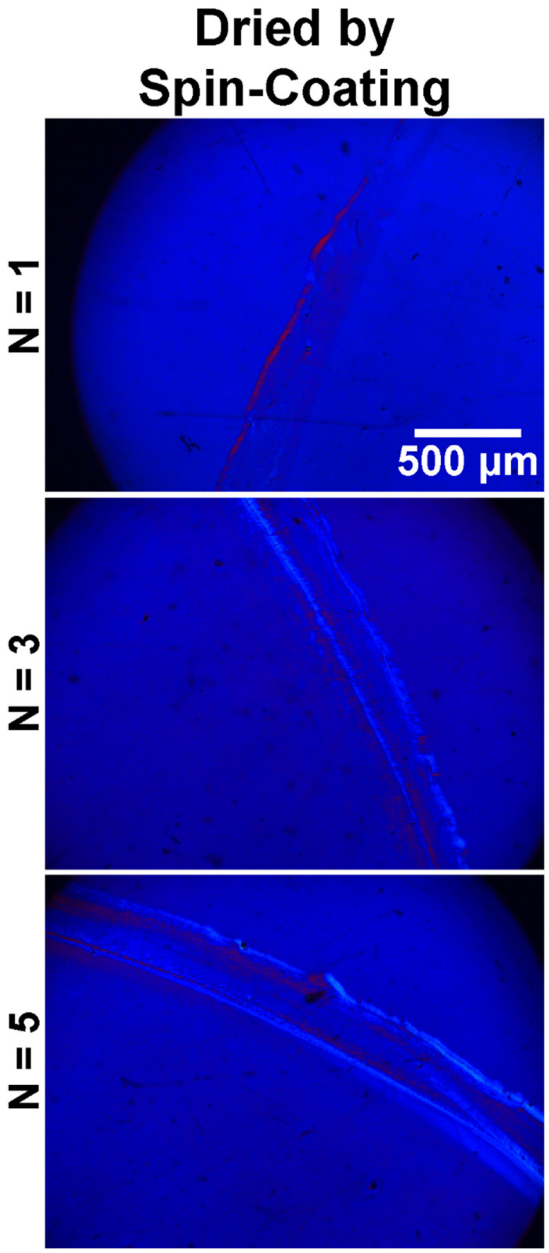

Figure B-3. POM images at the edge of CNC films that were prepared by spin-coating of CNC suspensions. Images indicate that the blue colour seen throughout these films was due to the birefringence of the underlying PS substrate. Images were taken between crossed polarizers, using a 530 nm retardation waveplate.

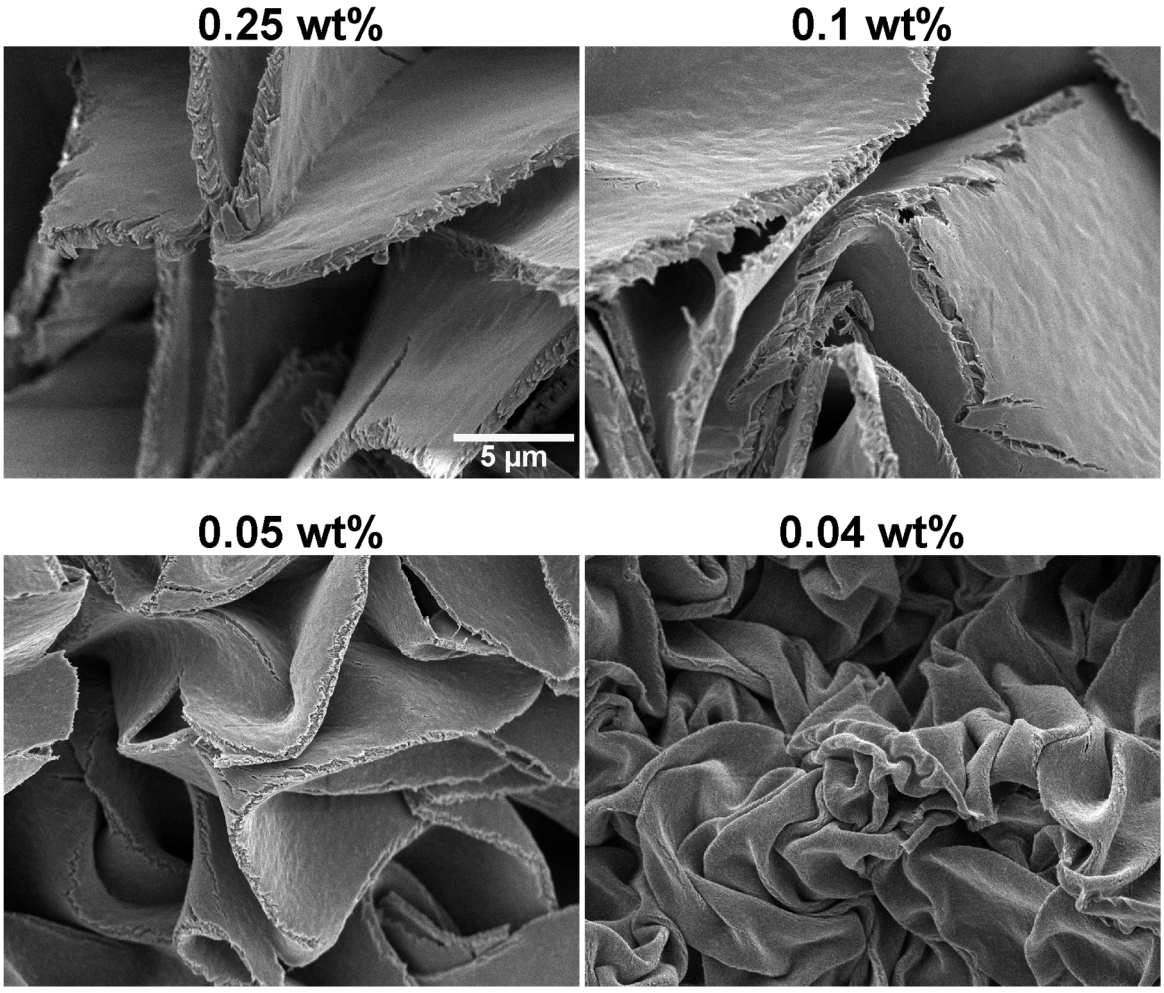

Figure B-4. SEM images showing the morphology of structured all-CNC films that were prepared by heating. Films with thicknesses beyond 0.4 µm consistently cracked (wt% > 0.04 wt%), while films that were 0.4 µm thick (0.04 wt%) formed continuously wrinkled surfaces.